

Novel Approaches to Indirect Drive Inertial Confinement Fusion

William Thomas Trickey

Doctor of Philosophy

University of York

Physics

January 2021

Abstract

This thesis describes work that developed new techniques towards indirect drive inertial confinement fusion. The work predominantly used the 1-dimensional (1D) and 2-dimensional (2D) versions of the radiation hydrodynamics code HYADES.

The scaling of ablation pressures produced by the irradiation of a material with soft X-rays was investigated. Materials with average atomic numbers between 3.5 and 22 were irradiated by X-ray sources with radiation temperatures ranging from 100 eV to 400 eV. For each material, pressure scaling laws were determined as a function of temperature and time. Additionally, the maximum drive temperature for subsonic ablation was found for all the materials. Materials with high atomic number tend to have weaker pressure scaling but higher maximum subsonic drive temperatures.

The next study found the laser drive parameters required to produce shock-ignition-like pressures through indirect drive. First, 1D simulations found an X-ray drive profile that is capable of producing shock-ignition-like pressures in a beryllium target. From there, 2D simulations were carried out to simulate the laser to X-ray conversion in a hohlraum. A laser drive profile was found that was capable of producing the required X-ray intensity profile.

The final piece of work developed a new technique for controlling the X-ray flux inside hohlraums using burn-through barriers. Hohlraum designs that use multiple chambers separated by burn-through barriers were proposed. The burn-through barriers are used to modulate the spatial and temporal properties of the X-rays as they flow between the chambers. It is shown how a number of different barrier designs can be used to manipulate the properties of the X-rays in both time and space.

Contents

Abstract	2
Contents	3
List of Tables	8
List of Figures	9
Acknowledgements	13
Declaration	14
1 Introduction	17
1.1 Inertial Confinement Fusion	17
1.2 Indirect Drive	20
1.3 The Need for Novel Approaches	21
1.4 Thesis Outline	21
2 Theory	23
2.1 Hydrodynamics and Shock Wave Physics	23
2.1.1 Fluid Description of Plasma	23
2.1.2 Forms of Fluid Equations	25
2.1.3 Acoustic Waves and Formation of Shock Waves	26
2.1.4 Rankine-Hugoniot Equations	27
2.1.5 Reflection of Shock Waves	28

<i>CONTENTS</i>	4
2.1.6 Collision of Shock Waves	29
2.2 Radiation Absorption	31
2.2.1 Inverse Bremsstrahlung	31
2.2.2 Laser Absorption	31
2.2.3 Parametric Instabilities	32
2.3 Thermal Energy Transport	33
2.3.1 Thermal Conductivity	34
2.3.2 Thermal Flux Limit	34
2.3.3 Coupling to Ions	34
2.4 Radiation Hydrodynamics	35
2.4.1 Radiation Transport Equation	36
2.4.2 Radiation in the Euler Equations	36
2.4.3 Approximate Descriptions of the Radiative Transfer Equation	37
2.4.4 Opacity Averaging	38
2.5 Radiation Waves and Ablation	38
2.5.1 Thermal Waves	39
2.5.2 Diffusive Radiation Waves in High-Z Materials	40
2.5.3 Ablation Pressure Scaling in Low-Z Materials	41
2.6 Indirect Drive	43
2.6.1 Laser to X-ray Conversion	44
2.6.2 Time-dependent Laser to X-ray Conversion Scaling	45
2.6.3 View-Factor Theory	46
2.7 Inertial Confinement Fusion	46
2.7.1 Central Hotspot Ignition	47
2.7.2 Shock Ignition	48
3 Methodology	51
3.1 HYADES Code	51
3.1.1 Lagrangian Mesh and Hydrodynamics	51
3.1.2 Thermal Transport	53

<i>CONTENTS</i>	5
3.1.3 SESAME Equation of State	53
3.1.4 Radiation Transport	53
3.1.5 Laser Absorption	54
3.1.6 Ionization	55
3.1.7 Opacity	55
3.1.8 h2d	56
3.2 F3D code	57
4 Soft X-ray Ablation Pressure Scaling	58
4.1 Introduction	58
4.2 Simulation Set-up	61
4.3 Simulation Results	62
4.4 Low-Density Titanium Simulations	66
4.5 Temperature and Time Scaling	69
4.6 Opacity effects	71
4.7 Comparison to Experiment	72
5 Indirect-Drive Shock-Ignition-Like Pressures	75
5.1 Introduction	75
5.2 1D Ablation Pressure Scaling Simulations	77
5.2.1 Direct-Drive Shock-Ignition Profile	77
5.2.2 Steady State Ablation Scaling	79
5.2.3 1D Ablation Pressure Simulations	81
5.3 2D Laser to X-ray Conversion Simulations	84
5.3.1 Hohraum Simulation	84
5.3.2 Low-Density Gas-Fill and Flux Limited Electron Transport	87
5.3.3 Higher Drive Powers	87
5.3.4 Scaling of Laser to X-ray Conversion and Ablation Pressure	88
5.4 Comparison to Other Studies	89
5.4.1 Comparison to Experimental Data	89
5.4.2 Comparison to Other NIF pulses	90

<i>CONTENTS</i>	6
5.4.3 Varying Hohlraum Size	93
5.4.4 Time-Dependent Laser to X-ray Conversion	94
5.4.5 Suprathermal Electrons	96
6 Hohlraum Burn-through Barriers	98
6.1 Introduction	98
6.2 1D HYADES Burn-through Barrier Simulations	100
6.2.1 Simulation Set-up	101
6.2.2 Comparison of High-Z Mid-Z and Low-Z Burn-through	101
6.2.3 Varying Thickness	106
6.2.4 Rising Flux Profile	107
6.3 Complex Barrier Design	110
6.3.1 Burn-through from Mid-Z to High-Z Material	110
6.3.2 Burn-through from Mid-Z to Low-Z Material	111
6.3.3 Delaying Burn-through	113
6.3.4 Burn-through Barrier Hohlräume	115
6.3.5 Shock Ignition Barrier	117
6.4 Spatially Shaped Burn-through Sources	122
6.4.1 Spatially Shaped Barrier Design	122
6.4.2 Simulation Set-up	124
6.4.3 Spatially Varying Drive Barriers	125
7 Conclusions	128
7.1 Conclusions	128
7.1.1 Soft X-ray Ablation Pressure Scaling	128
7.1.2 Producing Shock-Ignition-Like Pressures Using Indirect Drive	129
7.1.3 Hohlraum Burn-through Barriers	130
7.2 Further Work	131
8 Appendices	133
8.1 Appendix A: Derivation of Diffusion Equation	133

8.2 Appendix B: Technique for Extracting Rear-Surface Flux from HYADES . . 135

List of Tables

4.1	A table summarising the ablation pressure scaling and $T_{R,critical}$ values for plastic, beryllium, carbon, HDC, aluminium and titanium	70
5.1	A table of the laser drive powers used and the corresponding hohlraum temperatures and ablation pressures produced	88
5.2	A table summarising the peak hohlraum temperatures produced in different size hohlraums	94

List of Figures

1.1	A schematic diagram of the stages of an ICF implosion	18
1.2	A p-V diagram comparing adiabatic compression to multiple-shock compression	19
1.3	A schematic diagram of an indirect drive ICF configuration	20
2.1	A diagram of an ideal shock	27
2.2	A diagram of the collision of two counter-propagating shocks	29
2.3	A contour plot of the pressure difference between a pre-collision shock and the post-collision reflected shock	30
2.4	A diagram of the dynamics of shock ignition	50
4.1	A graph of the ablation pressure produced under X-ray drive up to 400 eV for the materials: solid DT, plastic, beryllium, carbon, high density carbon, aluminium and titanium	62
4.2	A graph showing three different fits of a power law to the ablation pressure scaling with X-ray drive temperature in beryllium	63
4.3	A number of graphs showing the fitting of a scaling law of the form $p_a = AT_R^\alpha$ to the ablation pressure scaling for beryllium, carbon, HDC, aluminium and titanium	64
4.4	A plot that summarises the $T_{R,\text{critical}}$ values predicted by theory and observed in simulation	65
4.5	A plot of the ablation front in solid-density titanium driven by a 400 eV X-ray source	65

<i>LIST OF FIGURES</i>	10
4.6 A plot of the ablation pressure and average ionisation at the ablation front in low-density titanium up to 400 eV	66
4.7 Some snapshots of the ablation front in simulations of 120 eV, 160 eV and 200 eV X-ray sources irradiating low-density titanium	67
4.8 A plot of the ablation pressure and average ionisation at the ablation front in solid-density titanium up to 400 eV using a Thomas-Fermi ionisation model	68
4.9 A plot of the ablation pressure and average ionisation at the ablation front in solid-density titanium up to 400 eV using a Saha ionisation model	69
4.10 Plots of the ablation pressure scaling with time for plastic, beryllium, carbon, HDC, aluminium and titanium	70
4.11 Plots of the repeated ablation pressure scaling simulations with varying opacity	71
4.12 Plots that compare the scaling laws from this work with experimental measurements	73
5.1 Plot of the laser power deposition used in a direct-drive shock-ignition study	78
5.2 Comparison of the ablation pressure profiles produced by direct and indirect drive in 1D simulations	82
5.3 A plot of the X-ray radiation temperature profile used in 1D simulations	83
5.4 A screen-shot of the hohlraum simulation carried out in h2d	84
5.5 A comparison of the Ribeyre power profile to the shock-ignition-like power profile	85
5.6 A plot of the laser power profile used in the hohlraum simulations and the X-ray flux profile that was produced	86
5.7 Plots of the overall scaling of laser power to hohlraum temperature to ablation pressure	89
5.8 Plotted comparisons of the laser power profile used in this work to the NIF high-foot and low-foot laser power profiles	91
5.9 Simulation results of the X-ray flux profiles produced by the NIF low and high-foot pulses compared to the 400 TW pulse used in this work	92

5.10	The laser power profile from the high-density-carbon ablator target design and the X-ray flux profile it produced in h2d simulations	93
5.11	Schematic diagram of a series of different hohlraum dimensions	94
5.12	A plot showing a linear fit to of the peak hohlraum temperature to the inner surface area of the hohlraum wall	95
5.13	A graph comparing simulations results to a laser to X-ray conversion model	96
6.1	A schematic diagram of a burn-through wave	99
6.2	Rear-surface flux profile from burn-through simulations of 15 μm gold, 30 μm copper and 800 μm beryllium	102
6.3	Plot of the rear-surface flux profile from a 15 μm gold burn-through barrier and snapshots of the simulation before, during and after the burn-through	103
6.4	Plot of the rear-surface flux profile from a 30 μm copper burn-through barrier and snapshots of the simulation before, during and after the burn-through	104
6.5	Plot of the rear-surface flux profile from a 800 μm beryllium burn-through barrier and snapshots of the simulation before, during and after the burn-through	105
6.6	Plot of the spectral structure of the burn-through radiation transmitting through 800 μm of beryllium at different stages of the burn-through.	106
6.7	A plot showing how the burn-through metrics are defined	107
6.8	Plots that show how the barrier thickness affects the burn-through metrics in beryllium, aluminium, copper and gold	108
6.9	Plots of rear-surface flux profiles and burn-through metrics for different rising X-ray sources burning through 30 μm of copper	109
6.10	Plots of rear-surface flux profiles and burn-through metrics for different rising X-ray sources burning through 800 μm of beryllium	109
6.11	Rear-surface flux profile of a copper-gold barrier compared to a pure copper barrier	111
6.12	Snapshots of the propagation of a burn-through wave in a copper-gold barrier	112

6.13	Rear-surface flux profile of a copper-beryllium barrier compared to a pure copper barrier	113
6.14	Snapshots of the propagation of a burn-through wave in a copper-beryllium barrier	114
6.15	Graphs comparing the rear-surface flux profiles in pure copper barriers to copper-plastic barriers	115
6.16	Schematic diagram of a hohlraum with an external burn-through chamber . .	116
6.17	Set-up of the shock-ignition burn-through barrier simulation	118
6.18	Rear-surface flux profiles from the burn-through of a shock-ignition compression-pulse through gold barriers of varying thickness	119
6.19	Rear-surface flux profiles from the burn-through of a shock-ignition ignition-pulse through copper barriers of varying thickness	120
6.20	X-ray flux results from the shock-ignition burn-through barrier simulation . .	121
6.21	A schematic diagram of a pixelated burn-through barrier	123
6.22	Rear-surface flux profile of a number of copper-plastic barriers with different copper:plastic thickness ratios	123
6.23	A schematic diagram of hohlraum burn-through barrier simulations carried out in F3D	125
6.24	The angular flux profile across the capsule for a number of different spatially varying burn-through sources in a hohlraum	126
6.25	Angular flux profiles across the surface of a capsule in a burn-through hohlraum with a narrower geometry	127
8.1	A plot of the photon spectral group structure in a HYADES simulation . . .	136
8.2	A histogram plot of the boundary emission from each spectral group in a HYADES simulation	137

Acknowledgments

Here I would like to dedicate a few words to some of the people who have offered me help and support over the course of my PhD.

First and foremost, my supervisor John who has provided me with the perfect balance of academic support and freedom. He had a talent for boosting my confidence and leaving me in an optimistic mood after every meeting.

I would like to thank all of the great teachers and role models I have had at the York Plasma Institute. With particular thanks to Kate who taught me both in the classroom and the lab and has always closely supported my outreach work.

To the wider laser-plasma scientific community. I have been taught by so many wonderful people and learned so much.

Thanks go to the EPSRC for funding the project.

To the many close friends I have made on the Fusion Centre for Doctoral Training course. Life has been made so much more pleasant with such a wonderful group of people to share an incredibly challenging four years. Particular thanks goes to my four year long office-mate Andrew, who shares my passion for scientific communication and served as a constant reminder of just how difficult doctorates can be.

To all my friends and family who have shown an interest in my work. To my Mum, whose passion for knowledge and learning mirrors my own. To my Dad, whose unrelenting work ethic has always inspired me. To my sister, for keeping me grounded and whose passion and talent for teaching is something I will always aspire to.

Declaration

This thesis has not previously been accepted for any degree and is not being concurrently submitted in candidature for any degree other than Doctor of Philosophy of the University of York. This thesis is the result of my own investigations, except where otherwise stated. All other sources are acknowledged by explicit references.

I declare that this thesis is a presentation of original work and I am the sole author. This work has not previously been presented for an award at this, or any other, University.

I am responsible for the running of all the simulations that were carried out in HYADES and h2d. HYADES and h2d are commercial products of Cascade Applied Sciences. Jamie Walsh made a significant contribution to the work described in chapter 4. Jamie carried out the preliminary work in the study but all the results presented in this thesis are from simulations that I ran myself. The development and running of the F3D code was undertaken by Joseph Owen. All sources are acknowledged as References. The work has been entirely supervised by Dr. John Pasley.

Much of the work discussed in this thesis has been presented at scientific conferences and has been, or will be, published in peer-reviewed journals. Full details of all prior published and presented work are given under the headings ‘Journal Articles’ and ‘Conference Proceedings’.

The work presented herein was funded by the Engineering and Physical Sciences Research Council (EPSRC), grant reference number: EP/L01663X/1.

Journal Articles

The details of the publications based on work presented in this thesis are as follows:

- [1] Plasma Physics and Controlled Fusion - 2019:
“Producing Shock-Ignition-like Pressures Through Indirect Drive”
W. Trickey and J. Pasley
doi: <https://doi.org/10.1088/1361-6587/ab3007>

- [2] Physics of Plasmas - Accepted for publication as of 10/09/2020
“Controlling X-Ray Flux in Hohlräume Using Burn-through Barriers”
W. Trickey, J. Owen, C. Ridgers and J. Pasley

- [3] In the final stages of preparation for submission to Matter and Radiation at Extremes
“Time-dependent subsonic ablation pressure scalings for soft X-ray heated low- and intermediate-Z materials at drive temperatures of up to 400 eV”
W. Trickey, J. Walsh and J. Pasley

Conference Proceedings

In addition to journal articles, work from chapters 5 and 6 have been presented at the following conferences:

2018 - HPL Christmas meeting (Poster Presentation):

“A Shock Ignition Scheme Using an Indirect Drive X-ray Source“

2019 - Direct Drive and Fast Ignition Workshop (Oral Presentation):

“Producing Shock Ignition-like pressures through indirect drive“

2019 - International Conference on High Energy Density (Poster Presentation):

“Producing Shock Ignition-like pressures through indirect drive“

2019 - IOP Plasma Physics (Oral Presentation):

“Producing Shock Ignition-like pressures through indirect drive“

2019 - International Conference on Fusion Science and Applications (Poster Presentation):

“Creating Fast Rises in Hohlraum Temperature with X-ray Burn-through Barriers“

2019 - HPL Christmas meeting (Oral Presentation):

“Producing Rapid Rises in Hohlraum Temperatures Using a Novel X-ray Burnthrough Technique“

2020 - Extreme Physics, Extreme Data, Lorentz Center Workshop (Lightning Talk):

“Machine Learning Led Indirect Drive Shock Ignition Target Design“

2020 - Prospects for High Gain Inertial Fusion Energy (Poster Presentation) *“A Novel*

Technique for Controlling X-Ray Flux in Hohlraums Using Burnthrough Barriers“

Chapter 1

Introduction

1.1 Inertial Confinement Fusion

In 2015 the World Energy Council predicted that demand for electricity would increase from 24 098 TW h to somewhere between 44 000 TW h and 49 000 TW h by 2060^{1,2}. Whilst most of this growth is intended to be met by increased capacity of renewables, there will still be a need for large-scale, reliable reactors (>500 MW)^{1,3}. In 2060 it is likely that a significant proportion of this form of energy will still be supplied by carbon emitting fuel sources. The advent of fusion energy will assist in shifting our reliance away from carbon fuels. Currently, nuclear fission reactors are taking on the brunt of this challenge but fusion offers several advantages over fission. Lower levels of activation in the waste products, more energy dense and abundant fuel and no possibility of meltdown make fusion a well suited candidate for a reliable, large scale energy supplier.

For many decades a variety of approaches to realising fusion energy have been considered. To generate an efficiently burning fusion plasma, one must heat it and confine it for a period of time such that the energy produced from fusion outweighs the radiative and conductive losses⁴. This criterion is known as the Lawson Criterion and was later extended to include temperature in which case it is known as the “triple product”. One of the mainstream approaches to create a burning plasma attempts to use high power lasers to compress fusion fuel to a high fuel density (~ 1000 g cm⁻³) and temperature (~ 10 keV), confined under its own inertia for a brief time (a few tens of picoseconds). This technique was first described

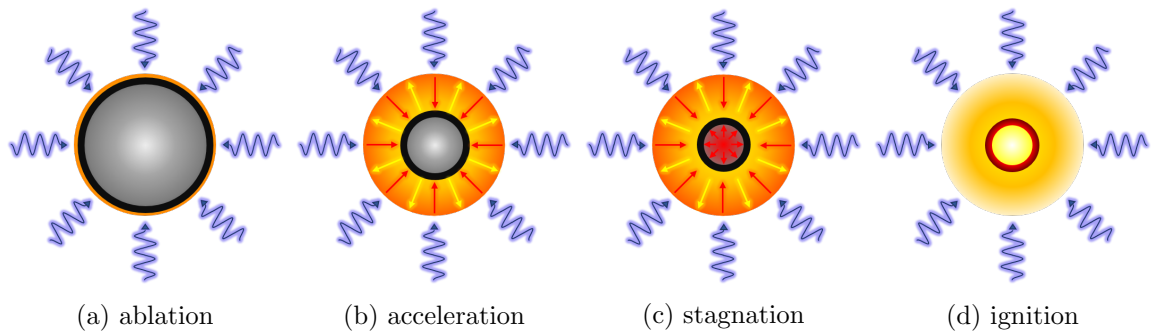


Figure 1.1: A schematic diagram that shows the stages of an ICF implosion. (a) The capsule is irradiated by the driver and the outer surface begins to ablate. (b) The ablation of material accelerates the shell inwards. (c) As the DT gas in the centre of the capsule is compressed, the pressure increases and causes the imploding shell to stagnate. (d) The fuel is then heated via mechanical work until ignition occurs in the centre and a burn-wave begins to propagate outwards.

in print in 1972⁵ and is known as Inertial Confinement Fusion (ICF).

In ICF, a capsule of deuterium-tritium (DT) fuel is compressed under high pressures produced via the ablation of material from the outer surface of the capsule. The stages of an ICF implosion are shown schematically in figure 1.1 The capsule is filled with a DT gas but the bulk of the fuel is kept as a solid in the shell surrounding it. The laser energy will either irradiate the capsule directly (direct drive), or is used to create a bath of soft X-rays (indirect drive). When using indirect drive, an ablator material (e.g. plastic) must be used (note that ablators are also sometimes used in direct drive). In both approaches, the outer layer of the capsule is heated and material begins to ablate from the surface. Through momentum conservation, as material is ejected from the capsule surface, a force acts to accelerate the shell inwards. As the shell converges, the gas is compressed and its pressure increases. Eventually the pressure will be enough to resist the inwards motion of the shell, causing it to stagnate. During the deceleration of the shell mechanical work is done, which raises the temperature of the fuel and creates a central hotspot. If the kinetic energy in the imploding shell is above a certain threshold, the fuel will be heated enough to ignite in the centre. A burn-wave will then propagate outwards through the dense fuel. If a sufficient amount of mass was assembled over the course of the compression, enough fuel will burn such that an overall gain in energy will result.

For efficient compression, the entropy of the fuel should be kept to a minimum. In the ideal case the fuel would be compressed adiabatically but to do this in ICF would require an un-

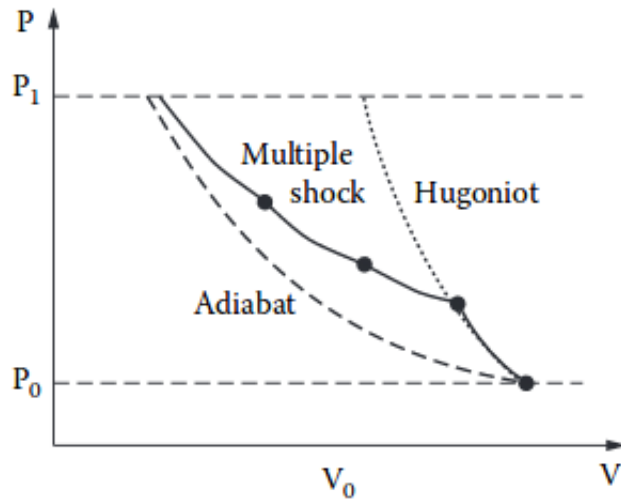


Figure 1.2: A p-V diagram comparing the adiabatic curve to multiple-shock compression. Taken from reference 7.

realistic degree of control over the compression⁶. Instead, efficient compression is achieved by launching a series of increasingly strong shocks. Figure 1.2 shows how, by using multiple shocks, one can reach a compression that is close to adiabatic. The Hugoniot describes the locus of the possible thermodynamic states of the shocked material. It can be seen that, by using multiple shocks, the compressed material will almost follow the p-V path of adiabatic compression. As the area under the curve represents the work done, the result is that multiple-shock compression approaches the efficiency of adiabatic compression.

Decades of research into ICF culminated in the construction of the National Ignition Facility (NIF)⁸, completed in March 2009. The NIF is capable of delivering 1.9 MJ of energy via 192 beams at a peak power of 500 TW⁹. In the first three years of its operation, the NIF dedicated a series of experiments to ignition, which were collectively referred to as the National Ignition Campaign⁹. The National Ignition Campaign failed to achieve ignition and whilst significant improvements have been made since then, ignition remains an elusive goal. The most successful shot to date saw a yield of 54 kJ, achieving a fusion yield greater than the kinetic energy of the shell¹⁰.

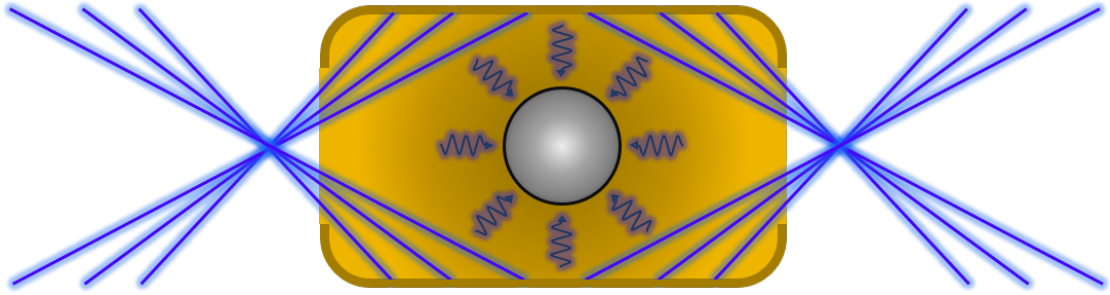


Figure 1.3: A schematic diagram of an indirect drive ICF configuration. Lasers are shone onto the inner surface of a cylindrical high-Z hohlraum. The hohlraum walls are heated and begin to emit soft X-rays, which fill the cavity and drive the ablation of the fuel capsule.

1.2 Indirect Drive

The mission of the NIF was to demonstrate ignition of a fusion capsule via indirect drive in which the lasers are shone onto the interior of a cylindrical casing with a high atomic number (high-Z) called a hohlraum. The lasers heat the inner hohlraum walls producing X-rays, which symmetrically irradiate the fusion fuel capsule. A diagram of the concept of indirect drive is shown schematically in figure 1.3. Overall, indirect drive is less efficient than direct drive in terms of coupling energy to the capsule. However, indirect drive offers a significant advantage in that the soft X-ray field has a high spatial uniformity. In direct drive, intensity variations in the beam can imprint perturbations on the capsule that develop into detrimental hydrodynamic instabilities¹¹. In designing the NIF, an indirect drive configuration was chosen as it was assessed that the benefits of higher irradiation uniformity outweighed the disadvantages of less efficient energy coupling¹².

Over the last few decades a great deal of effort has been invested into understanding the physical processes present in the conversion of lasers to X-rays inside hohlraums. The plasma that fills the cavity is susceptible to a number of different laser-plasma interactions (LPI) such as stimulated Brillouin scattering (SBS), stimulated Raman scattering (SRS), two-plasmon decay (TPD), and cross-beam energy transfer (CBET)¹³. These LPI have two detrimental effects. Firstly, they act to redistribute power within the hohlraum, which can result in asymmetric implosions. Secondly, they can produce small populations of hot electrons, which can penetrate deep into the fuel and cause pre-heat. A detailed understanding of these effects is necessary to achieve high performing implosions and it is still an area of

active research.

1.3 The Need for Novel Approaches

Whilst the NIF has made substantial progress in the last decade, there are still a few outstanding issues preventing ignition from being achieved. These include the previously mentioned LPI that degrade laser to X-ray conversion¹⁴, asymmetric capsule compression^{15,16} and hydrodynamic instabilities¹⁷ seeded by both capsule non-uniformities¹⁸ and support structures¹⁹. In recent years, the NIF has employed a variety of pulse shape, hohlraum and capsule designs in order to address these problems; none of these designs have been able to ignite a target. Promisingly, there is still a wide range of parameter space left to explore and it is possible we may see a capsule ignite in the coming years. However, there is still a large amount of uncertainty in understanding the ignition boundary^{20,21} and it is likely that the attainment of high gains will require a new laser facility or an alternative ignition scheme²². The NIF would be of great value when pursuing these alternative techniques. It could be used as a platform upon which to develop a deeper understanding of the relevant physical phenomenon on ignition scales. As such, the NIF has motivated proposals for several alternative ICF schemes. Examples include include direct drive shock ignition²³, magnetised indirect drive ICF²⁴ and double shell capsule designs²⁵. The work in this thesis investigates some new ideas on approaches to ICF, some of which could be fielded on the NIF without any major modifications to the facility.

1.4 Thesis Outline

Chapter 2 covers the background physics that is relevant to the work carried out in this thesis. This includes: hydrodynamics and shock-waves, radiation and thermal transport in plasma and the physics of inertial confinement fusion.

Chapter 3 gives the details of the 1D and 2D versions of the radiation hydrodynamics code HYADES and the 3D view-factor code F3D, which are used throughout this thesis.

Chapter 4 describes a study in which 1D radiation hydrodynamics simulations are used

to investigate the scaling of ablation pressure with time and temperature in materials with atomic numbers up to 22 at X-ray radiation temperatures up to 400 eV.

Chapter 5 outlines work that aimed to find the laser drive parameters that would be required to produce shock-ignition-like pressures by indirect drive. 1D radiation hydrodynamics simulations are used to find an X-ray drive profile that produces the same ablation pressures to those achieved in direct-drive shock-ignition. A 2D simulation then follows that finds the laser drive parameters that produce the required X-ray field inside a hohlraum.

Chapter 6 details the development of a technique for controlling hohlraum radiation fields using burn-through barriers. A number of 1D simulations are used to study the burn-through dynamics for a number of different materials. Several uses of this technique are proposed and a 3D view-factor code investigates the effect of spatially shaped X-ray sources inside hohlraums

Chapter 7 gives a summary of the work in the preceding chapters. A brief discussion is given on potential areas of further work.

Chapter 2

Theory

This chapter outlines the key physics relevant to the work carried out in this thesis. It begins with the fluid description of plasmas and the hydrodynamics of shocks. Next, an outline is given on thermal energy and radiation transport and how they can be coupled into the hydrodynamic equations. This lays the ground-work to discuss, in detail, the physics of ablation. Finally an overview is given of ICF, some key metrics are outlined that aid in the discussion of the shock ignition scheme.

2.1 Hydrodynamics and Shock Wave Physics

2.1.1 Fluid Description of Plasma

The most complete microscopic description of a plasma is given by kinetic theory. An extensive discussion of the kinetic treatment of plasmas can be found in references [26](#) and [27](#). Kinetic theory describes plasma through the distribution function $f(\mathbf{x}, \mathbf{v}, t)$, of the particle positions \mathbf{x} , and velocities \mathbf{v} . The evolution of the distribution under an external force $\mathbf{F}(\mathbf{x}, \mathbf{v}, t)$, is expressed by the Boltzmann equation

$$\frac{\partial f}{\partial t} + \mathbf{v} \cdot \nabla f + \frac{\mathbf{F}}{m} \cdot \nabla_{\mathbf{v}} f = \left(\frac{\partial f}{\partial t} \right)_{coll}, \quad (2.1)$$

where the RHS is the term that accounts for the particle collisions. The seven dimensions of the kinetic equations (three spatial, three in velocity space and one in time) often present

quite a challenge when it comes to finding solutions. In cases such as those, it is often appropriate to resort to a plasma theory based on macroscopic values, the so called fluid description.

The fluid description of a plasma uses averaged properties values such as density, temperature and average velocity. There exists a wide range of literature on fluid mechanics, the reader is directed to references 28 and 29. In the fluid description, a plasma is treated as two different fluids, one electron and one ion. The large difference in the mass of the constituents results in motions that occur on vastly different time-scales. Because of this, the electron and ion fluids can be individually described with separate sets of equations. For simplicity, the discussion here is limited to only one set of fluid equations. Any collisional terms that would couple the two fluids together are neglected.

The conservation equations of fluid dynamics can be found by taking moments of the Boltzmann equation³⁰. At the same time, the external force is taken to be the Lorentz force given by $\mathbf{F} = q(\mathbf{E} + \mathbf{v} \times \mathbf{B})$. To begin, the conservation of mass is found by taking the zeroth moment of the Boltzmann equation. Multiplying by mass, m and integrating over velocity space, gives

$$\frac{\partial \rho}{\partial t} + \nabla \cdot (\rho \mathbf{u}) = 0, \quad (2.2)$$

where ρ is the mass density, $\rho = mn$, n is the particle number density, $n(\mathbf{x}, t) = \int f(\mathbf{x}, \mathbf{v}, t) d^3\mathbf{v}$ and \mathbf{u} is the average velocity, $\mathbf{u} = \frac{1}{n} \int \mathbf{v} f(\mathbf{x}, \mathbf{v}, t) d^3\mathbf{v}$.

Next, the first moment of the Boltzmann equation is found by multiplying by $m\mathbf{v}$ and integrating over velocity, which gives the equation of momentum transfer,

$$\frac{\partial \rho \mathbf{u}}{\partial t} + \rho (\nabla \cdot \mathbf{u}) \mathbf{u} + \nabla \cdot \mathbf{P} = \rho q \left(\mathbf{E} + \frac{1}{c} \mathbf{u} \times \mathbf{B} \right) + m \int \mathbf{v} \left(\frac{\partial f}{\partial t} \right)_{coll} d^3\mathbf{v}, \quad (2.3)$$

where \mathbf{P} is the stress tensor. The second and third term on the left hand side (LHS) of 2.3 arise from the separation of the velocity term into some bulk fluid velocity plus some random fluctuation, $\mathbf{v} = \mathbf{u} + \delta\mathbf{u}$. The second term describes the flux of momentum due to the bulk velocity of the fluid, \mathbf{u} . The third term describes the transfer of momentum due to the pressure gradient, a result of the random motion, $\delta\mathbf{u}$.

Finally, the second moment of the Boltzmann equation gives the energy transfer equation,

$$\rho \frac{\partial}{\partial t} \left(\frac{1}{2} u^2 + \varepsilon \right) + \nabla \cdot \left[\mathbf{u} \rho \left(\frac{1}{2} u^2 + \varepsilon \right) \right] + \nabla \cdot (\mathbf{q} + \mathbf{P} \mathbf{u}) = nq \mathbf{E} \cdot \mathbf{u} + \int \mathbf{v} \mathbf{v} \left(\frac{\partial f}{\partial t} \right)_{coll} d^3 \mathbf{v}. \quad (2.4)$$

The thermal energy density term comes from $\rho \varepsilon = \frac{1}{2} m \langle \delta u^2 \rangle$, where $\langle \delta u \rangle$ is the average square random velocity and the heat flux \mathbf{q} , is given by $\mathbf{q} = \frac{\rho}{2} \langle \delta u^2 \delta \mathbf{u} \rangle$. Equations 2.2, 2.3 and 2.4 describe the single fluid behaviour of a plasma. In the next sections they will be used to derive the equations that describe the propagation of shock fronts in fluids.

2.1.2 Forms of Fluid Equations

The fluid equations in the previous section were derived in an Eulerian form, where a fluid element is considered fixed in time and space observing mass flow in and out. It is often convenient to express the fluid equations in the Lagrangian form, where the fluid element has a fixed mass and can flow freely. A complete description of the Lagrangian fluid equations is given in reference 31. Here, the fluid equations are expressed in a simplified Eulerian form and the converted to Lagrangian. In 1-dimension (1D), the viscosity terms in the stress tensor disappear and the divergence of the stress tensor becomes the pressure gradient; then, ignoring the Lorentz and collisional terms and removing the heat flux, the Eulerian equations become

$$\frac{\partial \rho}{\partial t} = -\nabla \cdot (\rho \mathbf{u}), \quad (2.5)$$

$$\frac{\partial \rho \mathbf{u}}{\partial t} = -\rho (\nabla \cdot \mathbf{u}) \mathbf{u} + \nabla p, \quad (2.6)$$

$$\frac{\partial}{\partial t} \rho \left(\frac{1}{2} u^2 + \varepsilon \right) = -\nabla \cdot \left[\mathbf{u} \rho \left(\frac{1}{2} u^2 + \varepsilon \right) \right] + \nabla \cdot (p \mathbf{u}). \quad (2.7)$$

Using the Lagrangian relation³⁰

$$\frac{D}{Dt} = \frac{\partial}{\partial t} + \mathbf{u} \cdot \nabla, \quad (2.8)$$

where D represents the Lagrangian derivative, the equations become

$$\frac{D\rho}{Dt} + \rho (\nabla \cdot \mathbf{u}) = 0, \quad (2.9)$$

$$\rho \frac{D\mathbf{u}}{Dt} + (\nabla p) = 0, \quad (2.10)$$

$$\rho \frac{D}{Dt} \left(\frac{1}{2} u^2 + \varepsilon \right) + \nabla \cdot (p\mathbf{u}) = 0. \quad (2.11)$$

2.1.3 Acoustic Waves and Formation of Shock Waves

Before moving on to the physics of shock waves, a brief discussion is given on their formation from non-linear acoustic waves. Consider some small disturbance in a stationary fluid at constant density or pressure expressed by

$$\rho = \rho_0 + \delta\rho, \quad (2.12)$$

$$p = p_0 + \delta p. \quad (2.13)$$

$$\mathbf{u} = 0 + \delta\mathbf{u} \quad (2.14)$$

Substitution into the Lagrangian fluid equations 2.9 and 2.10 gives

$$\frac{D}{Dt} (\rho_0 + \delta\rho) = -(\rho_0 + \delta\rho) \nabla \cdot (\delta\mathbf{u}), \quad (2.15)$$

$$(\rho_0 + \delta\rho) \frac{D(\delta\mathbf{u})}{Dt} = -\nabla (p + \delta p). \quad (2.16)$$

We can use the fact that the derivatives of the constant terms are zero, and that $\delta\rho \ll \rho_0$ and $\delta p \ll p_0$ to give

$$\frac{D(\delta\rho)}{Dt} = -\rho_0 \nabla \cdot (\delta\mathbf{u}), \quad (2.17)$$

$$\rho_0 \frac{D(\delta\mathbf{u})}{Dt} = -\nabla (\delta p). \quad (2.18)$$

If we take the time derivative of 2.17 and the divergence of 2.18, using the Lagrangian relation 2.8, ignoring second order terms and combining gives

$$\frac{\partial^2 (\delta\rho)}{\partial t^2} = c_s^2 \nabla^2 (\delta p), \quad (2.19)$$

where the sound speed is given by $c_s = (\partial p / \partial \rho)$. Equation 2.19 is a wave equation for which the general solution has the form $\psi = f_1(x - c_s t) + f_2(x + c_s t)$. In this manner we can

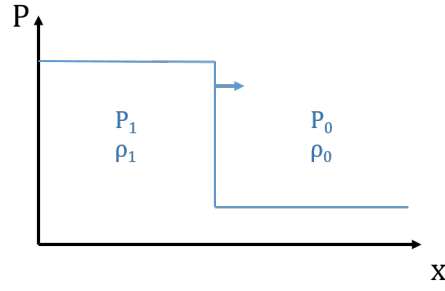


Figure 2.1: A simple diagram of a shock front propagating from left to right into a material of uniform density and pressure.

describe the movement of a wave of any physical property as a function of $x \pm c_s t$. Now consider some piston on the LHS that is pushing into a fluid at an accelerating velocity. At one moment in time the movement of the piston compresses the fluid sending forward a compression wave that travels at the sound speed. If we consider the acceleration of the piston as a series of increasing velocity steps over a number of time intervals, at the next interval a new compression wave is sent through the fluid that is travelling at a higher sound speed due to the increase in internal energy caused by the previous compression wave. This creates a series of increasingly fast compression waves that will eventually coalesce, forming a discontinuous shock front.

2.1.4 Rankine-Hugoniot Equations

A shock wave is a travelling, discontinuous boundary of pressure, density or temperature. The evolution of a shock front in time can be described in terms of the conservation of mass, momentum and energy across the discontinuity^{28,29}. Consider the mass and pressure discontinuity in figure 2.1, travelling at speed u_s . The undisturbed material ahead of the shock front is denoted with the subscript 0 and the compressed material behind the shock front given subscript 1. In the frame of the shock, the Euler equations can be used to describe the flow of material across the boundary. If equations 2.5, 2.6 and 2.7 are integrated in space over an infinitesimal boundary ($x_1 - x_0 \rightarrow 0$), the LHSs will all tend to zero leaving only the RHS flux terms that must be equal on either side of the boundary

$$\rho_0 u_0 = \rho_1 u_1, \quad (2.20)$$

$$\rho_0 u_0^2 + p_0 = \rho_1 u_1^2 + p_1, \quad (2.21)$$

$$\varepsilon_0 + \frac{u_0^2}{2} + \frac{p_0}{\rho_0} = \varepsilon_1 + \frac{u_1^2}{2} + \frac{p_1}{\rho_1}. \quad (2.22)$$

Equations 2.20-2.22 are the 1D, adiabatic Rankine-Hugoniot (RH) equations. They can be used to express some useful relations. The first being the Hugoniot condition for the specific energies. Combining equations 2.20 - 2.22 gives

$$\varepsilon_1 - \varepsilon_0 = \frac{1}{2}(p_0 + p_1)(V_0 - V_1), \quad (2.23)$$

where $V_n = 1/\rho_n$. Now, for a polytropic gas, where $\varepsilon = pV/(\gamma - 1)$, the Hugoniot condition for pressure takes the form

$$\frac{P_1}{P_0} = \frac{(\gamma + 1)V_0 - (\gamma - 1)V_1}{(\gamma + 1)V_1 - (\gamma - 1)V_0}. \quad (2.24)$$

In a similar manner, the fluid velocities behind and ahead of the shock front can be related by

$$u_1 = u_0 + \left[\frac{2p_0}{\rho_0} \frac{\left(\frac{p_1}{p_0} - 1\right)^2}{\frac{p_0}{p_1}(\gamma + 1) + (\gamma - 1)} \right]^{\frac{1}{2}} \quad (2.25)$$

2.1.5 Reflection of Shock Waves

In plasma physics, the fluid dynamics is often much more complex than the case of a single shock travelling through fluid of uniform density. There may be a number of shocks travelling at different speeds, interacting with one another and traversing regions of non-uniform density. Consider the shock from the previous section incident on a boundary with a density much higher than that of the shocked material. In the limit of very high density, it is assumed that there is no transmitted shock through the boundary and the shock front is entirely reflected. The region behind the reflected shock will be denoted with the subscript 2. A boundary condition can be imposed that there can be no flow in the high density region of the material. In this case the fluid velocity behind the reflected shock must be zero or $u_0 = u_2 = 0$. Inserting this condition into the RKH equations for an ideal shock results in

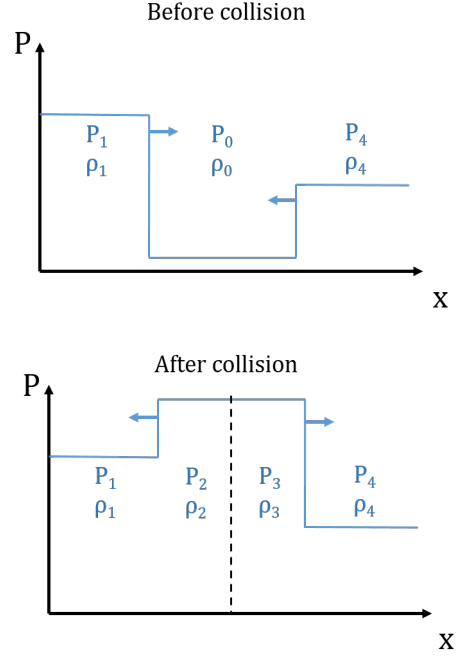


Figure 2.2: A diagram of the collision of two counter-propagating shocks. After the collision two new shocks of matching pressure are set-up propagating back into the shocked material

the relation²⁸

$$p_2 = p_1 \frac{\alpha + 2 - \frac{p_0}{p_1}}{1 + \alpha \frac{p_0}{p_1}}, \quad (2.26)$$

where $\alpha = (\gamma + 1)/(\gamma + 2)$.

2.1.6 Collision of Shock Waves

One of the key physical phenomena for the shock ignition ICF scheme (discussed later in section 2.7.2) is the collision of two counter-propagating shock waves. A simple analytical approach to describing the collision of two counter-propagating shocks is given here. Consider the two counter-propagating shocks in figure 2.2. Upon collision, a transmitted shock (travelling right) and reflected shock (travelling left) will be created. It is assumed that the pressure and fluid velocity is continuous across the boundary of regions 2 and 3. If this was not the case, additional discontinuities would be formed. Substituting these conditions into

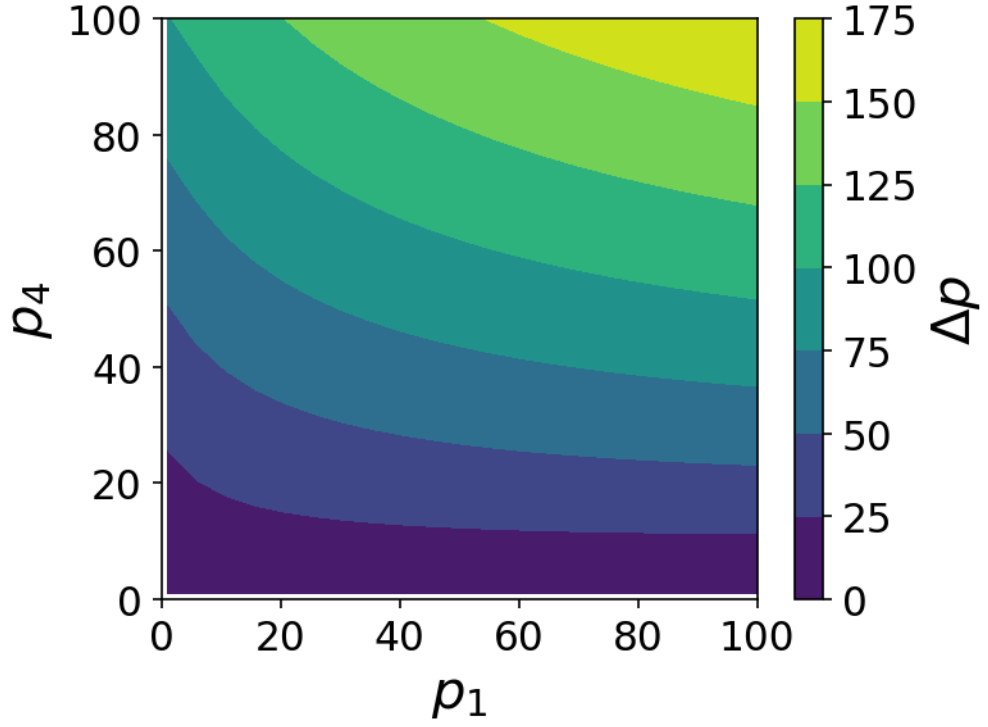


Figure 2.3: A contour plot that shows the pressure difference between the post-collision reflected shock p_2 and the pre-collision LHS shock p_1 . These results come from numerically solving equation 2.27.

the RKH equations derived previously gives the equation²⁸

$$\frac{1 - \frac{p_1}{p_2}}{\left[\frac{p_1}{p_2} \left(\alpha + \frac{p_1}{p_2}\right)\right]^{\frac{1}{2}}} + \frac{\frac{p_0}{p_1} - 1}{\left(1 + \alpha \frac{p_0}{p_1}\right)^{\frac{1}{2}}} + \left(\frac{\frac{p_0}{p_1} \left(\alpha + \frac{p_0}{p_1}\right) \left(1 + \alpha \frac{p_0}{p_4}\right)}{\frac{p_0}{p_4} \left(\alpha + \frac{p_0}{p_4}\right) \left(1 + \alpha \frac{p_0}{p_1}\right)}\right)^{\frac{1}{2}} \times \left(\frac{\frac{p_0}{p_4} - 1}{1 + \alpha \frac{p_0}{p_4}} + \frac{\frac{p_0}{p_4} - \frac{p_0}{p_2}}{\left[\frac{p_0}{p_2} \left(\alpha \frac{p_0}{p_4} + \frac{p_0}{p_2}\right)\right]^{\frac{1}{2}}}\right) = 0 \quad (2.27)$$

where the subscripts denote the regions outlined in figure 2.2. For the case of equal shocks $p_1 = p_4$, 2.27 simplifies to

$$\frac{p_2}{p_1} = \frac{p_3}{p_4} = \frac{\alpha + 2 - \frac{p_0}{p_1}}{1 + \alpha \frac{p_0}{p_1}}. \quad (2.28)$$

Which is the equivalent to the reflection of a shock wave from a solid boundary. Equation 2.27 has been solved numerically to find the difference between the post-collision reflected shock and the pre-collision LHS shock $\Delta p = p_2 - p_1$ for a range of shock pressures. The solution is shown in the form of a contour plot in figure 2.3.

2.2 Radiation Absorption

There are a number of physical mechanisms through which radiation can be absorbed in plasma. Which absorption mechanism are present depends on the intensity and spectral properties of the incoming radiation. For soft X-ray sources and lasers of moderate intensity ($10^{14} - 10^{15} \text{ W cm}^{-2}$) collisional absorption processes dominate. At higher intensities collisionless processes start to take over and these are often undesirable in the context of ICF compression. This section outlines the radiation absorption mechanisms that are pertinent to the discussions in this thesis.

2.2.1 Inverse Bremsstrahlung

The preferred mechanism of radiation absorption in ICF is a collisional process whereby an electron (in the presence of an ion to conserve momentum) is accelerated in the electric field of the light wave and then distributes its energy into the bulk plasma through collisions. This process is termed inverse bremsstrahlung because it is the reverse equivalent of bremsstrahlung emission. Inverse bremsstrahlung is preferred because the absorbed energy is distributed amongst the bulk of the electron population and then transported deeper into the target through thermal processes. For a Planckian X-ray radiation source, inverse bremsstrahlung absorption occurs up to the point where the plasma is sufficiently dense (and therefore opaque) to completely absorb the incoming radiation. The case of laser absorption is somewhat different and described in the next section.

2.2.2 Laser Absorption

The outstanding feature of the absorption of laser radiation in plasma is the presence of a critical density^{6,32}. Electrons in a plasma have a natural frequency at which they will oscillate when perturbed. This property is termed the plasma frequency and can be expressed by²⁶

$$\omega_{pe} = \sqrt{\frac{n_e e^2}{m_e \epsilon_0}}, \quad (2.29)$$

where n_e is the electron number density, e is the charge of the electron, m_e is the electron mass and ϵ_0 is the permittivity of free space. A light wave propagating through the plasma

with a frequency lower than the plasma frequency will be critically damped. As the plasma frequency is a function of the electron density, there exists a critical density beyond which the propagation of laser radiation is damped. Rearranging equation 2.29, this critical density can be expressed by⁶

$$n_{\text{crit}} = \frac{m_e \epsilon_0 \omega_L^2}{e^2} \quad (2.30)$$

which is approximated by $n_{\text{crit}} = 1.1 \times 10^{21} \lambda_L$ where λ_L is the laser wavelength in μm . For moderate laser sources, energy will be absorbed via inverse bremsstrahlung up to the critical density at which point the light is reflected. For higher laser intensities ($10^{15} - 10^{16} \text{W cm}^{-2}$) undesirable collisionless processes become important. An example of such is the absorption of radiation energy through non-linear three-wave coupling in which the incoming light wave can resonantly excite two new waves in the plasma. These processes are collectively referred to as parametric instabilities and are discussed in some more detail in the next section.

2.2.3 Parametric Instabilities

Parametric instabilities become important when the laser intensity is high enough for the oscillation energy of electrons in the light field to become comparable their thermal energy. They occur at specific points in the plasma where the resonance conditions are met. The resonance conditions are³³

$$\omega_L = \omega_1 + \omega_2, \quad (2.31)$$

$$\mathbf{k}_L = \mathbf{k}_1 + \mathbf{k}_2, \quad (2.32)$$

ω represents frequency, \mathbf{k} the wavenumber, the subscript L is for the laser properties and 1 and 2 the properties of the decay products. Discussed here are the instabilities two-plasmon decay (TPD), stimulated Brillouin scattering (SBS) and stimulated Raman scattering (SRS). TPD is the decay of an electromagnetic wave into two counter-propagating electron plasma waves^{6,33}. The resonance conditions are met when $\omega_1 = \omega_2 = \omega_{pe} = \omega_L/2$. Equation 2.30 shows that this condition is only satisfied at one position in the plasma, where the density is $n_{\text{crit}}/4$. For this reason TPD is suppressed in regions with steep density profiles.

SBS is the decay of an electromagnetic wave into a back-scattered electromagnetic wave and

a forward propagating ion-acoustic wave^{6,33}. The ion-acoustic wave will have a low frequency and as such, the resonance conditions can be met anywhere in the plasma up to the critical density. Therefore, SBS becomes an efficient process in plasmas with a long scale length.

SRS is the decay of an electromagnetic wave into a (forward or backward) scattered electromagnetic wave and an electron-plasma wave^{6,33}. As the electron-plasma wave will have a frequency of $\sim \omega_{pe}$ the resonance conditions dictate that SRS can only occur up to $n_{\text{crit}}/4$. As with SBS, plasmas with long scale lengths are susceptible to SRS.

Absorption of laser light through SRS and TPD can be detrimental in the context of ICF compression as the energy is deposited preferentially into a small population of electrons; this creates a number of hot electrons which can penetrate past the shock front and go on to pre-heat the fuel.

2.3 Thermal Energy Transport

In the previous discussion of energy transfer in fluids, the thermal flux term \mathbf{q} was neglected. In this section, the transfer of energy due to thermal conduction is discussed in more detail. We begin with the Eulerian energy transfer fluid equation 2.4 but only consider the internal energy terms. Subtracting the kinetic energy terms and expressing in 1D gives³⁰

$$\frac{\partial}{\partial t}(\varepsilon) + \nabla \cdot (\varepsilon \mathbf{u}) + \nabla \cdot (p \mathbf{u}) + \nabla \cdot \mathbf{q} = C_{ei}(T_i - T_e), \quad (2.33)$$

the collisional term on the RHS represents the energy exchange with the ion fluid, T_i is the ion fluid temperature and T_e is the electron fluid temperature. The heat flux is dependent on the temperature gradient and is given by Fourier's law

$$\mathbf{q} = \chi(T) \nabla T, \quad (2.34)$$

where χ is the thermal conductivity coefficient. To solve the energy transport equation one must find an expression for the thermal conductivity. The full treatment of thermal energy transport is quite involved and as such is not described here in full. Instead, a brief overview of the key points of the theory is given.

2.3.1 Thermal Conductivity

The standard approach is to use the transport coefficients from the work of Spitzer and Härm³⁴. The Spitzer-Härm theory is a kinetic treatment which solves the Fokker-Planck equation numerically accounting for interactions among the ions and electrons (Fokker-Planck is a collisional form of the Boltzmann equation). The Spitzer-Härm treatment has been extended to include degenerate effects that become relevant at high densities^{35,36} (for example in compressed ICF capsules). However, it is well known that Spitzer-Härm transport theory fails to accurately describe thermal transport in the presence of steep temperature gradients.

2.3.2 Thermal Flux Limit

For sufficiently steep gradients, Spitzer-Härm theory over-predicts the level of heat transport and may exceed the free-streaming limit, the maximum possible flow of thermal energy given by $q_{fs} = nkTv_{th}$, where v_{th} is the thermal velocity. There are many possible explanations for this phenomenon, including deviations from Maxwellian electron distributions, turbulence, induced magnetic fields, plasma instabilities and more³⁰. There is however, no theory that adequately assesses the contribution of all these effects. Instead, hydrodynamic simulations typically account for this by taking the minimum of either the classical heat flux due to Spitzer-Härm or the product of the free streaming limit with a flux limiter. In computer modelling the flux limiter is a user-defined parameter the value of which typically lies around $0.03 < f_{lim} < 0.10$ ⁶. Whilst not a very sophisticated solution, this approach has proven to be quite effective at replicating experimental observations.

2.3.3 Coupling to Ions

This section on thermal transport is finished with a brief discussion on the inclusion of collisions into the theory. Collisional terms appear in the expressions for electrical and ion thermal conductivity coefficients as well as the C_{ei} term in the energy transfer equation itself. Collisions are incorporated into the conductivity coefficients via the inclusion of Coulomb logarithms. In the energy transfer equation 2.33, the term on the RHS accounts for the

equilibration of the electron temperature to the ion temperature through collisions. This is determined by the temperature differential and some characteristic relaxation time τ_{eq} , where $C_{ei} = 3n_i k / 2\tau_{eq}$.

2.4 Radiation Hydrodynamics

Radiation hydrodynamics is the incorporation of radiative heat and momentum transfer into the fluid transport equations. In-depth descriptions of radiation hydrodynamics can be found in references 30, 37 and 38. The transfer mechanisms of radiation and matter are dependent on the opacity of the material, which itself is a function of density, temperature and composition. It is convenient to refer to the optical depth of a material when discussing radiation transport. Optical depth is a measure of the opacity of a material and is defined by³⁰

$$\tau = \int_0^{\Delta s} k_\nu dl. \quad (2.35)$$

where the dl element refers to a path through the material, Δs is the depth into the material and k_ν is the absorption coefficient of the material. A material with a high opacity will have a large optical depth and is said to be optically thick. Conversely, a material with a small optical depth is said to be optically thin.

In the extreme case of an optically thin plasma, the radiation is coupled to the fluid predominantly through emission and radiative cooling; there is little momentum coupling between the radiation and matter. On the other hand, in an optically thick plasma, absorption dominates and the mean free path of the photons is negligible compared to the scale of the system. Under these conditions the radiative flux is effectively zero. In this case, the radiation can be assumed to be in equilibrium with the matter; the energy, pressure and momentum of the two are combined. Radiation hydrodynamics is required in the regimes between the extremes of optically thin and thick plasmas, where there is significant coupling of the radiation energy and momentum into the matter. The treatment of radiation transfer is very similar to that of the Eulerian fluid equations discussed earlier.

2.4.1 Radiation Transport Equation

In radiation hydrodynamics the radiation field is treated as a third fluid in a similar manner to that of the electrons and ions. The radiation fluid consists of a distribution of massless particles each with an associated frequency. The equivalent property to the particle number density is the specific intensity I_ν defined by³⁰

$$I_\nu(\mathbf{r}, \mathbf{n}, t) = ch\nu f(\mathbf{r}, \nu, \mathbf{n}, t), \quad (2.36)$$

where c is the speed of light, h is Planck's constant, ν is frequency and $f(\mathbf{r}, \nu, \mathbf{n}, t)$ is the photon distribution function. The photon distribution function is defined as the number of particles at spatial position \mathbf{r} , frequency ν , travelling in the direction \mathbf{n} at time t . The radiation transport equation has a similar form to the Boltzmann equation and is expressed by

$$\frac{1}{c} \frac{\partial I_\nu}{\partial t} + \mathbf{n} \cdot \nabla I_\nu = j_\nu - k_a I_\nu + \sigma_{\text{scatter}}, \quad (2.37)$$

where j_ν is the emission coefficient, k_a is the absorption coefficient and σ_{scatter} encompasses all the radiation scattering terms.

2.4.2 Radiation in the Euler Equations

Radiation can be incorporated into the plasma fluid equations through the addition of the radiation field terms. As with the plasma fluid equation, the radiation terms arise from taking moments (this time angular moments) of the radiation transport equation. Adding those terms into the original Eulerian fluid equations 2.6 and 2.7 gives³⁰

$$\frac{\partial \rho \mathbf{u}}{\partial t} + \rho (\nabla \cdot \mathbf{u}) \mathbf{u} = \mathbf{F} - \nabla \cdot \mathbf{P} - \left(\frac{1}{c^2} \frac{\partial \mathbf{F}_r}{\partial t} + \nabla \cdot \mathbf{P}_r \right) + \frac{\mathbf{u}}{c^2} \left(\frac{\partial E_r}{\partial t} + \nabla \cdot \mathbf{F}_r \right), \quad (2.38)$$

$$\frac{\partial}{\partial t} \left(\frac{\rho}{2} u^2 + \rho \varepsilon + E_r \right) + \nabla \cdot \left[\rho \mathbf{u} \left(\frac{u^2}{2} + \varepsilon \right) \right] + \nabla \cdot (\mathbf{q} + \mathbf{P} \mathbf{u} + \mathbf{F}_r) = \mathbf{u} \cdot \mathbf{F} \quad (2.39)$$

The radiation terms, denoted by the subscript r, are the radiation energy density E_r , the radiative flux \mathbf{F}_r and the radiation momentum pressure tensor \mathbf{P}_r .

2.4.3 Approximate Descriptions of the Radiative Transfer Equation

For practical applications, the radiative transfer equation is too complex to yield useful solutions. Note that the absorption, emission and scattering terms in 2.37 are complex functions of radiation intensity, material composition, frequency, space and time. For this reason, one must resort to approximate descriptions of the radiation transport equation.

A diffusive form of the radiation transport equation can be found by applying a low order expansion and making the assumption of diffusive behaviour. This is known as the diffusion or Eddington's approximation. This derivation is quite involved so it is not written here but is included in appendix A (section 8.1). Instead, the diffusion equation is just stated:

$$\frac{1}{c} \frac{\partial I_\nu^{(0)}(\mathbf{r}, t)}{\partial t} - \nabla \cdot D(\nu) \nabla I_\nu^{(0)}(\mathbf{r}, t) = 4\pi j_\nu - (k_a + k_s) I_\nu^{(0)}(\mathbf{r}, t), \quad (2.40)$$

here $I_\nu^{(0)}(\mathbf{r}, t)$ represents an isotropic function of radiation intensity (often assumed to be a Planck function under LTE conditions) and the diffusion coefficient is given by $D(\nu) = 1/3(k_a + k_s)$. To find a solution to the diffusion equation it is necessary to calculate the absorption and scattering coefficients. These terms have a frequency dependence which can be handled in a couple of different ways. Either a Planckian distribution is assumed and the absorption coefficient is averaged over all frequencies, or the frequency is binned into multiple bands and an average absorption coefficient calculated for each frequency bin. The latter is called multi-group radiation transport and is able to handle more complex, non-Planckian radiation distributions. In any case, some amount of opacity averaging must be carried out. The subject of opacity averaging is discussed in more detail in the next section.

The final approximation used in radiation transport is needed in the case of optically thin plasmas where the diffusive approximation breaks down. The assumption made for diffusive transport was that the mean free path of the photon is small and the radiative flux is effectively zero which is not true if the plasma is optically thin. In the most extreme case this can cause the diffusion equation to calculate an energy transfer rate above the speed of light which is obviously impossible. The diffusion equation is so convenient however, that it is more simple to use ad-hoc flux limiter (similar to flux limiting in thermal transport).

2.4.4 Opacity Averaging

To solve the radiation diffusion equation values for the emission, absorption and scattering coefficients must be found. In order to do this, the combined contributions from all of the absorption and scattering processes present in the plasma must be summed. As mentioned in the previous section, the frequency dependence of these coefficients can be handled by averaging over a range of frequencies. There are two possible techniques for opacity averaging, the Planck mean and the Rosseland mean.

In an optically thin regime, the plasma is dominated by emission; absorption and scattering can be neglected and the Planck mean can be used. Under the assumption of LTE the total emission can be expressed as the product of the absorption coefficient k_a and black-body Planck function B_ν^P . The Planck mean is then defined as³⁰

$$k_a^{(P)} = \frac{\int_{\nu_{g-1}}^{\nu_g} k_a B_\nu^{(P)} d\nu}{\int_{\nu_{g-1}}^{\nu_g} B_\nu^{(P)} d\nu}. \quad (2.41)$$

If the plasma is optically thick, the diffusive approximation is valid and the Rosseland mean can be used. A consequence of the diffusive approximation is that the total radiative flux is related to the isotropic radiation intensity by

$$\mathbf{F}_r(\mathbf{r}, t) = - \int_0^\infty D(\nu) \nabla I_\nu^{(0)}(\mathbf{r}, t). \quad (2.42)$$

If thermodynamic equilibrium is assumed $I^{(0)}$ is related to the Planck function by $I^{(0)} = 4\pi B_\nu^{(P)}(T)$. We can now use $\nabla B_\nu^{(P)} = \frac{\partial B_\nu^{(P)}}{\partial T} \nabla T$ to find an expression for the Rosseland mean opacity³⁰

$$k_a^{(R)} = \frac{\int_{\nu_{g-1}}^{\nu_g} D(\nu) k_a \frac{\partial B_\nu^{(P)}}{\partial T} d\nu}{\int_{\nu_{g-1}}^{\nu_g} D(\nu) \frac{\partial B_\nu^{(P)}}{\partial T} d\nu}. \quad (2.43)$$

2.5 Radiation Waves and Ablation

The physical process of ablation occurs when high intensity radiation irradiates a material. The outer surface of a material is vaporised, ionised and then heated, causing it to expand. Through Newton's third law, the momentum flux out of the surface of the material must

be balanced by a compression force acting into the surface. The dynamics of the ablation is dependant on the speed of the radiation heat wave relative to the sound speed of the plasma. This section outlines the physics of ablation which is central to the many of the discussions in this thesis. To begin with, a description is given of radiation diffusion waves in high- Z materials. From there, the discussion moves onto low- Z materials in which case stationary ablation can be assumed.

2.5.1 Thermal Waves

Before discussing ablation in detail a general description of thermal waves must be given. When a flux of radiation enters a material, it will heat a surface layer. Then, as the absorption coefficient decreases with temperature, the radiation can penetrate further in. In this way, a thermal wave with a sharp temperature front is set up. This section continues with a discussion of some of the different forms these heat fronts can take.

In general, the propagation of the heat front will either be subsonic or supersonic (although transonic behaviour exists between these two limits). Supersonic behaviour refers to the case where the thermal radiation wave travels faster than the sound speed of the heated material. In this case, the heat front will traverse into the material without significantly perturbing it. For a subsonic thermal wave, the heat front is slower than the sound speed. The material is heated and sets up a pressure gradient which develops into a shock front. The resulting structure is a shock wave travelling into the material supported by the radiation heat wave. The penetration of a radiation wave into a material can pose a difficult problem and the radiation transfer equation is often solved numerically. However, under certain conditions, it is possible to derive analytical solutions, making some assumptions. For diffusive radiation waves, this class of solvable problems is often referred to collectively as Marshak waves³⁹. There exists a wide range of literature on the analytical treatment of Marshak waves⁴⁰⁻⁴³. One of these solutions is considered in more detail later but first, a discussion is given on the transition point between the supersonic and subsonic regimes.

At early times, or for very high temperatures, the propagation of a radiative heat front will be supersonic. In the supersonic regime the hydrodynamic motion can be considered negligible. In this case, one can remove the kinetic terms and take only the radiation terms

in equation 2.39, dropping the velocity dependent terms and ignoring the change of radiation energy density gives the simple diffusion relation

$$\rho \frac{\partial \varepsilon}{\partial t} = \rho c_v \frac{\partial T}{\partial t} = -\nabla \cdot \mathbf{F}_r, \quad (2.44)$$

assuming constant density and specific heat c_v . The flux term can be expressed as the negative of the temperature gradient multiplied by the thermal conductivity κ , so in 1D the relation becomes

$$\rho c_v \frac{\partial T}{\partial t} = \frac{\partial}{\partial x} \left(\kappa \frac{\partial T}{\partial x} \right). \quad (2.45)$$

We can make the simple assumption that the temperature behind the heat front is constant; the LHS of equation becomes zero and therefore, the flux is constant in space. If we relate the flux to the rate at which the material is heated, using $\kappa = (4\sigma T^3)/3k_a^{(R)}$, we get

$$\rho \varepsilon_0 \frac{dx_p}{dt} \approx \frac{4\sigma T_0^4}{3k_a^{(R)} x_p}, \quad (2.46)$$

where x_p is the penetration distance of the heat front. The solution for equation 2.46 is³⁰

$$x_p = \left(\frac{8\sigma T_0^4}{3k_a^{(R)} \rho \varepsilon_0} t \right)^{\frac{1}{2}}. \quad (2.47)$$

The \sqrt{t} dependence of the penetration distance shows how the speed of the heat front decreases. At a certain point, the heat front will drop below the sound speed in the heated material. At this time a shock front will overtake the heat front and the subsonic regime is entered. The next section discusses a solution for this regime.

2.5.2 Diffusive Radiation Waves in High-Z Materials

The standard approach for finding solutions to Marshak wave problems is to seek self-similar solutions through dimensional analysis. A detailed discussion of dimensional analysis can be found in reference 44. The specific problem discussed here is from reference 40 in which the assumption of infinite density at the ablation front is used to yield a self-similar solution. We follow the application of this method as in section 7.4 of reference 6 to find the following

scaling relations for gold

$$p_a = 22q_0^{10/13}(f_R t)^{-3/26}\text{Mbar}, \quad (2.48)$$

$$S_r = \sigma T_0^4 = 10q_0^{16/13}(f_R t)^{8/13}\text{W/cm}^2, \quad (2.49)$$

where p_a is the pressure at the ablation front, q_0 is the absorbed flux in units of $1 \times 10^{14} \text{ W cm}^{-2}$, t is time in ns, f_R is a reduction factor to approximate the opacity of gold and S_r is the radiation flux re-emitted from the heating wave in units of $1 \times 10^{14} \text{ W cm}^{-2}$. Inserting values into the equations shows that high-Z materials are poor ablaters but efficient radiation reflectors. For a 5 ns long pulse of $1 \times 10^{14} \text{ W cm}^{-2}$ only 1.9 Mbar is generated but the re-emitted flux exceeds the absorbed flux at $1 \times 10^{15} \text{ W cm}^{-2}$. The gold material couples only a small portion of energy into fluid motion but after 5 ns is reflecting 90% of the incoming radiation. This feature will become important later in the discussion of indirect drive and hohlraums.

2.5.3 Ablation Pressure Scaling in Low-Z Materials

In the discussion of high-Z materials the radiation waves were assumed to propagate diffusively. This approach is not valid for low-Z materials as the ablative blow-off is optically thin and diffusive behaviour is not a correct assumption. Instead, it can be assumed that the blow-off is effectively transparent to incoming radiation. For X-ray radiation this means that the energy will be entirely deposited at the ablation front, where the plasma is sufficiently opaque to completely absorb the radiation. This case is known as stationary ablation. A similar treatment can be used for laser driven ablation but with the assumption that the energy is deposited at the critical density and then transported to the ablation front through a conduction layer.

Stationary ablation can be modelled in a similar manner to the RKH jump conditions. The derivation here largely follows that given in reference 45. Incorporating the radiative flux into the boundary q_r , into the Euler fluid equation for energy 2.7 and integrating over space gives

$$e_2 + \frac{u_2^2}{2} + \frac{p_2}{\rho_2} + \frac{q_r}{\rho_2 u_2} = e_1 + \frac{u_1^2}{2} + \frac{p_1}{\rho_1}. \quad (2.50)$$

The q_r term is not the same as the external flux that reaches the ablation front q_{ex} . Some energy must be deposited in the blow-off to keep it isothermal and therefore, not all the energy is deposited at the ablation front. This is accounted for by including a term for the power required to keep the gas isothermal $q_{\text{ex}} = q_r + p_1 3/2 V_1^{1/2}$. Now, combining 2.50 with the mass and momentum jump relations 2.20 and 2.21 and an ideal gas equation of state ($\gamma = 5/3$) gives the Hugoniot condition

$$q_{\text{ex}} = p_2^{3/2} V_2^{1/2} + \sqrt{\frac{p_2 - p_1}{V_1 - V_2}} \left(\frac{3}{2} p_2 V_2 - \frac{3}{2} p_1 V_1 + \frac{1}{2} (p_1 + p_2) (V_2 - V_1) \right). \quad (2.51)$$

There exist two forms of solution for equation 2.51 that correspond to the subsonic and supersonic heating regimes discussed previously. The transition between them occurs at the point where the isothermal sound speed in the blow off is the same as the fluid velocity $c_T = u_1$. The isothermal sound speed in a plasma is expressed by⁴⁵

$$c_T = \left(\frac{T_R R}{\mu} \right)^{1/2}, \quad (2.52)$$

where T_R is the radiation temperature of the external Planckian flux, R is the ideal gas constant and μ is the fully ionized mean molecular weight $\mu = A/(Z + 1)$. With that and using the Stefan-Boltzmann law $q_{\text{ex}} = \sigma T_R^4$, a critical temperature can be defined⁴⁵

$$T_{\text{crit}} = \left(\frac{4\rho_0}{\sigma} \right)^{2/5} \left(\frac{R}{\mu} \right)^{3/5}. \quad (2.53)$$

At drive temperatures above T_{crit} the ablation will occur in the supersonic regime. In that case the pressure is higher in the blow-off region and due to the isothermal condition it will scale linearly with the temperature of the drive radiation. In the subsonic regime, the maximum pressure occurs in the material ahead of the ablation front. Under the conditions of the low drive limit $q_{\text{ex}} \ll \rho_{\text{solid}} c_T^3$, the pressure ratio can be approximated by $p_0/p_1 = 2$, the density ratio approximated by $\rho_0/\rho_1 = q_{\text{ex}}/(\rho_{\text{solid}} c_T^3)$ and the relation in equation 2.51 approximated by $q_{\text{ex}} = 2c_T p_0 = 4\rho_1 c_T^3$. The expression for the pressure in the material is then

$$p_a = \frac{\sigma_B T_r^4}{\sqrt{4T_r(1+Z)k_B/Am_p}}. \quad (2.54)$$

The situation for laser ablation differs somewhat in that the laser radiation is only able to propagate up to the critical density. In this case, it can be approximated that the energy is deposited at the critical density and the assumption of stationary ablation can be applied from there. Ablation under laser drive always occurs subsonically due to the low density of the ablated material⁶. As with the X-ray case, the assumption of subsonic ablation in the low drive limit leads to a flux balance expressed by

$$I_L = 4\rho_c c_T^3, \quad (2.55)$$

where q_{ex} has been replaced by the laser intensity I_L . The difference here is that the point of absorption is determined by the critical density $\rho_c = (Am_p/Z)n_c$. Again, using the low drive approximation $p_a = I_L/(2c_T)$ and inserting the expression for the critical density 2.30 gives

$$p_a = (I_L/\lambda_L)^{2/3} \left(\frac{Ze^2}{2Am_p\pi m_e c^2} \right). \quad (2.56)$$

2.6 Indirect Drive

There has already been some discussion given on the coupling X-ray radiation into material but nothing in-depth has been said on how such sources are generated. In ICF experiments X-rays are generated through the heating of a high-Z cavity called a hohlraum. Hohlräume are typically made from gold and take a cylindrical shape due to the ease of manufacturing them in this way³³. Rather than irradiating a payload directly with the source (e.g. laser, ion beam, z-pinch), the hohlraum interior is irradiated which in turn produces a near blackbody radiation field that drives the a payload, hence the term indirect drive. The payload is typically a surface on the one of the hohlraum walls or, in the case of ICF implusions, a capsule suspended in the centre of the hohlraum. The real benefit of indirect drive is the potential uniformity of radiation field over the payload surface. However, there are additional benefits in that indirect drive avoids the fact that monochromatic and spatially coherent laser light is susceptible to fluid and parametric instabilities. The downside of indirect drive is that a lot of the drive energy manifests itself as thermal energy in the hohlraum wall, so the coupling to the payload is less efficient.

2.6.1 Laser to X-ray Conversion

There exist a number of drive options for hohlraum heating but here the discussion is focussed on laser heated hohlraums. Section 2.5.2 already outlined how high-Z materials can become efficient radiation reflectors. Initially X-rays are produced at the laser spot sites where the beams strike the wall heating them. As those spots heat up, they will emit X-ray radiation which transports to the other parts of the hohlraum wall. As the travel time of the photons is significantly lower than the variations in the drive power, an isotropic radiation field is rapidly set-up inside the cavity. To model the laser to X-ray conversion we consider the flux balance into a high-Z material.

The source term S_c (which includes the external heating source S_s and the influx from the rest of the hohlraum wall S_i) is balanced by the radiation absorbed S_a in the wall plus the radiation reflected from the wall S_r so that³³

$$S_c = S_i + S_s = S_a + S_r. \quad (2.57)$$

In a closed hohlraum, one has $S_i = S_r$ and $S_a = S_s$ but real hohlraums will have entrance holes for the drive source and an absorbing surface (e.g. fuel capsule) that will receive but not emit radiation. This can be accounted for by using a loss fraction f , which gives

$$S_i = (1 - f)S_r. \quad (2.58)$$

It is also useful to define a wall albedo α , as the ratio of the incoming flux into the wall to the reflected flux or

$$\alpha = S_r/S_c \quad (2.59)$$

We can then use these to relate the source flux to the absorbed and reflected flux by³³

$$S_r = \frac{S_s}{f + (1 - \alpha)/\alpha}, \quad (2.60)$$

$$S_a = \frac{S_s}{1 + f\alpha/(1 - \alpha)}. \quad (2.61)$$

2.6.2 Time-dependent Laser to X-ray Conversion Scaling

In the simple analysis above it was assumed the the wall albedo was just a constant that related the reflected flux to the incoming flux. However, in reality, the wall albedo is a function of both time and the intensity of the incoming flux. In section 2.5.2 dimensional analysis was used to find such a relation for gold (see equation 2.49). An alternative approach is to find the scaling using 1D simulations. Such a study was carried out in reference number 46. The result for gold is shown below

$$S_r = 13S_a^{1.05}t^{0.46}. \quad (2.62)$$

The scaling is similar to equation 2.49 which is re-expressed here for comparison.

$$S_r = 10S_a^{16/13}(f_R t)^{8/13} \quad (2.63)$$

These relations have used the assumption that S_a that is constant in time. This is not the case in ICF as the drive source will have a shaped profile in order to set the adiabat of the fuel and launch a series of shocks in the compression. For drive sources that vary in time, equations 2.62 and 2.63 will give incorrect predictions of S_r . A more accurate prediction is given by the approach in reference 47. This study proposed a more useful scaling of the form

$$S_r(t) = K_r[E_a(t, \mathbf{r})]^\alpha[S_a(t, \mathbf{r})]^\beta, \quad (2.64)$$

where α and β are constants and E_a is defined as

$$\frac{\partial E_a(t, \mathbf{r})}{\partial t} = S_a(t, \mathbf{r}). \quad (2.65)$$

As before, a self-similar solution can be found using dimensional analysis, which for gold gives

$$S_r = 14.1[E_a(t, \mathbf{r})]^{0.510}[S_a(t, \mathbf{r})]^{0.748}. \quad (2.66)$$

This time-dependent scaling law will be more accurate for ICF drive pulses that vary in time.

2.6.3 View-Factor Theory

The discussion of flux balances up until this point has assumed isotropic radiation fields. In reality, due to the geometry of the hohlraum and the existence of hotspots, the radiation field in the cavity will be non-uniform. It is necessary then to find how the radiation field emitting from the hohlraum wall translates onto a target surface. Such techniques are termed view-factor calculations.

The view-factor between two surfaces is defined as the fraction of radiation emitted from one surface that is incident on the second. The view-factor dF_{ij} , between two infinitesimal surface elements i and j is defined as

$$dF_{ij} = \frac{\cos(\theta_i) \cos(\theta_j)}{\pi r_{ij}^2} dA_j, \quad (2.67)$$

where θ_i and θ_j are the angles between the vector connecting the centre points of the surfaces r_{ij} and the surface's normal vector and dA_j is the area of surface element j . Integrating over the emitting and incident surface then gives

$$F_{12} = \frac{1}{A_1} \int_{S_1} \int_{S_2} \frac{\cos(\theta_i) \cos(\theta_j)}{\pi r_{ij}^2} dA_j dA_i. \quad (2.68)$$

In combination with the time-dependent albedo relations derived earlier, the view-factor method can be used to fully describe the radiation field incident on a surface.

2.7 Inertial Confinement Fusion

In Inertial Confinement Fusion (ICF) the aim is to compress a a pellet of deuterium-tritium (DT) to sufficient density and temperature in order to trigger ignition. Ignition is loosely defined as the point at which the energy deposited from the fusion alpha particles is enough to overcome the energy losses and therefore sustain a burning fuel. In the field of magnetic confinement fusion the point of ignition is usually defined by the Lawson criterion⁴, which is a function of particle density and confinement time. In ICF the Lawson criterion cannot be used because there is no way to directly measure the confinement time. A number of studies have attempted to address this by defining useful ignition metrics^{48–50}. This section

outlines some other common metrics used in ICF implosions and uses them to discuss the benefits of the shock ignition scheme.

2.7.1 Central Hotspot Ignition

A fusion fuel capsule typically consists of low-density DT gas surrounded by a layer of solid DT. When using indirect drive, one must use an ablator material (e.g. plastic) on the outer surface but this is optional under direct drive. The outer layer is irradiated and the resulting ablation accelerates the shell towards the centre of the capsule. As the shell converges inwards, it compresses the DT gas, increasing the pressure. The pressure in the gas continues to increase until it starts to resist the compression of the shell. At this point, resistive forces cause the shell to stagnate and the pdV work generates heat, creating a central hotspot. If the kinetic energy of the imploding shell is sufficient, the resultant heating will be enough to trigger ignition and fusion reactions will begin taking place in the gas. The alpha particles produced from the DT reaction then deposit their energy in the inner surface of the high-density DT shell. This energy deposition will heat the inner layer of the shell, making it transparent to the alphas and allowing them to penetrate further. In this way, a burn-wave is set-up that traverses through the fuel until it meets the rarefaction wave produced at the outer surface as a result of the ablation.

In order to ignite, the fuel must be compressed to a high density ($\sim 450 \text{ mg cm}^{-3}$)⁶. For the most efficient use of the driver energy, the fuel should be compressed isentropically, where the entropy remains constant. The entropy of the fuel is often measured in terms of the adiabat α , defined as the ratio of the fuel pressure to the pressure of a cold, Fermi-degenerate DT gas. In ICF implosions the fuel adiabat is typically kept around a value of 1.5-4⁶. This near-isentropic compression is achieved by superimposing a sequence of increasingly strong shocks. The launching of the shocks must be carefully timed such that the shocks coalesce at the same time. The process just described is termed central hotspot (CHS) ignition.

Before discussing some drawbacks of CHS and the advantages of alternative schemes it is useful to define some implosion metrics. Firstly, the burn fraction θ_b is the fraction of the

total fuel burned and is given by⁶

$$\theta_b = \frac{1}{1 + 7/\rho R}. \quad (2.69)$$

where ρR is the areal fuel density, the product of the radius and fuel density. The gain G , is defined as the ratio between the fusion energy yield and the drive energy on target. For a direct drive target, the gain can be simply approximated by⁵¹

$$G \simeq \frac{73}{I_{15}^{0.25}} \left(\frac{3 \times 10^7}{v_I} \right)^{1.25} \left(\frac{\theta_b}{0.2} \right), \quad (2.70)$$

where I_{15} is the laser intensity in units of 10^{15}W cm^{-2} and v_I is the implosion velocity. In the derivation of equation 2.70 it was assumed that ignition has already been achieved but to achieve ignition, the drive energy must be above a threshold. This threshold ignition energy is approximated by⁵²

$$E_{\text{ign}} = 50.8\alpha^{1.9} \left(\frac{3 \times 10^7}{v_I} \right)^{-5.9} \left(\frac{p_a}{100 \text{Mbar}} \right)^{-0.8}. \quad (2.71)$$

where α is the fuel adiabat, the ratio between the fuel pressure and the Fermi degeneracy pressure. The final useful parameter is the in-flight aspect ratio (IFAR). The IFAR is the maximum value of the ratio between the shell radius and thickness. The IFAR is approximated by⁵³

$$\text{IFAR} \simeq \frac{51}{\langle \alpha \rangle^{0.6}} \left(\frac{v_i}{3 \times 10^7} \right)^2 I_{15}^{-4/15}. \quad (2.72)$$

2.7.2 Shock Ignition

Equation 2.71 shows how the energy required for ignition decreases with increasing implosion velocity. For this reason the CHS scheme uses high implosion velocities of $\geq 370 \text{ km s}^{-1}$ ⁵⁴. However, equation 2.70 shows that, once ignition has been achieved, the gain actually decreases with implosion velocity. Further to this, high implosion velocities may be more susceptible to hydrodynamic instabilities. Hydrodynamic instabilities place an upper bound on the IFAR. As the IFAR scales with implosion velocity, this gives further motivation to keep the implosion velocity low.

These issues establish the motivation for alternative, low implosion velocity ignition schemes. In these schemes, the slower implosion velocities used to assemble the fuel allow for potentially higher gains and may be more robust to hydrodynamic instabilities. However, these slower implosions will not reach the threshold for ignition. The solution then is to use an external trigger for ignition. In the shock ignition scheme this trigger is an extreme shock launched at a late stage of the implosion. The ignition of a pre-compressed fuel via a strong shock was first proposed by Shcherbakov⁵⁵ in 1983. The modern shock ignition scheme was first suggested by C. Zhou and R. Betti⁵⁶ published in full in 2008⁵⁷. The progress made in understanding the shock ignition scheme was reviewed in 2014^{58,59} and 2016⁶⁰.

The compression stage of shock ignition is similar to that of CHS. The shell is accelerated inwards via ablation of the outer surface until the pressure of the central gas becomes enough to resist the implosion. However, this time the kinetic energy of the shell is not sufficient to trigger ignition on its own. Instead ignition is triggered via an extreme shock launched at a late stage in the implosion. The ignition shock is timed such that it should collide with the rebounding shock (from the stagnation phase) near the inner surface of the shell. As laid out in section 2.1.6, this will result in two new shocks. One convergent shock travelling back to the centre of the capsule and one divergent towards the outer surface. Ignition occurs when the convergent shock causes further heating of central fuel. Crucially this must happen before the diverging shock reaches the outer shell surface, triggering target disassembly. The dynamics of this implosion are outlined graphically in figure 2.4 taken from reference number 61.

At the time of ignition, a shock ignition assembly will be isochoric as opposed to a CHS assembly which is isobaric. It has been shown that the ignition energy of such an isochoric scheme is significantly lower than that of an isobaric scheme; another factor contributing to the potential for high gains⁵⁷.

The shock ignition scheme is highly desirable not only because the low implosion velocity allows for high gains and low levels of fluid instability but also because the intensities required ($< 10^{16} \text{W cm}^{-2}$) are reachable on existing facilities. A number of studies have focused on the design and refinement of shock ignition schemes^{23,62-65}. More recent studies have demonstrated the achievement of shock ignition like pressures under direct drive⁶⁶⁻⁶⁸. The key

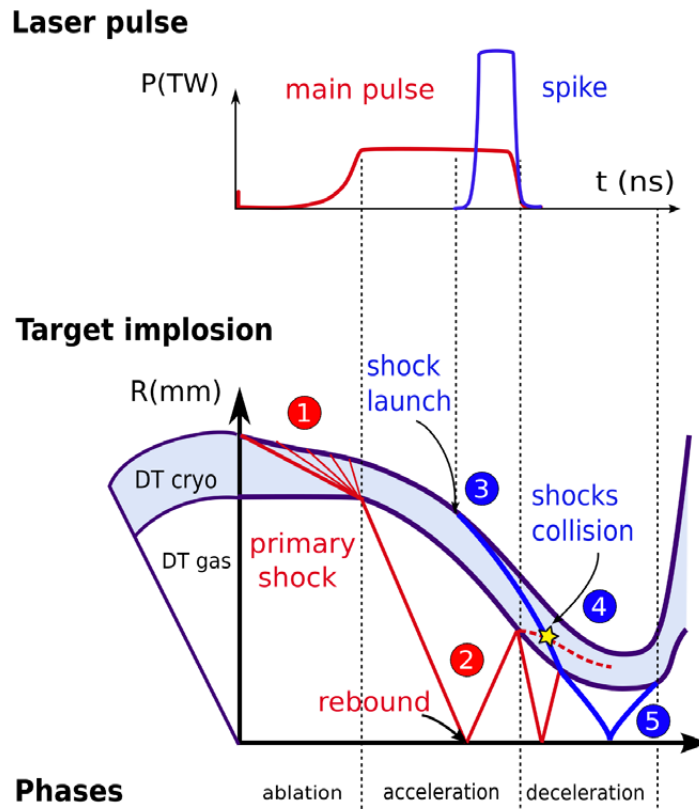


Figure 2.4: A diagram of the dynamics of shock ignition from reference 61. (1) Ablation at the outer surface causes near-adiabatic compression of the fuel and acceleration of the shell. (2) Rebound of the compression shock at the centre of the capsule and the shell begins to decelerate. (3) The ignition shock is launched via a sharp increase in the laser drive power. (4) The rebounding compression shock collides with the ignition shock in the shell. (5) A combination of heating from the shock and resistive forces trigger ignition.

question still to be answered is the role that parametric instabilities and the hot electrons they produce will play, as they become significant at shock ignition relevant intensities^{61,69,70}.

Some studies have suggested that, if their energy is low enough, the hot electrons produced through parametric instabilities could enhance the pressure in the igniter shock^{71,72}.

Historically the shock ignition scheme has been considered only possible using direct drive^{23,58}.

This is mostly due to the thermal capacity of hohlraums causing some temporal lag the conversion to X-rays making fast rising drive profiles difficult to achieve. This assumption is addressed in this thesis. Firstly in Chapter 5, a study looking at the ablation pressure and drive parameters required for an indirect drive shock ignition scheme. Then partly in Chapter 6 that discusses using burn-through barriers as a technique for generating fast rising hohlraum temperatures at late drive times.

Chapter 3

Description of Codes

This chapter gives an overview of the three numerical codes used to carry out the work in this thesis. The first is the Lagrangian radiation hydrodynamics code HYADES. HYADES was used predominantly to model the coupling of radiation to targets and the resulting fluid motion. The second code is h2d, the 2D version of HYADES. h2d is used in the study of hohlraums to model the conversion of laser to X-ray drive. The description of the HYADES and h2d codes given here largely follows documents on the Cascade Applied Sciences inc website⁷³ and references 30 and 74.

The third code is a view-factor code called F3D developed by J. Owen at the University of York. This code was used in 3D simulations of hohlraums to measure the spatial distribution of radiation fields. The description of the code here has been produced based upon documents supplied by J. Owen.

The physics basis for this chapter was outlined in detail in the previous theory chapter. Here a description is given of how the previously derived equations are implemented.

3.1 HYADES Code

3.1.1 Lagrangian Mesh and Hydrodynamics

The predominant physics package of HYADES is the fluid transport model. All other physical processes are coupled into the fluid transport package via source terms in the fluid momentum transfer equation. HYADES uses a Lagrangian co-ordinate system. Lagrangian systems

follow specific mass elements of the fluid and allow the mesh to move freely (in contrast Eulerian systems have a fixed mesh that is used to track how the spatial co-ordinates of the fluid change). The mesh positions x and velocities u are updated in the code following a von Neumann leap-frog method. First, the velocities are updated at every half time-step using the momentum equation

$$\frac{u_j^{n+\frac{1}{2}} - u_j^{n-\frac{1}{2}}}{\Delta t^n} = - \frac{\left[(p+Q)_{j+\frac{1}{2}}^n - (p+Q)_{j-\frac{1}{2}}^n \right]}{\rho_j \left(x_{j+\frac{1}{2}} - x_{j-\frac{1}{2}} \right)}, \quad (3.1)$$

where superscript denotes the time-step, the subscript denotes the mesh point and the Q terms are viscosity terms. The pressures and the viscosities are calculated using the known density, temperature and the equation of state of the material. The additional source terms from thermal transport, radiation etc. are added to the RHS of equation 3.1. Once the mesh velocities are calculated, the positions are then updated at the end of the integer time-step according to

$$\frac{x_j^{n+1} - x_j^n}{\Delta t^{n+\frac{1}{2}}} = u_j^{n+\frac{1}{2}}. \quad (3.2)$$

In Lagrangian geometry the movement of the mesh can cause issues at later times in the simulation. Regions that decrease significantly in density will lose spatial resolution as the mesh expands. This requires the mesh to be carefully set-up in order to assure spatial resolution is maintained. In two dimensions, this problem becomes significantly more pronounced. The additional degree of freedom can allow the mesh to entangle forming bow-ties. For this reason, the hydrodynamic package in h2d is more sophisticated and allows for manipulation of the mesh during simulations.

Lagrangian meshes can also struggle to model discontinuities as the scale length of the discontinuity may be smaller than the mesh size. HYADES manages this by applying an artificial viscosity⁷⁵, which acts to spread out the shock front over a number of cells whilst obeying the Rankine-Hugoniot conditions. The artificial viscosities are encompassed along with the real viscosities in the Q term in equation 3.1.

3.1.2 Thermal Transport

In HYADES, the thermal heat transport is handled using the flux-limited Spitzer-Härm model outlined in section 2.3. First, the rise in temperature due to pdV work is calculated using the pressure from the equation of state and the volume change from the hydrodynamics package. Next, the electron-ion collisional term is calculated along with the electron and ion diffusion coefficients. These are then used to solve the diffusion equation for both the ion and electron fluid. Once the diffusion equation has been solved the temperatures are updated for the next time step.

3.1.3 SESAME Equation of State

The equation of state of a material relates the properties of matter (e.g. pressure, temperature density) to each other given a set of physical conditions. The hydrodynamics and the thermal transport in materials are both functions of the equation of state. In HYADES the known values in the material are the mass, density and temperature. The equation of state is used to relate these to specific energy and pressure.

HYADES implements equation of state through the inclusion of look-up tables. The simulations in this thesis used the SESAME look-up tables⁷⁶. The SESAME tables are calculated using a number of theoretical models in the different regions of phase space of the material. The SESAME tables are maintained by the Los Alamos National laboratory.

3.1.4 Radiation Transport

The HYADES simulations in this thesis used a multi-group radiation transport package. This was already described in section 2.4. Radiation transport is handled by solving the radiation transport equation

$$\frac{\partial U_g}{\partial t} + P_g(\nabla \cdot \mathbf{u}) + \nabla \cdot \mathbf{F}_g = c\kappa\rho \left(\frac{4\pi}{c} B_g - U_g \right) \quad (3.3)$$

where the subscript g denotes the radiation group, all other terms were defined in chapter 2. The first step is to find the 2nd term on the LHS which is related to the pdV work by $P_g(\nabla \cdot \mathbf{u}) = W_{pdV}/V$. This is done by using the volume change of the cell and the radiation

pressure, which is related to the volume via the ideal gas relation $P = V^{-\gamma}$, where $\gamma = 4/3$. The next step is to find the radiation density added from emission from the electron fluid (the terms on the RHS). To do this, one must first calculate the radiation absorption term. This term is calculated in the HYADES atomic physics and opacity package. The details of this calculation are described later in section 3.1.7. Then all the other terms on the RHS are known quantities. The flux term (third term LHS) is found using the diffusion approximation $\mathbf{F}_g = \chi_g \nabla U_g$. As with the radiation absorption term, the flux limited diffusion term is calculated in the atomic physics and opacity package. Finally, the coupling from the radiation fluid to the electron fluid needs to be accounted for. The energy added to the electron fluid is just the negative of the terms in the bracket on the RHS multiplied by the specific heat η , the group frequency ν_g and Planck's constant

$$\Delta E_g = \eta h \nu_g \left(U_g - \frac{4\pi}{c} B_g \right). \quad (3.4)$$

Then the pressure increase is $\Delta p = \frac{\Delta t}{3} V \nabla U^{n+1}$, which appears as a source term in the fluid equation.

3.1.5 Laser Absorption

There are multiple models in HYADES for handling the absorption of laser radiation but the model used for the simulations in this thesis was ray-tracing inverse-bremsstrahlung. Energy is deposited up to the critical density of the plasma according to the absorption coefficient. The absorption coefficient used is given by³⁰

$$\alpha = \frac{2^8 \pi^{\frac{5}{2}}}{3ch^3} \frac{e^6 \langle n_i (Z^*)^2 \rangle}{\omega_L^2 \left(1 - \frac{\omega_{pe}^2}{\omega_L^2} \right)^{\frac{1}{2}}} F_{\frac{1}{2}} \left(\frac{\mu_{\text{chem}}}{k_B T_e} \right) \left(1 - e^{-h\omega/2\pi k_B T_e} \right) \log(\Lambda_{ei}) [\text{cm}^{-1}], \quad (3.5)$$

where $F_{\frac{1}{2}} \left(\frac{\mu_{\text{chem}}}{k_B T_e} \right)$ is a Fermi-Dirac integral term that accounts for electron degeneracy and $\log(\Lambda_{ei})$ is the electron-ion Coulomb logarithm.

3.1.6 Ionization

There are several models for ionization used in HYADES. The models used in this thesis were the Saha and average-atom LTE models. The Saha model uses Boltzmann statistics to give the ratios of ion densities in successive ionisation stages. The model is dependent on the atomic structure of the atom, the plasma density and temperature. It is valid only for weakly ionised plasmas and is widely applicable.

The average-atom LTE model is required when plasma densities start to become high and the radiation field considerable (e.g. compressed ICF capsules). An average-atom model places emphasis on the population of ionisation levels (as opposed to densities of ions in particular states). In this way it can more accurately find frequency dependent absorption coefficients which means the model can support non-Planckian radiation fields. The model employed by HYADES is a screened hydrogenic LTE model⁷⁷. The model does not attempt to find the shell populations of many different atomic configurations but rather uses one sequence of levels whose occupation can be non-integer and is used to represent an average of the many different shell populations. The model uses a screening theory base upon a Wentzel-Kramers-Brillouin calculation, which gives the electron energy levels as a function of the shell populations. A Hartree-Fock approximation is used to replace the shell populations with their averages. LTE equations are then used to determine the shell populations.

3.1.7 Opacity

Opacity calculations in HYADES are handled with the atomic physics and opacity package. This takes the details of the populations of ionisation levels from the ionisation model being used. Once these populations have been found the package calculates the frequency-dependent absorption and diffusion coefficients for each of the frequency groups specified in the multi-group radiation transport model. The relevant atomic processes are free-free (absorption/emission through free electrons), bound-free (the liberation of an electron into the continuum or vice versa) and bound-bound (excitation or de-excitation of an electron into a different atomic level).

The bound-bound interactions can be calculated from the Einstein A and B-coefficients. The

bound-free are then found from Einstein-Milne relations (The generalisation of the Einstein relations to the continuum). Finally the free-free coefficients are found by considering the interaction of a free electron in a Coulomb field.

3.1.8 h2d

h2d is the 2D version of the codes HYADES. h2d uses a cylindrical geometry in which the axes are in the r and z directions. The computational grid is made up of a number of quadrilateral zones each defined by 4 vertices. The code then uses the z -axis as the axis of symmetry. In this way a rectangular mesh or disc mesh will simulate a cylindrical or spherical object respectively.

Much of the physics in h2d is the same as in HYADES. For example the zero dimensional packages (e.g. ionisation, opacity) are handled in the same way as in HYADES. The diffusive transport packages (thermal and radiation transport) are similar to the 1D case, just extended to 2D. Refraction of the laser is accounted for in the ray-tracing package. The major differences exist in the fluid transport package which manages the mesh acceleration and movement.

As in HYADES, the mesh accelerations are found by solving the momentum equation but this time the accelerations act on the zone vertices rather than interfaces. The assumption is made that the pressure in an adjacent zone acts isotropically between the two mesh vertices. The positions of the mesh vertices are then updated according to their change in velocity. The main issue arises from the potential for the mesh to become entangled due to non-uniform pressures and shear flow. h2d attempts to prevent this with the inclusion of artificial viscosities. These induce artificial pressures that act to untie any bow-tied zones. Even with the artificial viscosities, the h2d mesh can still become entangled. In the event of a bow-tie h2d has a manual re-meshing function in which the user can re-organise the mesh to undo any bow-ties. There also exist a number of semi-automated rezoning schemes.

3.2 F3D code

The F3D code calculates the transfer of radiation between surfaces. It works by solving the radiosity equation for a number of individual surface elements that comprise a complex surface geometry. The radiosity equation expresses the radiation flux from a surface as

$$I_i = \sigma T_i^4 + \alpha_i \sum_{j=1}^n F_{ij} I_j, \quad (3.6)$$

where the first term is the blackbody radiation from the surface and the second term is the radiation reflected due to incident radiation from all other surfaces (this mimics re-emission), α_i is the albedo and F_{ij} is the surface view-factor.

The problem is broken down into a number of triangular surface elements. This is imported in the form of an .stl file which can be created in any 3D modelling software (e.g. blender). Each triangular surface element is defined by three vertices and a unit normal surface vector. The spatial resolution of the simulation is determined by the size of these surface elements. Each of these surface elements is assigned an albedo value. A hot gold wall for instance, may have an albedo of 0.9 meaning it reflects 90% of the incident radiation. An albedo of 0 can be used to represent a loss surface that reflects no radiation (e.g. laser entrance hole in a hohlraum). Additionally each surface may include an emitting source via inclusion of an emission term in the radiosity equation. In this way radiating surfaces (e.g. laser hot spots in a hohlraum) may be included in the simulations. Once the stl file has been imported, the surface geometry is known and the view-factors can be calculated using the equation from section 2.6.3

$$F_{12} = \frac{1}{A_1} \int_{S_1} \int_{S_2} \frac{\cos(\theta_i) \cos(\theta_j)}{\pi r_{ij}^2} dA_j dA_i. \quad (3.7)$$

Then, after the view-factors have been determined, the radiosity equation can be solved. The solution of this equation will then yield the flux distribution across all surfaces.

Chapter 4

Soft X-ray Driven Ablation Pressure Scaling for Low-Z to Mid-Z Materials

This chapter describes work investigating the ablation pressure scaling under indirect drive for a number of different materials. First, an outline is given on the physics of ablation and the state of current knowledge in the field of high energy density physics (HEDP). Next, a summary of the work investigating the physics of ablation for materials with atomic numbers ranging from 3.5 to 22 and radiation temperatures up to 400 eV is given. Over six hundred HYADES simulations were run to find how the ablation pressure scales with increasing intensity X-ray drive and time. The transition point from subsonic to transonic behaviour is found for each material. Evidence is given for an atomic shell effect in the ablation of titanium. Finally, some comparisons are made to experimental ablation rate studies.

4.1 Introduction

The interaction of high intensity, soft X-rays with matter is of great importance in the field of HEDP. Examples include but are not limited to: opacities and equations of state of stellar interiors^{78,79}, shock driven turbulent dynamics of supernovae and gas nebulae^{80,81} and the formation of ionisation waves from newly formed stars^{82,83}. A review of modern laboratory

astrophysics can be found in reference 84. In recent decades, with the emergence of large scale experimental HEDP facilities, there has been a surge in the pursuit of laboratory astrophysics experiments. The physics of ablation under soft X-ray irradiation is also of key importance in the area of indirect drive ICF.

Materials under X-ray drive will exhibit a range of phenomena depending on the intensity and spectral structure of the source, and the composition of the target. Some of these phenomena were introduced in section 2.5.1 of chapter 2. In general, a radiative heat wave with a sharp front will penetrate into the target. In the case of a low-Z material the ablative blow-off will be transparent to the incoming X-rays and the radiation will freely penetrate into the unheated material (see section 2.5.3). In a high-Z material the opacity of the ablated plasma is higher and the incoming radiation will propagate diffusively into the cold regions (see section 2.5.2). The hydrodynamic response of the material then depends on whether the radiation wave is propagating sub, trans or super-sonically where the terminology refers to the speed of the radiation front relative to the speed of sound in the heated material.

Under subsonic propagation, the heat front is travelling into the material at less than the speed of sound. This gives rise to a gross hydrodynamic response and the formation of a shock front which is then supported by the radiation wave. The result is an ablation wave in which material is ejected from the ablation front and, through momentum conservation, sends a compression wave forwards. If the incoming radiation is sufficiently intense, the radiation wave will propagate supersonically. In supersonic propagation the heating wave moves so rapidly that very little hydrodynamic motion occurs. Transonic behaviour occurs between the sub and supersonic regimes where the heat front and shock front overlap with one another.

For the purposes of ICF capsule compression, subsonic ablation is the desired regime. Ablators should be chosen such that they ablate subsonically over the full range of hohlraum temperatures. In section 2.5.3 the temperature at which transonic behaviour will begin to occur was estimated by the relation

$$T_{\text{crit}} = \left(\frac{4\rho_0}{\sigma} \right)^{2/5} \left(\frac{R}{\mu} \right)^{3/5} . \quad (4.1)$$

Materials with a higher atomic number will transition from subsonic ablation at higher radiation temperatures. However, there is an upper limit on the atomic number as materials with high atomic numbers exhibit poor ablation efficiency. This is made apparent by inspecting the ideal rocket equation⁸⁵

$$V_{\text{shell}} = \frac{p_a}{\dot{m}_a} \ln\left(\frac{m_0}{m_f}\right) \equiv V_{\text{exhaust}} \ln\left(\frac{m_0}{m_f}\right), \quad (4.2)$$

where m_0 is the initial shell mass, m_f is the final shell mass, p_a is the ablation pressure, \dot{m}_a is the mass ablation rate per unit area V_{shell} is the shell velocity and V_{exhaust} is the velocity of the ablative blow-off. In the central hot-spot ignition scheme the shell must be accelerated to a threshold velocity in order to sufficiently heat the hotspot in the stagnation phase^{86,87}. Equation 4.2 shows that a higher exhaust velocity will result in a larger shell velocity. The lower the ion mass, the higher the exhaust velocity will be for a given temperature. This feature, in addition to the low albedo of low- Z materials, is why modern capsule designs have favoured them as ablators.

The most recent experiments on the NIF have employed three ablators⁸⁸: Germanium or silicon doped plastic (CH)⁸⁹, diamond-like high density carbon (HDC)^{90,91} and beryllium^{92,93}. Each ablator choice has its own strengths and weaknesses. The beryllium ablator is the highest performer in terms of ablation pressure and mass ablation rate which, in theory, should also make it the most hydrodynamically stable⁹³. By contrast the CH ablator is less efficient but has a much higher surface smoothness which prevents the seeding of hydrodynamic instabilities due to capsule roughness⁸⁹. The plastic ablator was the original choice for the National Ignition Campaign⁹. HDC ablators lie between CH and beryllium in terms of ablator efficiency. Due to the high density of the carbon ablators, the pulse durations are much shorter (5 ns-9 ns)⁹¹. The shorter pulse durations lead to less hohlraum wall expansion which allows for lower density gas-fills, so called near-vacuum hohlraums. Near-vacuum hohlraums experience less laser-plasma interactions leading to more efficient hohlraums⁹⁴. Recent experiments using HDC ablators and near-vacuum hohlraums hold the current record for fusion yield on the NIF¹⁰.

The significant interest in ICF research in the field of HEDP has inevitably led to the ma-

majority of work on non-astrophysical soft X-ray ablation physics concentrating on ICF ablator materials. Conversely, the astrophysical studies have been more concerned with astrophysical materials (hydrogen). Therefore, there exists very little literature on the ablation physics for mid-Z materials. This study aims to address this by investigating the underlying physics of ablation in a more general way. In this work the scalings of ablation pressure for a range of materials are compared over the temperature range 100 eV-400 eV. For each material the $T_{R,\text{critical}}$ value for transonic behaviour is determined along with power laws for the pressure scaling with temperature and time. Evidence of an atomic shell effect in the scaling of ablation pressure in titanium is also presented.

4.2 Simulation Set-up

The simulations were run in HYADES using 1D planar surfaces. A description of HYADES and the physics models used was given in chapter 3. Thermal transport was handled with a flux-limited Spitzer-Härm model. The ionisation was handled with a Saha model. The radiation transport used a multi-group diffusion model, 50 groups with upper bounds ranging from 0.003keV to 15 keV. Each target was 1 mm thick with 120 mesh lines and a feather ratio of 0.909 (meaning the spacing between each mesh line decreased by a factor of $\times 0.909$ with each zone). For each material, the drive sources ranged from 100 eV to 400 eV in steps of 10 eV. Each simulation was run for 2 ns and the maximum pressure was taken to be peak pressure achieved in any mesh region at any point in time. Simulations were performed for the following materials (and SESAME EOS numbers): Solid DT (#5271), polystyrene plastic (#7592), beryllium (#2020), carbon (#7832), high density carbon (#7830), aluminium (#3718) and titanium. There is no SESAME entry for titanium, instead a quotidian equation of state is employed⁹⁵. The corresponding densities were 0.2205 g cm^{-3} , 1.044 g cm^{-3} , 1.845 g cm^{-3} , 2.25 g cm^{-3} , 3.5 g cm^{-3} , 2.7 g cm^{-3} and 4.54 g cm^{-3} . All these materials were well represented by their EOS with the exception of HDC. In the HDC simulations the low-density, high temperature region at the boundary left the range of validity of the SESAME table. This was handled by setting the pressure and internal energies to the value at the edge of the range of validity. This region is far from the ablation front so will not significantly

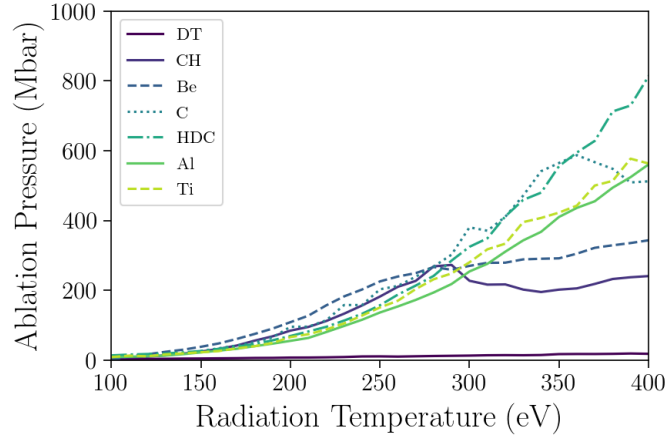


Figure 4.1: A graph that shows the results of a number of HYADES simulations of X-ray drive incident on the materials: solid DT, plastic, beryllium, carbon, high density carbon, aluminium and titanium. The X-ray drive ranges from radiation temperatures of 100 eV-400 eV in steps of 10 eV. The drive temperature is plotted against the maximum ablation pressure produced at any time in the simulation. Some of these results are re-plotted individually in figure 4.3.

affect the ablation pressure.

In total, six hundred and eighty four individual simulations were run in this study.

4.3 Simulation Results

Figure 4.1 shows how the maximum ablation pressure scaled with drive temperature for all the materials. Immediately, it can be seen that the pressure produced in the DT is much lower than any of the ablator materials. This clearly demonstrates the need for ablator materials in indirect drive ICF. One must use an ablator to even be able to reach moderate pressures.

The simulation results can be used to find the $T_{R,critical}$ value for each material. This was done by fitting a power law of the form $p_a = AT_R^\alpha$ to the results, where A and α are the fitting variables. A number of non-linear regression fits were carried out over different ranges of temperature values. Then, the best fit was chosen by visual inspection. An example of different fits are shown in figure 4.2. After a fit was chosen the $T_{R,critical}$ temperature was taken to be the last point in the fitted range. For beryllium, the value of $T_{R,critical}$ was 260 eV. The same process was then carried out for each of the materials the resulting fits are shown in figure 4.3.

The $T_{R,critical}$ value deduced from the simulations for each material is compared the the

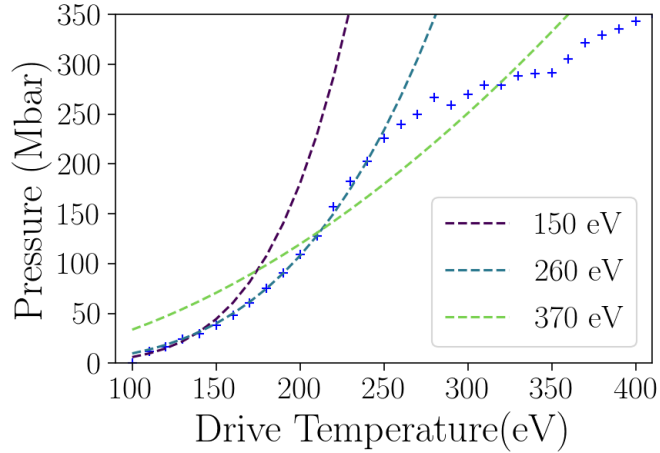


Figure 4.2: A graph showing a number of fits for the ablation pressure scaling of X-ray drive on beryllium. Each + represents the result of one simulation in HYADES. The three fits shown were applied over the ranges 100 eV-150 eV, 100 eV-260 eV and 100 eV-370 eV. The fit up to 260 eV displays the best fit before the drop off in pressure and therefore 260 eV is defined as the $T_{R,critical}$.

values predicted by equation 4.1 in figure 4.4. In each case, the simulated results predict lower $T_{R,critical}$ values than the analytical theory. This is primarily due to the assumption of ideal gas equation of state in the derivation of equation 4.1. By contrast, the simulations used accurate EOS look-up tables so a discrepancy is to be expected. However, in the case of the titanium simulation, the discrepancy between simulation and theory is noticeably larger. In addition, the fall off in pressure scaling is less pronounced than for the other materials. One can inspect whether this is actually the transition to transonic behaviour by investigating the dynamics of the ablation.

The density, pressure and radiation temperature profiles from the 400 eV titanium simulation are shown in figure 4.5. Even at 400 eV the ablation still seems to be occurring subsonically. This suggests that the change in pressure at 330 eV is not actually the transonic point. It would be useful to simulate higher drive temperatures to see at what point the ablation of titanium begins to exhibit supersonic behaviour. However, this would be outside of the range of hohlraum temperatures that are conceivable at current facilities. Alternatively, it is possible to study the materials at a fraction of the solid density. Experimentally this can be achieved by using low-density titanium foams. The density term in 4.1 shows that $T_{R,critical}$ should decrease along with the density. So the use of a titanium foam will reduce the $T_{R,critical}$ into the temperature range being explored here.

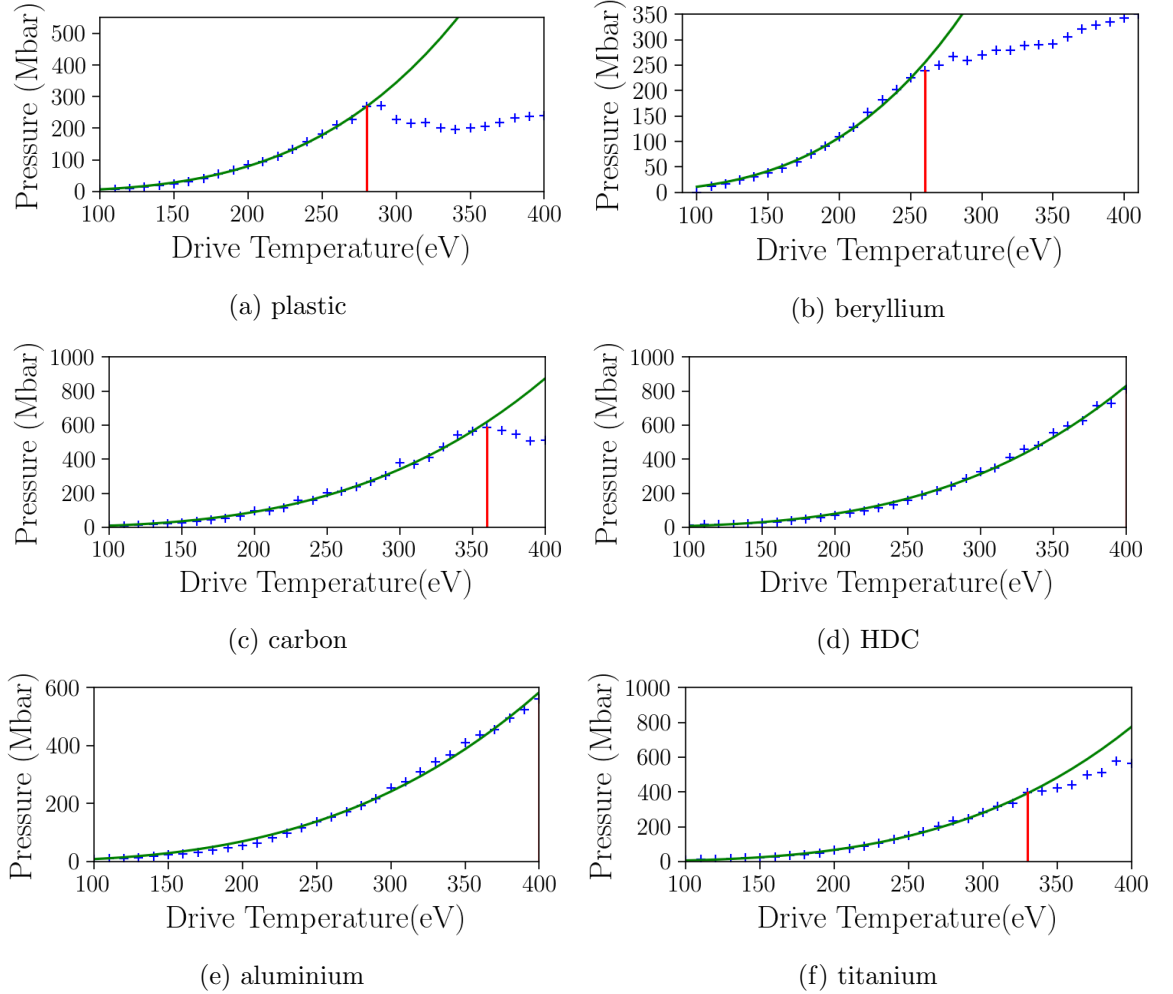


Figure 4.3: A number of graphs that show the values of $T_{R,critical}$ for each material. Each + marks the ablation temperature achieved in a HYADES simulation for the given drive temperature. The green lines represent the fitting of a scaling law of the form $p_a = AT_R^{\alpha}$. The solid red line represents the $T_{R,critical}$ value up to which the fitting is applied.

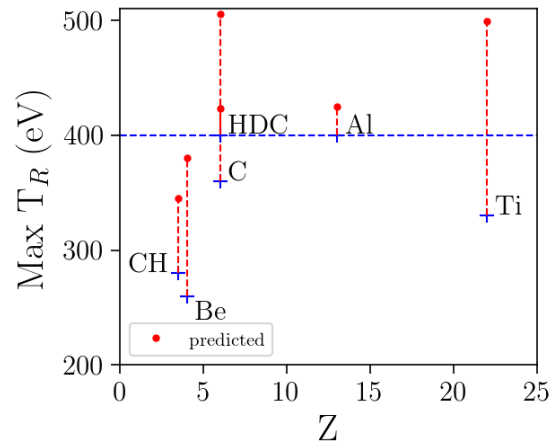


Figure 4.4: A plot that shows the $T_{R,critical}$ values for seven different materials. For each material the $T_{R,critical}$ value defined in figure 4.3 is shown as a blue +. The $T_{R,critical}$ value predicted from equation 4.1 is shown as a red dot. The blue dotted line marks the maximum 400 eV limit in the simulations.

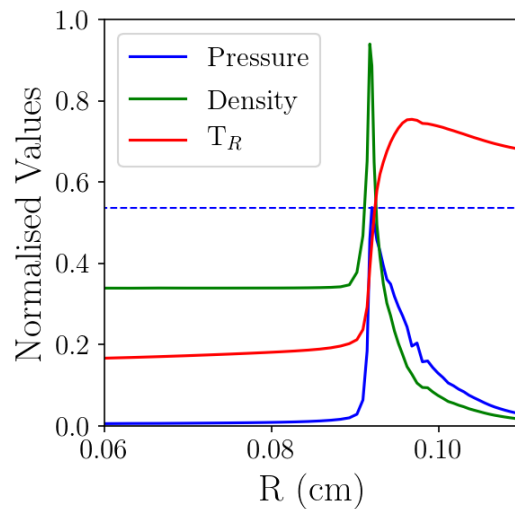


Figure 4.5: A plot of the ablation front of the 400 eV simulation of solid-density titanium. The plot shows the profile of the mass density, pressure and radiation temperature through the target, the X-ray drive is incident from the RHS. The radiation front is trailing behind the density front demonstrating subsonic ablation. The values are normalised to the maximum corresponding value at any point in the simulation.

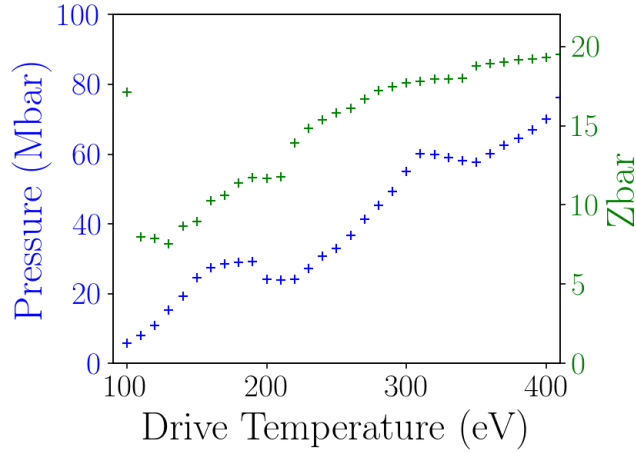


Figure 4.6: A plot of the HYADES simulations of X-ray drive on titanium at one tenth solid density. For each simulation the ablation pressure (blue +) and average ionisation at the ablation front (green +) is shown. There are two points where the pressure scaling changes, 160 eV and 310 eV.

4.4 Low-Density Titanium Simulations

Another set of X-ray drive simulations were run for titanium at one tenth solid density ($\rho = 0.454 \text{ g cm}^{-3}$). The simulations used the same models and 1 mm thick target and mesh that were described in section 4.2. The resulting ablation pressures are shown in figure 4.6. The results for low-density titanium show two points at which the pressure scaling changes. The first at 160 eV and the second at 310 eV. To find which of these points corresponds to the transition from subsonic behaviour, we can look at the dynamics at the ablation front. Figure 4.7 shows three snapshots of the density, pressure and radiation temperature profiles at temperatures around the 160 eV pressure scaling change. Figure 4.7a clearly shows a subsonic ablation regime with a peaked pressure profile leading the radiation wave. Figure 4.7b then shows that, at a higher drive temperature, the density of the shock front is beginning to weaken and widen. Finally in figure 4.7c, at a drive temperature of 200 eV, the radiation wave has begun to overtake the shock front and the density perturbation is small; the system is approaching supersonic behaviour. This confirms that the first pressure drop at 160 eV is the $T_{R,\text{critical}}$ point.

An explanation for the pressure drop seen at 310 eV is still required. Titanium has a higher atomic number and a more complex atomic structure than the low-Z ablaters. At the temperatures present in this study a titanium plasma is only partially ionised. The electrons bound in a partially ionised titanium atom will lie in a number of different atomic shells.

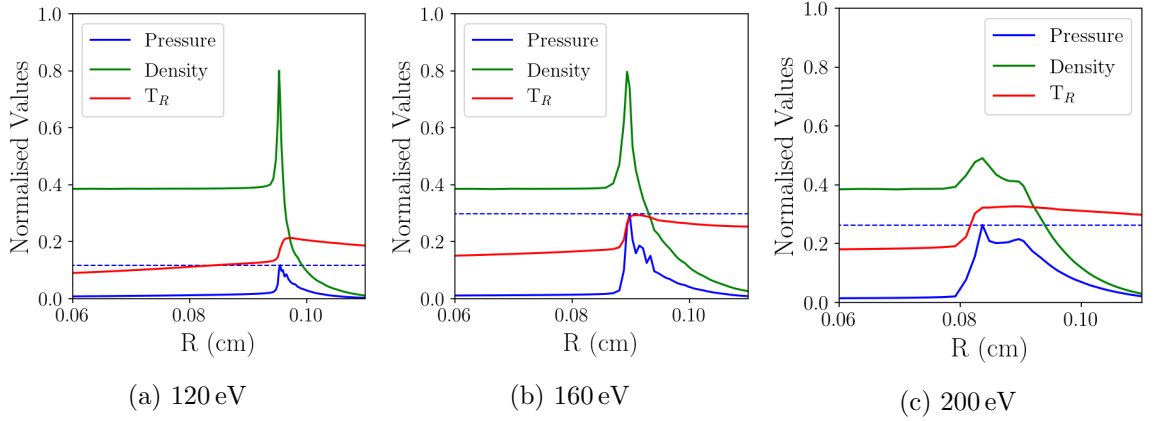


Figure 4.7: Snapshots of the density, pressure and radiation temperature profiles in low-density titanium for three different drive temperatures. Each snapshot was taken from the time in the simulation where the ablation pressure peaked. 120 eV shows a clear case of subsonic ablation. At 160 eV the density spike has begun to widen and the radiation wave begins to overtake it. Finally 200 eV shows a trend towards supersonic behaviour where the hydrodynamic perturbation is minimal.

Once the final electron in an atomic shell is removed there is a jump in the energy required to ionise the next electron as it experiences less shielding from the atomic nucleus. If there is a significant population of ions with full outer shells in the plasma, the energy required to induce further ionisations will increase. It is proposed that this is the effect causing the observed drop in pressure.

The atomic shell structure in titanium is $1s^2 2s^2 2p^6 3s^2 3p^6 3d^2 4s^2$. The titanium outer shell will be full at ionisation states +2, +12 and +20. From +19 to +20 the ionisation energy jumps significantly from 1425 eV to 6249 eV⁹⁶. In figure 4.6 the average ionisation level at the ablation front is shown. This value is taken from the same mesh region that the peak pressure was taken from. A jump in average ionisation level from 18.0 to 18.8 can be seen at 340 eV. This could correspond to a significant portion of the titanium ions jumping from the +19 to the +20 ionisation state. This jump in average ionisation state occurs at drive temperatures just above the 310 eV point where the pressure starts falling off. At temperatures just below 340 eV, the average ionisation energy has significantly increased causing the observed fall off in pressure.

The presence of a shell effect can be confirmed by using an ionisation model that should be unable to resolve such a feature. The Thomas-Fermi ionisation model uses Fermi-Dirac statistics rather than the Boltzmann statistics used in the Saha ionisation model. The Thomas-Fermi model becomes relevant for very high density plasmas, where electron degen-

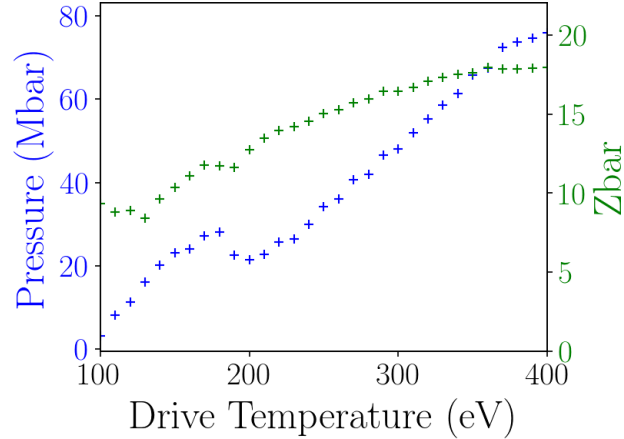


Figure 4.8: A plot of the HYADES simulations of X-ray drive on titanium at solid density. The simulations employed a Thomas-Fermi ionisation model instead of a Saha model. For each simulation the ablation pressure (blue +) and average ionisation at the ablation front (green +) is shown.

eracy effects are significant. Such a model would not be accurate in these simulations but would still be useful as one of its failings is that it is unable to resolve the shell structure of the atom³⁰. Simulations using Thomas-Fermi ionisation should still be able to observe a transition from subsonic behaviour as this a result of the radiation front reaching a speed above that of the isothermal sound speed. So, when using the Thomas-Fermi model, one should still see the first drop in pressure due to transonic behaviour but no second drop in pressure due to the atomic shell effect. To investigate this, the low-density titanium simulations were repeated with the ionisation model changed to Thomas-Fermi. The resulting ablation pressure and average ionisation values at the ablation front are shown in figure 4.8. The subsonic transition point can be seen at 150 eV, which is very close to the value of 160 eV observed using the Saha ionisation model. As expected, the second drop in pressure is no longer observed. This is strong evidence that the second drop in pressure seen when using a Saha ionisation model is the result of an atomic shell effect.

The shell effect may also explain the slight fall off in scaling seen in the original solid-density titanium simulations from section 4.3. It was confirmed earlier that this was not due to transonic behaviour. The pressure scaling and the average ionisations at the ablation front from those simulations are shown in figure 4.9. The fall off in pressure scaling begins at around 330 eV. At this point the average ionisation is starting to get close to the +12 full outer shell ionisation state. From the +11 to +12 ionisation states the ionisation energy

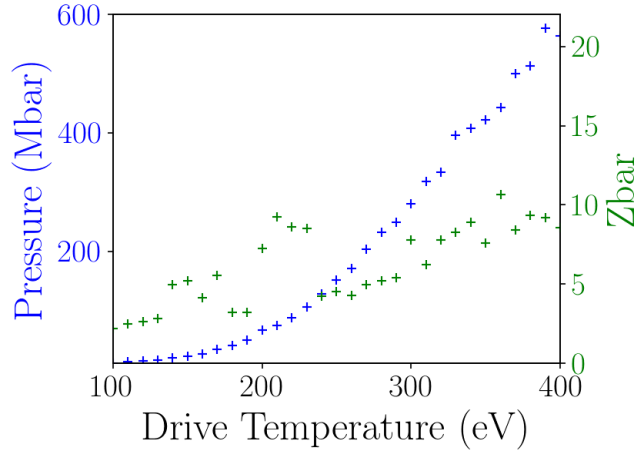


Figure 4.9: A plot of the HYADES simulations of X-ray drive on titanium at solid density that was previously shown in section 4.3. The ablation pressure is plotted in blue and the ionisation at the ablation front is plotted in green. At 330 eV a fall off in pressure is seen that could be explained by an atomic shell effect at the +12 ionisation state

jumps from 292 eV to 788 eV⁹⁶. This energy jump is much less than the jump at the +20 ionisation state which explains why the fall off in pressure is weaker.

The shell effect is likely not seen in the other plasmas because their atomic numbers and ionisation energies are lower. However, it is worth noting that these effects are likely present in other high-Z materials which have complex shell structures and in which the jumps in ionisation energy can be quite large. Observing these effects though, would most likely require highly ionised plasmas driven at X-ray radiation temperatures above 400 eV. As this is above what is achievable in current hohlraums, this is not investigated any further and left as a point of further study.

4.5 Temperature and Time Scaling

In addition to the scaling of maximum ablation pressure with temperature, the pressure scaling with time was also investigated. These simulations used a constant drive source with radiation temperature 250 eV. The settings were the same as with the varying temperature simulations other than that the simulation end time was 10 ns instead of 2 ns. Again, the ablation pressure was taken to be the maximum pressure in any mesh region. Then, as with the temperature scaling, a power law of the form $p = Bt^\beta$ was fit with regression fitting. The resulting fit for each material is shown in figure 4.10. In each case the first 1 ns was

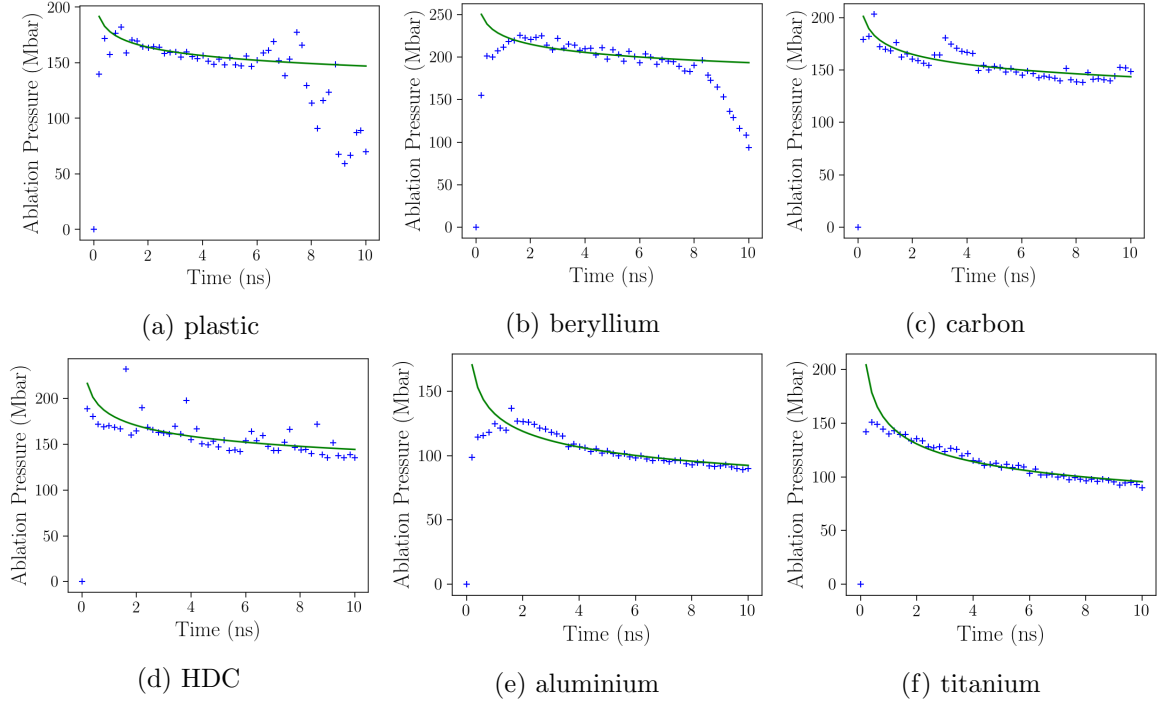


Figure 4.10: A number of plots showing how the ablation pressure in 6 materials being driven with a 250 eV X-ray source changes over time. In each plot the ablation pressures are shown as blue crosses and a fitting of a power law of the form $p = Bt^\beta$ is shown as a green line.

Material	Suggested Scaling Law	Max T_R
Plastic	$p_a \propto T_R^{3.6} t^{-0.07}$	280 eV
Beryllium	$p_a \propto T_R^{3.3} t^{-0.07}$	260 eV
Carbon	$p_a \propto T_R^{3.3} t^{-0.09}$	360 eV
HDC	$p_a \propto T_R^{3.4} t^{-0.10}$	>400 eV
Aluminium	$p_a \propto T_R^{3.2} t^{-0.17}$	>400 eV
Titanium	$p_a \propto T_R^{3.2} t^{-0.21}$	>400 eV

Table 4.1: A table summarising the pressure scaling with temperature and time for six materials. The temperature fits are shown in figure 4.3 and the time fits shown in figure 4.10. Shown as well are the $T_{R,critical}$ values defined in figure 4.3. Note that the $T_{R,critical}$ value for titanium has been changed to >400 eV based on the discussion of the atomic shell effect in section 4.4.

omitted from the fit as it typically takes a short amount of time for the pressure to build up. In the plastic and beryllium simulations, drops in pressure can be seen when the shock in the target breaks out of the rear surface at 6 ns and 8 ns respectively. The data range was accordingly reduced to avoid fitting in those regions. The power scalings with temperature and time are summarised in table 4.1. The higher-Z materials have weaker scaling in both temperature and time but the $T_{R,critical}$ is higher. These results are in-line with the discussion of the theory which suggests that low-Z materials are better ablaters but are limited in the pressure they can achieve due to early transitions to transonic behaviour.

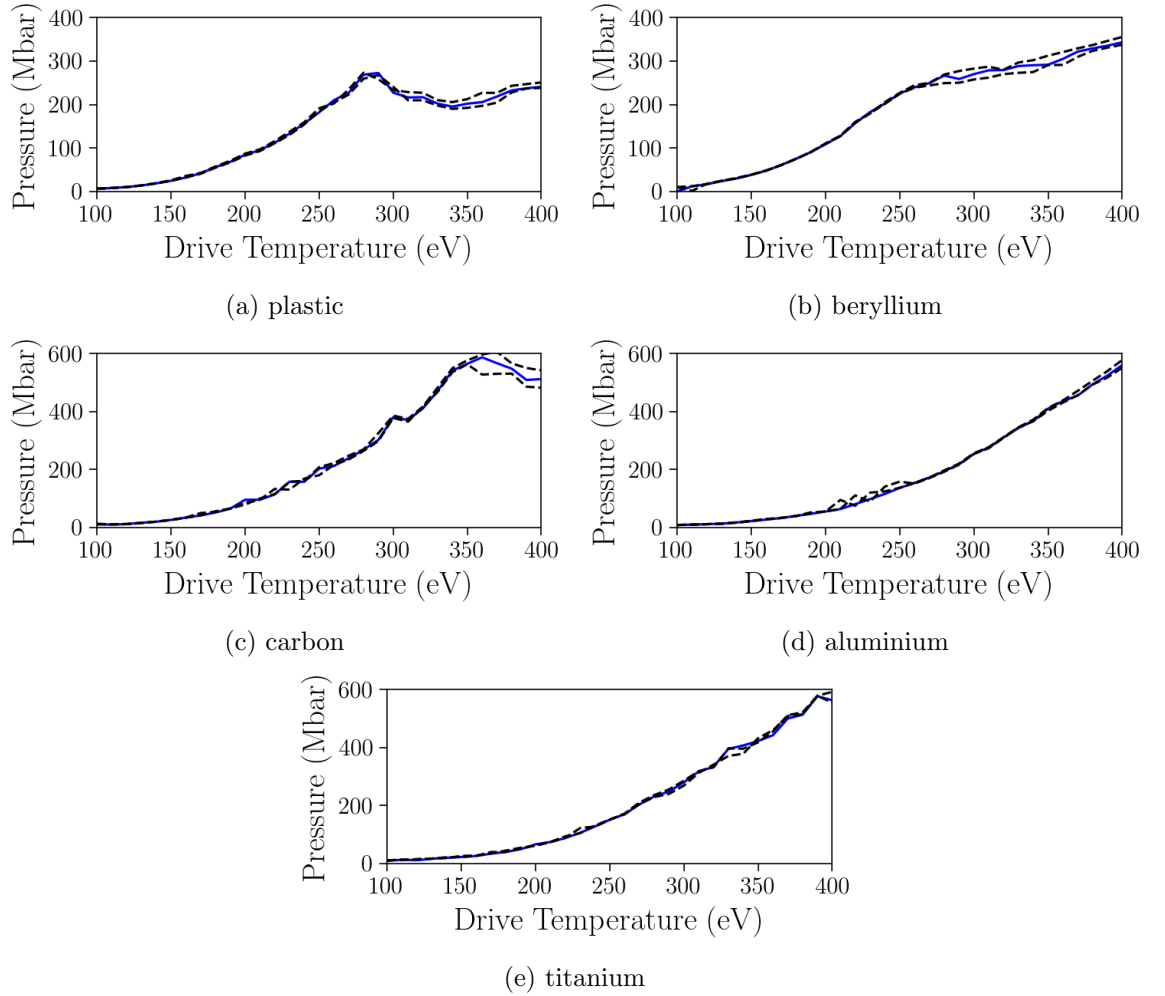


Figure 4.11: Plots of the ablation pressure scaling simulations that were repeated with varying opacity. The original results with unmodified opacity are shown as solid blue lines. The $0.5\times$ and $2\times$ opacity results are shown as black dashed lines.

4.6 Opacity effects

The opacity model in HYADES is not expected to be particularly accurate for higher- Z materials. With that in mind it is interesting to consider the sensitivity of the ablation pressure to the opacity. HYADES allows for the opacity to be modified using a number of user defined multiplier variables that appear in the radiation transport equations. The simulations described in section 4.3 were re-run for the materials plastic, beryllium, carbon, aluminium and titanium with $0.5\times$ and $2\times$ opacity. The results are shown in figure 4.11.

The change in opacity does not make a significant difference in pressure, especially at temperatures below $T_{R,critical}$. However, there is a noticeable difference in the pressure at tempera-

tures above $T_{R,\text{critical}}$. Interestingly there is no change in the $T_{R,\text{critical}}$ value. This suggests that the subsonic pressure scaling and the transition to supersonic behaviour is primarily a function of the equation of state of the material.

4.7 Comparison to Experiment

In this final section, an effort is made to compare the scalings arrived at in this work to experimental measurements. In general there does not exist a wide range of literature on the scaling of ablation pressure in materials under X-ray irradiation. The studies that have been carried out have focussed on the low-Z indirect drive ICF ablator materials. In reference 97 the X-ray ablation rates of plastic, beryllium and HDC were measured over the radiation temperature range of 160 eV-240 eV. A similar study measured the ablation rate of aluminium over the drive temperature range 180 – 250 eV⁹⁸. It is not possible to directly measure ablation pressure but one can infer it from the rate of ablated mass per unit area \dot{m}_a/A_s and the sound speed c_s by the simple relation⁹⁷

$$p_a = \frac{\dot{m}_a c_s}{A_s}. \quad (4.3)$$

The sound speed for a fully ionised plasma using an ideal gas equation of state is then expressed by³³.

$$c_s = \left(\frac{\gamma(1+Z)k_B T_R}{A m_p} \right)^{1/2}. \quad (4.4)$$

Equations 4.3 and 4.4 can then be used to infer the ablation pressures from the experimentally measured ablation rates. The scaling laws arrived at in section 4.5 are compared to the inferred ablation pressures in figure 4.12. The scalings seem to match fairly well for aluminium and beryllium. Although as these pressures have been inferred from the assumption of full ionisation (which is not valid in these temperature ranges) an exact match should not be expected.

In the plastic simulations there is a significant over-prediction compared to the experimental measurements. This is explained by the use of a germanium dopant in the experimental study⁹⁷. The presence of a high-Z dopant will reduce the achievable pressure in the material

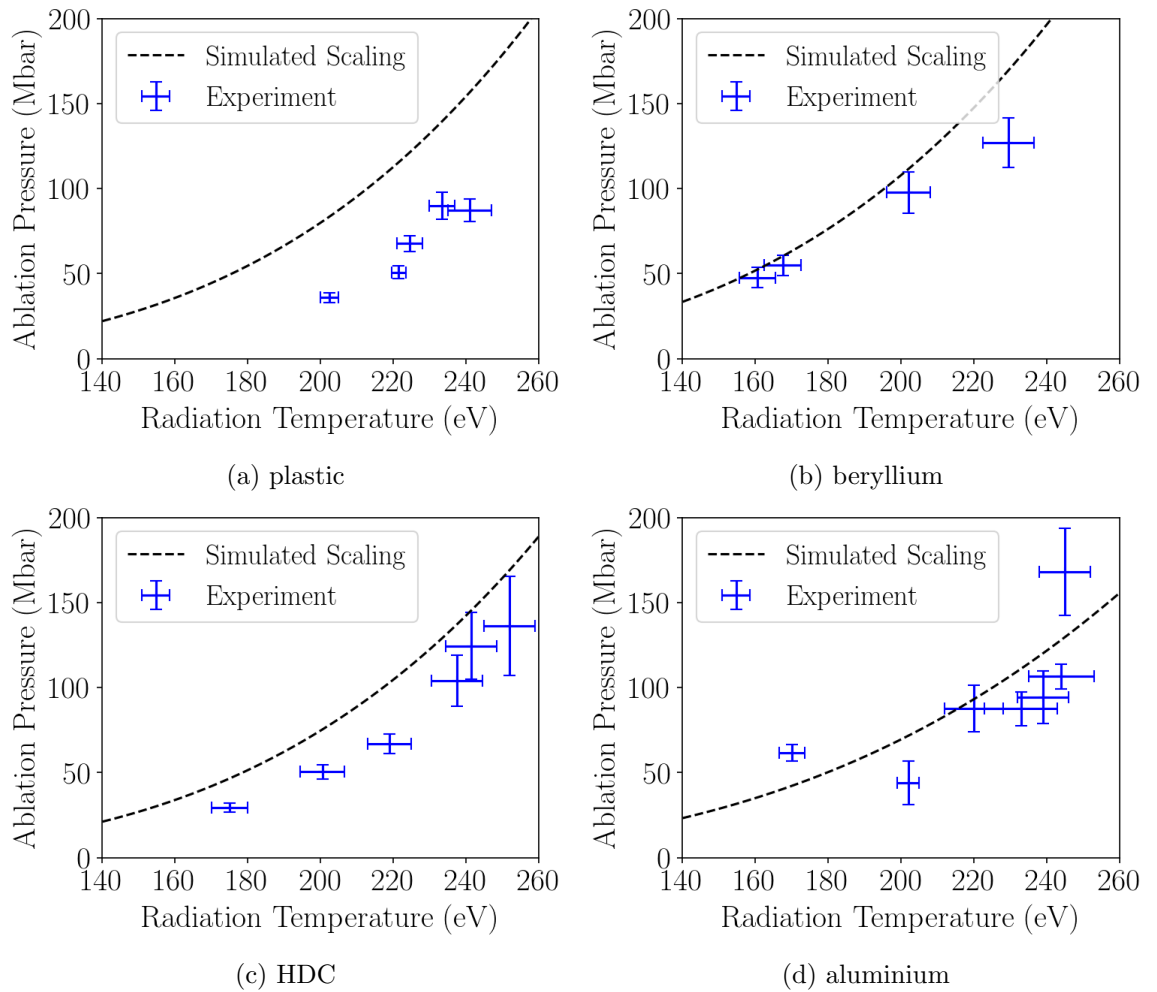


Figure 4.12: Plots that compare the fitted pressure scaling laws from figure 4.3 with ablation pressures inferred from experimental measurements from references 97 and 98 (extracted using WebPlotDigitizer⁹⁹). In each plot the scaling laws from the HYADES simulations are shown as black dashed lines and the experimental results are shown as blue error bars.

(according to equations 4.3 and 4.4). This is why the dopant in capsule ablators is concentrated in layers near the inner surface of the shell⁸⁹. For the HDC material, the predicted ablation pressures are slightly above the measured pressures, although the shape of the trend is similar. There is also a fall off in the experimental pressure at ~ 230 eV in beryllium. It is possible that this is due to random variation in the measurements as the scaling law still lies within 2σ of the measurement. However, it could be a sign of the transition to transonic behaviour. The simulations predicted that this would occur at 260 eV but it is possible that experiment observes this occurring at lower temperatures. Further measurements of the ablation of beryllium would be required to confirm this.

Chapter 5

Producing Shock-Ignition-like Pressures Using Indirect Drive

This chapter outlines work that investigated the laser drive parameters that would be required for an indirect-drive shock-ignition scheme. First, a description is given of the potential benefits of carrying out indirect-drive shock-ignition experiments. Then, a number of 1D HYADES simulations are summarised investigating the X-ray drive parameters needed to create a shock-ignition-like pressures. Following this, 2D simulations of hohlraums were carried out to find the laser powers that would be required to generate the required radiation temperatures.

5.1 Introduction

Shock ignition has several benefits over the traditional central hotspot ignition scheme. Firstly, the use of a slow implosion velocity ($<300 \text{ km s}^{-1}$) makes the implosion more robust to hydrodynamic instabilities and gives more time for the assembly of fuel, leading to higher yields⁵⁸. Secondly, the laser-plasma interactions at the intensities required ($10^{15} - 10^{16} \text{ W cm}^{-2}$) are achievable on existing facilities⁵⁹. Finally, from an inertial fusion energy perspective, it has been shown that the isochoric assembly of the fuel may potentially lead to drive pulses with a lower total energy than in CHS ignition⁵⁷. This gives the potential for higher gains, which is why it is sometimes referred to as a high-gain scheme.

Historically, shock ignition has only been considered from a direct drive perspective^{23,58}. However, to date, there exist no direct drive platforms configured to perform full scale ignition experiments. There have been numerous studies on shock ignition on smaller facilities but it is challenging to achieve shock-ignition-relevant plasma temperatures and length scales with such lasers. There has been some success in terms of the demonstration of shock-ignition-scale pressures^{66–68}. However, it is difficult to replicate the parametric instabilities that would be present. Smaller facilities tend to be TPD dominated whereas ignition-scale experiments would experience higher levels of SRS¹⁰⁰. It is important to understand these instabilities as they create populations of hot electrons which may be capable of penetrating through the dense fuel and causing preheat. Whether these electrons will deposit their energy before or after the shock front is still not known and has major implications for the viability of shock ignition^{59,69,101}.

To adequately assess the feasibility of shock ignition, a platform must be developed for large scale facilities. The three most energetic laser facilities that would be capable of conducting these experiments NIF, LMJ and SG-III, are set-up in a polar drive configuration. The polar drive configuration is necessary for indirect drive experiments so that the hohlraum can be uniformly irradiated. Polar direct drive set-ups have been proposed on the NIF¹⁰² and LMJ^{103,104} via a re-pointing of the beams. This would be costly to implement but achievable. However, there is still some concern as to whether sufficiently uniform drive symmetry would be possible. Low-mode drive asymmetry was highlighted as one of the biggest barriers to ignition during the National Ignition Campaign⁹. Consequentially, the ability to carry out shock ignition experiments in an indirect drive configuration would be desirable. However, there exist some potential obstacles to the development of an indirect-drive shock-ignition scheme.

The crucial stage in the drive pulse of shock ignition is the sharp rise in drive power (ignition spike) used to launch the ignition shock. This ignition spike must be capable of launching a shock on the magnitude of a couple hundred Mbar. When using direct drive, increasing the drive power rapidly is trivial but it is somewhat more complicated in the case of indirect drive. The X-rays are created as a result of the heating of the hohlraum wall. The heat capacity of the wall causes an inherent lag in the X-ray production^{23,105}. This causes a delay in

the X-ray profile relative to the laser drive profile on the order of about half a nanosecond¹⁰⁵. The time lag may make it difficult to create the necessary sharp rise in X-ray flux that would be required to launch the ignition shock. It is possible to somewhat mitigate this by pushing to higher laser drive powers and heating the hohlraum faster. However, using higher driver powers at late stages in the implosion can give rise to high levels of parametric instabilities due to the large amount of plasma fill in the hohlraums. These instabilities deplete energy from the beam, preventing it from being absorbed in the wall. They can also be a source of suprathermal electrons, which can cause fuel pre-heat. It is for these reasons that there is scepticism around the utility of an indirect drive configuration for the purpose of conducting shock ignition experiments. Despite those reservations, an indirect-drive shock-ignition platform would be of great use in developing the understanding of the implosion dynamics of shock ignition at ignition relevant parameters. This is the motivation for the work outlined in this chapter.

This work was built on an established direct-drive shock-ignition profile developed in reference 62. The laser drive profile was scaled to a pressure using a steady state ablation scaling law. From there the pressure profile could then be scaled to a soft X-ray drive profile. These results were then confirmed through 1D radiation hydrodynamics simulations. The resultant X-ray flux profile was taken to be a shock-ignition-like drive source. Then, 2D simulations of laser irradiated hohlraums were run to find a laser source that could generate the shock ignition X-ray profile. A few different scaling laws are used to verify the results. A comparison is then given to experimental results as well as other, similar numerical studies.

5.2 1D Ablation Pressure Scaling Simulations

5.2.1 Direct-Drive Shock-Ignition Profile

This study began by searching for a direct-drive shock-ignition profile that has already been demonstrated to work. Designing an integrated indirect-drive shock-ignition target from scratch would be an involved project and beyond the aims of the current work. Using an already established shock ignition profile will give a good representation of the ranges of pressures required and the shape of the pressure profile in time. A study of a shock

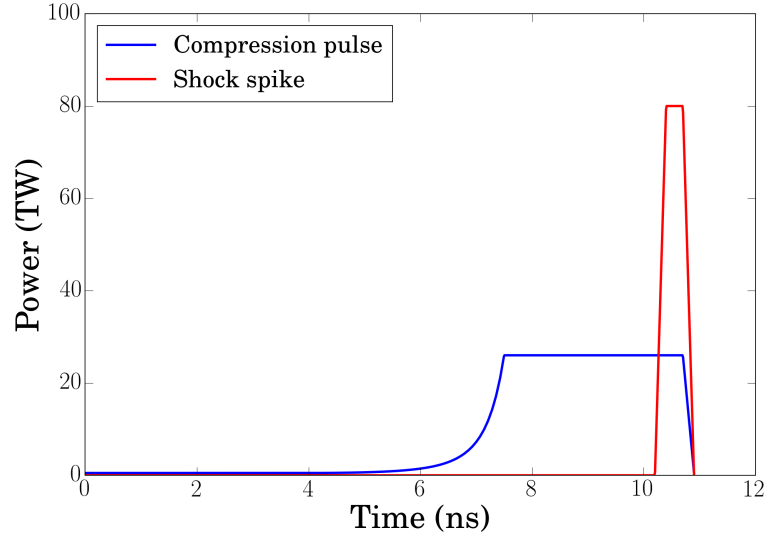


Figure 5.1: Power deposition of the drive profile that can be seen in figure 6a in reference 62. The profile is separated into two portions. The compression pulse (blue) that drives the implosion of the capsule to sufficient density and the shock spike (red) that launches a strong shock to ignite the fuel.

ignition baseline target produced for the HiPER project¹⁰⁶ was chosen due to the in-depth literature published on the capsule, drive-pulse design and simulation details^{62,63,107}. These publications were investigating the ignition of a 211 μm thickness solid DT ice ablator, 833 μm thickness DT gas, capsule via a direct drive 0.351 μm wavelength laser source. The work covers a wide range of shock ignition topics but the important information for this study is the direct-drive power-deposition profile that was used in 1D spherical implosion simulations, the full details of which are given in figure 6a in reference 62. In the 1D study, using the radiation hydrodynamics code CHIC¹⁰⁸, that profile was shown to produce a thermonuclear yield of close to 20 MJ.

As the Ribeyre drive pulse was shown to be capable of igniting a fuel capsule, it is used as the baseline for this study. The power deposition profile (that is the energy deposited into the ablator per unit time) has been reproduced in figure 5.1. The power profile is separated into two components: the compression pulse and the igniter pulse. The compression pulse is designed to compress the fuel on a low adiabat. That is to say the fuel will be compressed as close to adiabatically as possible to ensure the entropy of the fuel doesn't increase making it harder to compress. The adiabat, α is a measure of the entropy of the capsule shell and is defined as the ratio of the pressure in the shell to the Fermi-degenerate pressure of the

shell calculated at solid density. The adiabat for this compression pulse was designed to be $\alpha \approx 1$ ¹⁰⁷. To maintain adiabatic compression, a Kidder-like rise is used between 4-7.5 ns¹⁰⁹. The Kidder-like rise comes from an analytical theory of homogenous isotropic compression from a laser driver¹¹⁰. The equation for the Kidder-like rise is given by

$$P = \frac{P_0}{\left(1 - (t/T_c)^2\right)^\omega}, \quad (5.1)$$

where t is time in ns, ω governs the steepness of the pressure increase and P_0 and T_c are normalisation coefficients defined such that they match with the power profile outlined before. For the profile in the present work, a steepness value of $\omega = 7$ was used (numerical simulations have shown that a value of $2 < \omega < 7$ has little effect on the shell adiabat¹⁰⁹). The igniter spike rise begins at 10.2 ns and, at 10.4 ns, peaks at a power of 80 TW which lasts until 10.7 ns and then drops to zero at 10.9 ns.

The aim of the work described in this chapter was to find an X-ray drive profile that is capable of producing the same implosion parameters as the Ribeyre laser drive profile. To do this, a variable is required that allows for direct comparison of the two types of drive sources. In the ideal case of subsonic ablation, all the incident drive radiation is absorbed before the ablation front and then transported to the front via thermal conduction. The pressure produced at the ablation front (ablation pressure) then drives a compression wave into the fuel. For this reason, the ablation pressure makes for a good comparison point between the two drivers. In the actual case, there exist some pre-heat effects that may cause discrepancies in the two drive sources. For example in indirect-drive implosions hard X-rays are produced from M-band emission that will not be present in direct-drive implosions. However, these effects are typically neglected in radiation hydrodynamics simulations so the ablation pressure will be adequate for a simple comparison.

5.2.2 Steady State Ablation Scaling

To find an initial estimate for an X-ray drive profile, the most simple approach is to use an analytic scaling law that relates the drive energy to ablation pressure. These scaling laws are derived by considering the energy flux deposited into the material by the incoming

radiation and using the conservation of mass, momentum and energy. The deposited energy can then be converted to a pressure using an ideal gas equation of state. Ablator materials in ICF are usually low- Z ($Z \leq 6$). In this case, the ablative blow-off is transparent to the incoming radiation and it can be assumed that the radiative energy is absorbed entirely at the ablation front. Under these conditions, one can assume a case of steady state ablation. The full treatment of the physics of this scaling is outlined in section 2.5.3. The equations 2.54 and 2.56 can be used to estimate the ablation pressure for laser and X-ray drive respectively. Entering in the values of $Z = 1$, $A = 2.5$ and $\rho = 0.22 \text{ g cm}^{-3}$ for DT into equation 2.54 gives the following scaling law for laser drive on a DT surface

$$p_a = 40 \frac{I_L^{2/3}}{\lambda_L}, \quad (5.2)$$

where p_a is ablation pressure in Mbar, I_L is drive intensity in $10^{15} \text{ W cm}^{-2}$ and λ_L is wavelength in μm . The power can be converted into an intensity by dividing by the target surface area which is 0.137 cm^2 for the HiPER target capsule radius of $1044 \mu\text{m}$. Note that the assumption of constant surface area is not valid as the outer capsule surface area will decrease as capsule implodes. This is accounted for in the next section by running a 1D direct drive simulation in spherical geometry.

The ablation pressure can now be scaled to an X-ray radiation temperature profile. Firstly, in the case of X-ray drive, an ablator material is required. The need for an ablator was made clear in the soft X-ray ablation scaling study in chapter 4. Under soft X-ray radiation, DT is essentially heated volumetrically. Equation 2.53 predicts that, for DT, the transition from subsonic to transonic behaviour will occur at a temperature of 133 eV , which is far below the temperatures required here. Beryllium is a standard ablator choice in indirect drive ICF experiments^{93,98}. Equation 2.53 predicts that, for beryllium, the transition from the subsonic regime will occur at 380 eV , which is well above the radiation temperatures reached during capsule implosions at the NIF and as such makes it a suitable ablator choice for indirect-drive shock-ignition. With $Z = 4$, $A = 9$ and $\rho_0 = 1.84 \text{ g cm}^{-2}$ the pressure

scaling predicted from equation 2.56 is

$$p_a = 6.6T_r^{7/2}. \quad (5.3)$$

It is worth pointing out at this point that a beryllium coated capsule would have a heavier shell and therefore different implosion dynamics. However, the aim of this study was only to find the the drive parameters that would be required to produce the shock-ignition scale pressures. The dynamics of the implosion are not considered further here.

5.2.3 1D Ablation Pressure Simulations

This section summarises the 1D radiation hydrodynamics simulations investigating the pressure scaling for both laser and soft X-ray drive. The simulations were run using the code HYADES; chapter 3 outlines the physics models present in HYADES. Both the 1D simulations described in this chapter used the same physics models. The equation of state was calculated using SESAME look-up tables. Electron transport was handled with a flux-limited Spitzer-Härm model with a flux limiter of 0.06. The ionization model was an average-atom LTE. The average-atom LTE model was chosen over Saha as it can account for degeneracy effects that become important when the capsule is significantly compressed. Radiation transport was handled with a multi-group diffusion model. The radiation absorption coefficients are calculated in-line using the HYADES APOP (see section 3.1.7). The APOP is not expected to give particularly accurate opacity calculations for high-Z materials but should be adequate for the low-Z materials being used in these simulations. In any case, the validity of these models are tested later when comparing with experimental results.

As noted previously, in the direct drive simulations, the spherically converging outer surface must be accounted for. The need for this arises due to a ‘zooming’ effect. This is the effect that, as the capsule implodes, the laser radiation is distributed over a smaller surface area. In the 1D simulations, the laser source is defined in terms of a power deposition. Therefore, as the capsule implodes, the outer surface area over which the laser drive is deposited decreases. In this manner, the intensity of the drive increases for fixed powers. As the ablation pressure scales directly with intensity (equation 5.2), the pressure is substantially increased as the

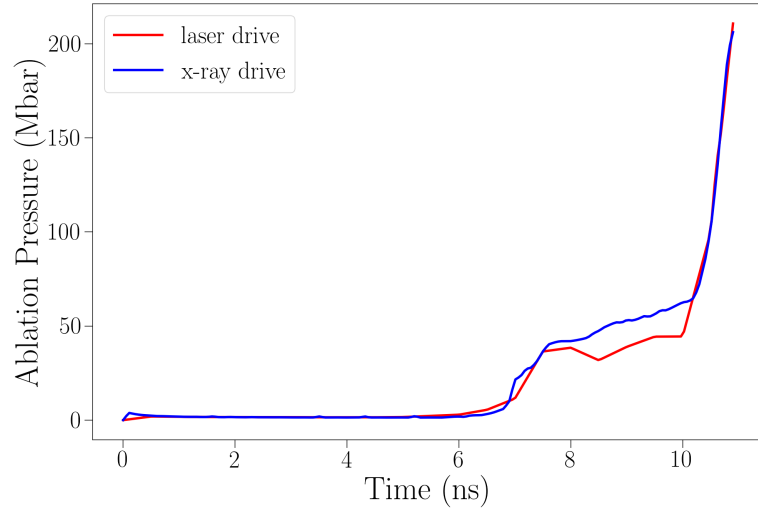


Figure 5.2: The ablation pressures produced by X-ray and laser drive in 1D HYADES simulations. The ablation pressure produced by the Ribeyre laser drive profile on the spherical HiPER baseline target is shown as a solid red line. Then, in blue, the results for the ablation pressure produced from the irradiation of a planar beryllium target under the X-ray profile that was scaled from the spherical laser drive pressure results.

capsule implodes. Some studies have suggested ways to utilise this effect by using lasers of varying focal-spot size^{111–113}. Zooming is easily accounted for in HYADES when running in spherical geometry with the source defined in terms of power. This is not necessary in the X-ray simulations as X-ray sources in HYADES are defined in units of intensity.

The spherical, laser-drive simulations were run using the same capsule design that was used in the Ribeyre study that the laser power profile was taken from. The capsule is the HiPER baseline target¹⁰⁶. This way, one should expect the same amount of spherical convergence and accurate modelling of the zooming effect. The capsule design had 833 μm of DT (SESAME #5271) gas-fill at density of 0.1 mg cm^{-3} , surrounded by 211 μm of 0.25 g cm^{-3} solid DT. The Ribeyre power deposition profile (figure 5.1) was used as the drive source with a 0.351 μm wavelength laser. A 0.351 μm wavelength laser is standard for direct drive as the third harmonic of neodymium glass laser system. The ablation pressure was taken to be the peak pressure produced in the DT. The resulting ablation pressure achieved can be seen in figure 5.2.

From here, the next step was to find an X-ray flux profile capable of achieving the same pressures. A prediction for the required radiation temperature profile can found by scaling the ablation pressure from the direct drive simulation to a radiation temperature profile us-

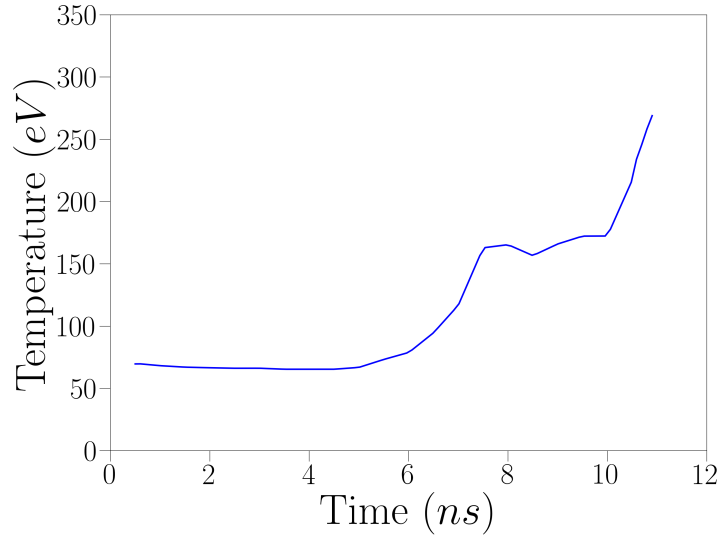


Figure 5.3: The X-ray radiation temperature profile produced from scaling of the pressure produced from the spherical compression of the HiPER target under laser drive (shown in figure 5.2) using equation 5.3.

ing equation 5.3. The resulting X-ray radiation temperature profile can be seen in figure 5.3. That radiation temperature profile was then put into a 1D planar simulation of a beryllium surface to confirm that the pressures match. The target in the simulation was a 1000 μm thick planar beryllium (SESAME #2020) surface at the solid density of 1.84 g cm^{-3} . It is reiterated here that the X-ray flux is entered into the simulation as an intensity, so there are no zooming effects to be accounted for and therefore a planar target is appropriate. The ablation pressure profile produced can be seen in figure 5.2 as the solid blue line.

Equation 5.3 has made a good prediction for the required X-ray drive intensity as is demonstrated by the match between the two pressure profiles. Crucially, the rate of rise in pressure is fast enough in the ignition spike region. It can be stated that this X-ray radiation profile is capable of producing shock-ignition-like pressures. The peak pressures achieved are just above 200 Mbar which is in the region of shock-ignition-like pressures. Now that a shock-ignition-like X-ray profile has been found, the next step in this work is to investigate the laser to X-ray conversion in hohlraums and what laser drive parameters would be required to produce it.

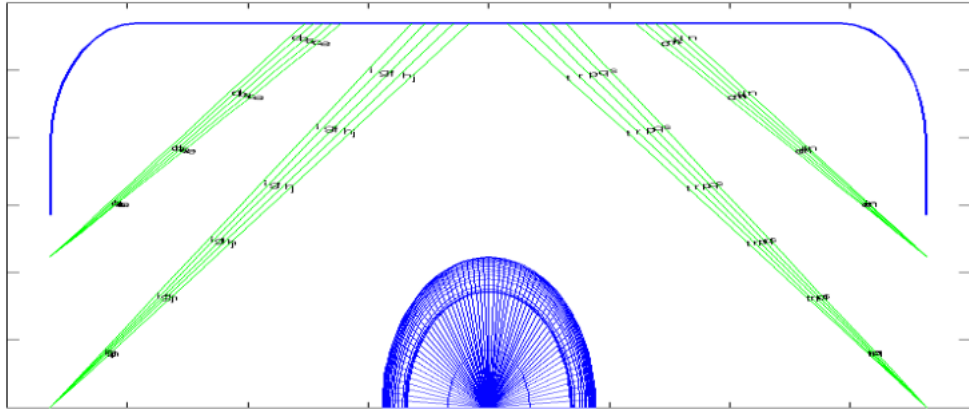


Figure 5.4: A diagram of the hohlraum used in the h2d simulations. This is a screen-shot of the mesh taken from the `hyadplot` utility of h2d. The hohlraum wall and capsule mesh are shown in blue, the ray tracing lines for the laser source are shown in green.

5.3 2D Laser to X-ray Conversion Simulations

5.3.1 Hohlraum Simulation

The hohlraum modelling was carried out using the 2D radiation hydrodynamics code h2d, a description of which is given in chapter 3. Radiation transport was modelled with multi-group model, ionisation used an average atom LTE and equation of state was handled with SESAME tables. The simulations used a NIF-scale gold (SESAME #2700), vacuum fill hohlraum with the dimensions: 8.2 mm length, 5.1 mm diameter, 10 μm thickness with laser entrance holes of 2.56 mm diameter. The laser source was 0.35 μm in wavelength and the laser absorption was handled via a ray-tracing inverse-bremsstrahlung model. A 1044 μm radius, plastic coated, DT capsule was placed in the centre of the hohlraum. The role of this capsule was simply to provide a region in which to measure the X-ray flux, the physics of the implosion was not explored. A diagram of the simulation geometry is shown in figure 5.4.

In an attempt to avoid mesh entanglement and simplify the simulations, hydrodynamics was initially turned off. However, in these simulations, the X-ray conversion was unphysically low. Laser powers in the 10s of PW were required to reach even moderate radiation temperatures. For accurate X-ray conversion modelling, an ablative heat wave needs to form at the hohlraum wall. To allow for this, hydrodynamics is turned on for the first 2 ns, which gives enough time for the ablative heat wave to form. This sets up the rising density profile into the hohlraum

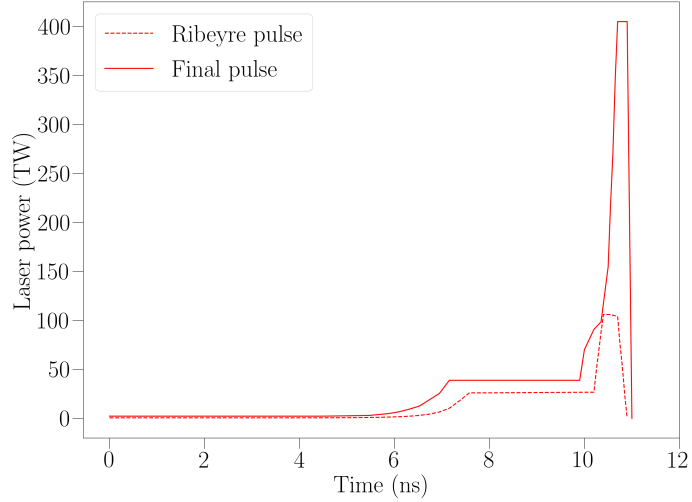


Figure 5.5: A plot that shows the differences in the Ribeyre pulse and the final shock-ignition-like drive pulse arrived at in the h2d simulations.

wall where laser light is absorbed via inverse bremsstrahlung up to the critical density. After 2 ns, the hydrodynamics is turned off. In doing this, the effects of the expansion of the gold wall are not considered. Expansion of the gold plasma into the hohlraum cavity will affect the laser plasma coupling through the presence of laser plasma instabilities that occur in low density plasma. Typically the presence of SRS and SBS reduce the laser absorption efficiency to 90%^{114,115}. HYADES at present is not able to directly account for these effects but they are discussed in more detail later. The X-ray emission from the gold wall is a function of the penetration of the radiation wave into the wall. For high-Z gold however, the energy transport of the heat wave is dominated by thermal conduction (as demonstrated by the weak scaling of ablation pressure in section 2.5.2). Thermal transport still takes place in HYADES with the hydrodynamic motion turned off. As thermal transport is the dominant process in the penetration of the heating wave, it is reasonable to assume that the laser to X-ray conversion is modelled with sufficient accuracy.

As an initial starting point, the Ribeyre profile was used to drive the hohlraum. Changes were made iteratively over a series of simulations to find a laser profile that could produce the required X-ray flux. Figure 5.5 shows the final pulse design. The final laser profile arrived at begins with a 2.5 TW foot, has a Kidder-like rise (equation 5.1) between 4 ns and 7.12 ns up to 39 TW. The ignition spike peaks at 400 TW rising between 9.9 ns and 10.7 ns, then from 10.9 ns decays linearly to zero. The total drive energy of the pulse is 290 kJ. There have

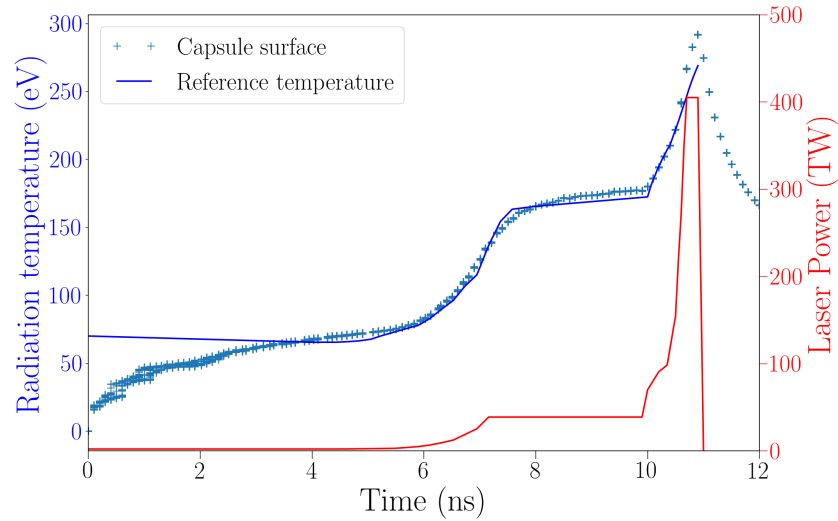


Figure 5.6: The X-ray flux profile produced from a laser drive profile (red) in a NIF-scale hohlraum. The solid blue line shows the desired profile from figure 5.3 and the radiation temperature achieved in the simulation is shown as blue crosses.

been some significant changes from the original Ribeyre profile. Most notably, the power of the drive has considerably increased. This is a result of the fact that thermal energy is stored in the hohlraum wall and the radiation field in the cavity. Essentially, the laser drive power (which in the direct drive simulations was entirely incident on the capsule surface) is now distributed over the surface of the hohlraum and capsule. This accounts for the higher power required in the compression portion of the drive pulse. Then, the peak drive power was raised significantly above that of the Ribeyre profile in an effort to drive a fast-rising hohlraum temperature at the end of the pulse. There were also a number of changes in the shape of the profile. In general, the rises in power occur at earlier times, which helps account for the time lag in the conversion to X-rays.

The hohlraum temperature profile produced by the new pulse shape can be seen in figure 5.6 compared to the X-ray profile used in the 1D simulations, which has been labelled “reference temperature”. The new laser profile produces an X-ray flux that shows good match in the Kidder-rise region and the ignition spike region. Most importantly, the rise in X-ray flux occurs at an appropriately fast rate. This is worth drawing attention to as the feasibility of this rise is the main source of scepticism towards indirect-drive shock-ignition and in these simulations it has been achieved. In addition, the peak laser power required was only 400 TW which is within the standard operating parameters of the NIF. However, there are still some

effects that would be present in experiment that aren't accounted for in these simulations. The rest of this chapter is dedicated to investigating some of those physical effects. The radiation temperature profile from figure 5.6 was used in another simulation to achieve a peak pressure of 250 Mbar.

5.3.2 Low-Density Gas-Fill and Flux Limited Electron Transport

Hohlraum experiments typically use a low-density gas-fill to counteract the plasma expansion at the hohlraum wall. Simulations were re-run with a low-density $\rho = 1 \text{ mg cm}^{-3}$ helium gas-fill but the laser to X-ray conversion was unaffected as negligible energy was deposited in the helium. However, the gas-fill may be a site for parametric instabilities that will take energy from the laser and prevent it reaching the hohlraum wall. h2d does not have the capability to model these instabilities but they are discussed in more detail later.

The original simulations were run with a Spitzer-Härm heat flux electron transport model. This is not always sufficient for ICF as electrons may have mean free paths longer than the temperature gradient length-scales, as is the case for the laser absorption at the critical density. The simulations were repeated with a flux limiter of $f = 0.06$ and saw no change in the X-ray flux.

5.3.3 Higher Drive Powers

The ablation pressures predicted to be required for shock ignition are in the range of 200–300 Mbar^{58,59}. So far, the simulations in this study have generated peak ablation pressures of ~ 250 Mbar. It is interesting to consider if the scaling laws will hold up to higher pressures and what driver powers would be required to launch shocks of >300 Mbar. To model this, the simulations were re-run with a modified ignition spike profile. The compression portion of the pulse was kept the same up to 10 ns then the drive power in the spike portion was scaled by a numerical factor. The original 400 TW spike was scaled to form a number of profiles that peaked at 300 TW to 600 TW in steps of 100 TW. The new drive profiles were put into the h2d simulation described in section 5.3.1. The resultant soft X-ray flux profile was then put into a 1D HYADES simulation of a 1000 μm thick beryllium surface as in section 5.2.3. Table 5.1 shows the peak hohlraum temperature achieved in the 2D

Drive Profile	Peak Radiation Temperature	Peak Pressure
300 TW Peak	270 eV	206 Mbar
400 TW Peak	290 eV	251 Mbar
500 TW Peak	303 eV	270 Mbar
600 TW Peak	319 eV	310 Mbar

Table 5.1: Results of the 1 & 2D simulations investigating the drive powers required to produce ablation pressures of up to 310 Mbar. Shows the peak power of the drive pulse used and the corresponding maximum radiation temperature produced in 2D hohlraum simulations. Then shows the ablation pressure produced by that hohlraum radiation temperature in a 1D simulation using beryllium.

simulations and the peak ablation pressure produced in the 1D ablation simulations. It can be seen that for a >300 Mbar ablation pressure to be achieved, a 600 TW spike power must be used.

5.3.4 Scaling of Laser to X-ray Conversion and Ablation Pressure

The physical scaling of the simulations described in this chapter has been investigated and compared to some standard scaling laws from references 85 and 116 (discussed in more detail later). For the 1D simulations a series of snapshots were taken from the simulations. For each snapshot the ablation pressure, p_a was extracted and has been plotted against the corresponding X-ray drive temperature at that point in time. The results are plotted in figure 5.7a. The same process was carried out for the 2D hohlraum simulations with the hohlraum temperature and the corresponding laser drive power; these results are plotted in figure 5.7b. The blue lines in those plots are standard scaling laws.

It can be seen that there is a noticeable over-prediction of the pressure at higher radiation temperatures. For the peak of 319 eV the simulations calculated a pressure of 310 Mbar where the scaling law predicts 380 Mbar. There are two possible sources for this reduction in pressure. Firstly, this could signify a transition out of the subsonic regime. The analytical equation predicts that this transition will occur around 380 eV. However, in the actual case, this transition occurs at a much lower temperature (260 eV as was seen in chapter 4). The second possible cause for the reduction in the pressure is due to the acceleration of the ablation front. At this late stage in the drive, the ablation front of the beryllium surface is undergoing a significant amount of acceleration. In an accelerated frame, a pseudo-gravitational term appears in the momentum Rankine-Hugoniot momentum equation (equation 2.21). The ef-

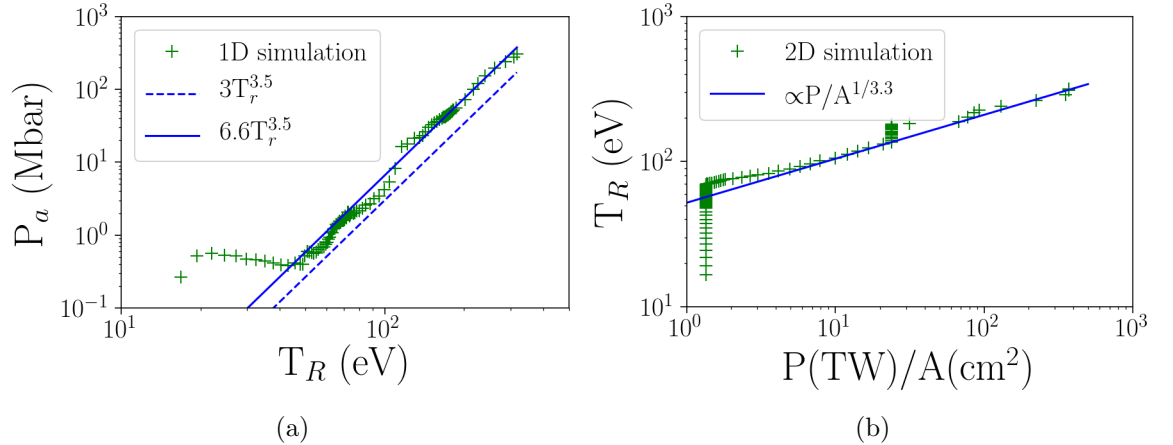


Figure 5.7: Figures showing (a) the X-ray radiation temperature to ablation pressure scaling and (b) the laser drive power to X-ray radiation temperature scaling. The results are taken from the 600 TW peak drive 1D and 2D simulations. Each cross shows the relation between the parameters at a snapshot in each of the simulations. The blue lines show scaling laws to be used as reference.

fect is to reduce the ablation pressure by $p_{\text{grav}} = g \int_{x_1}^{x_2} \rho dx^6$, which can reduce the scaling in equation 5.3 by up to a factor of $\times 2^{6,85}$.

For the conversion of laser energy to X-rays, the $p_a \propto P/A^{1/3.3}$ scaling comes from reference 85 and is based on experimental data from a number of facilities. It can be seen that the h2d simulation data agrees well with the scaling. Note that the original scaling law had an additional term that included a $\tau^{0.5}$ scaling with time. This has been neglected here as it is too simplistic a treatment for the complex pulse shape being used. However, the effect can still be seen in figure 5.7b in the form of the 2 vertical jumps. These correspond to foot and plateau regions of the drive pulse where the laser power remains constant for some time and the scaling increases. A more sophisticated time-dependent scaling is discussed later in section 5.4.4.

5.4 Comparison to Other Studies

5.4.1 Comparison to Experimental Data

The scaling of ablation pressure with X-ray drive temperature and hohlraum temperature with laser drive power has been compared to experimental measurements. Reference 97 details measurements of the ablation pressure of beryllium, copper-doped beryllium, germanium-doped plastic and high density carbon ablaters. The study measured the ab-

lation rates via time resolved X-ray measurements of the burn-through at the rear surface. One can then relate the mass ablation rates, \dot{m}_a to an ablation pressure via the sound speed of the ablated plasma, c_s by the following relation $P_a \propto \dot{m}_a c_s$. For a fully ionized plasma, the sound speed will be proportional to $T_R^{0.5}$. In this manner an ablation pressure can be inferred which, for beryllium, gave pressures of 40-140 Mbar for hohlraum temperatures of 160-240 eV (see figure 8 in reference 97). These measurements are consistent with the scaling determined in this study, as can be seen in figure 5.7a

A scaling law for hohlraum temperature with laser drive power can be found in references 85 (figure 56) and 116 (figure 4). This scaling law arises from experimental measurements made at the Nova, Phebus, GEKKO XII and Shenguang-II facilities. The scaling law given is of the form $\frac{P}{A} \tau^{0.5} \propto T_R^{3.3}$. This is the origin of the scaling used in figure 5.7b in which the scaling with time has neglected time for simplicity. In the experimental data, the scaling holds well up to 200-300 TW cm⁻² s^{0.5} where it begins to fall off somewhat. The source of this fall off is not made apparent in the literature but as the drive powers being used in this work lie in that fall off region, a direct comparison to similar experimental results is appropriate.

The study in reference 115 achieved similar hohlraum temperatures to the simulation work carried out here. Experimental measurements were taken of smaller scale hohlraums at lower drive powers. In that work, an X-ray rise of 200 eV to 300 eV was observed in a rise time of 0.5 ns for a 300 TW pulse, almost twice the rate of rise that was observed for the 400 TW ignition spike described in section 5.3.1.

5.4.2 Comparison to Other NIF pulses

There exist a few numerical studies that use laser drive parameters notionally similar to the ones presented in this work^{91,117,118}. It is valuable to directly compare those results to illustrate the unique characteristics of the pulse shape used in this study. Firstly, the work in reference presented in reference 117 and 118 shows hohlraum temperature profiles produced from high and low-foot NIF pulses (figure 1 from reference 117). The high-foot drive profiles used at the NIF were developed to raise the adiabat of the fuel in an effort to increase the resistance to Rayleigh-Taylor instabilities¹¹⁸. Examples of the the low and high-foot NIF

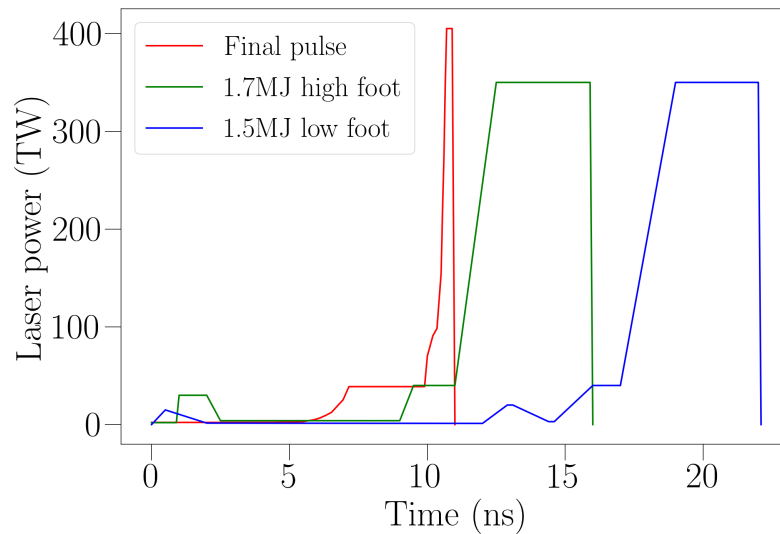


Figure 5.8: A graph showing how the drive pulse profile used in the hohlraum simulation described here compares to the standard high and low-foot NIF pulse designs. The 400 TW laser pulse from the present work is shown in red compared to the high-foot pulse (green) and the low-foot pulse (blue) from reference 118.

pulses are shown in figure 5.8. Secondly, we refer to the drive profile used in the high density carbon ablator experiments on NIF⁹¹. High density carbon ablators are favoured because shorter duration pulses can be used, thus reducing the effects of hohlraum wall expansion which in turn allows for a lower density gas-fill and lower levels of parametric instabilities. An example of the shorter, high density carbon drive pulse can be seen in figure 5.10a. The high-foot and high density carbon drive pulses exhibit similar final rises in laser power to the one used here ($\sim 100\text{--}400$ TW in ~ 1 ns).

To make a comparison, the high-foot and low-foot drive profiles along with the high density carbon drive profile were simulated in h2d, this time using the larger hohlraum dimensions as were used in the respective studies. Figure 5.9 shows the hohlraum temperature profiles produced from the low and high-foot pulses. For comparison, the low and high-foot radiation temperature profiles from reference 117 are plotted as solid lines. Overall the profile shape and rise times show good match. However, the high foot profile is shifted a little later in time due to the use of slightly different laser drive pulse. When comparing with the shock-ignition-like profile from figure 5.6, even with similarly fast rises in drive power, the low-foot and high-foot radiation profiles show a slower overall rise >3 ns from 200 eV to 300 eV when compared to the one developed in this study. This is also true of the high density carbon

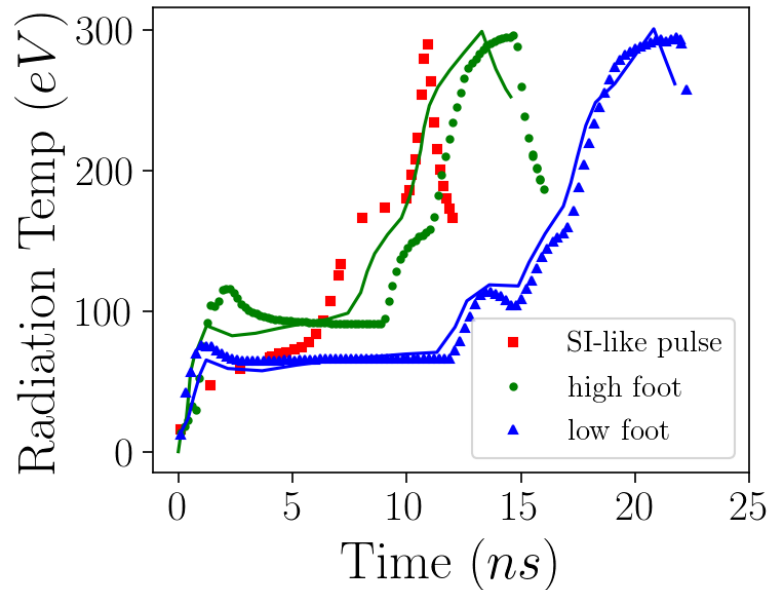


Figure 5.9: The NIF low and high-foot pulse profiles from figure 5.8 have been put into the 2D 5.75 mm diameter hohlraum simulation as described in section 5.3.1. The resultant hohlraum temperature profiles are displayed compared to the hohlraum temperature achieved using the SI-like 400 TW peak pulse. For comparison, the low and high-foot radiation temperature profiles from reference number 117 are shown as solid lines (extracted using WebPlotDigitizer⁹⁹)

pulse as can be seen in figure 5.10.

There exist a number aspects of the shock-ignition-like drive pulse that have resulted in such a fast rise. Firstly, quite simply, the peak drive power is higher and the rise time is lower. In this way, more time is spent at higher driver powers which will clearly push the hohlraum temperature up faster. Secondly, the plateau before the ignition spike lasts longer. As the conversion efficiency increases with time, the radiation temperature will be higher at the time of the ignition spike. This can be observed in figure 5.9 where the plateau region is well above that of the high-foot pulse, even with a similar drive power. Consequently, the required jump up to 300 eV is smaller. That, combined with the increased conversion efficiency, contributes to the faster rise time of the ignition spike. In the shock-ignition-like pulse there is also an initial bump 300 ps before the main portion of the ignition spike. This speeds up the initial rise in temperature allowing for a more consistent increase overall. Finally, the high and low-foot pulses use a larger, 5.75 mm diameter hohlraum, which will push the peak radiation temperature down. This will be examined in more detail in the next section. The combination of these effects results in a much faster rises being observed in the work presented here.

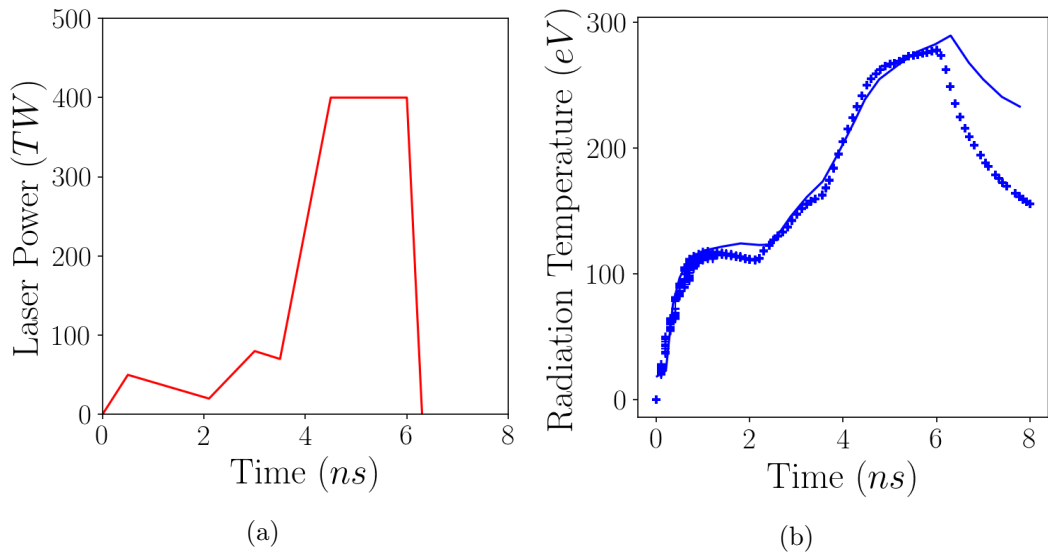


Figure 5.10: (a) The 6 ns laser drive pulse used in the high-density-carbon ablator shots from reference 91. (b) The X-ray radiation profile that was produced in h2d using the drive profile in (a) and a 6.20 mm diameter hohlraum. For comparison the radiation temperature profile from reference 91 is shown as a solid line (extracted using WebPlotDigitizer⁹⁹)

5.4.3 Varying Hohlraum Size

In the previous section, it was highlighted that hohlraum size is an important factor in determining the maximum achievable hohlraum temperature. For this reason, a simple study was carried out to investigate the drive powers required to produce a 300 eV radiation temperature in four hohlraums of different size. Reference 94 predicts the required drive powers for 300 eV for three hohlraum sizes 5.75 mm, 6.20 mm and 6.72 mm; the dimensions of these hohlraums are outlined in figure 5.11. Simulations using h2d were run for these three hohlraum sizes as well as the hohlraum dimensions used in the simulations described in section 5.3.1. In each case, a uniform drive pulse irradiated the hohlraum.

As described in the earlier simulations, the hydro-motion was turned off before the wall expansion could cause any bow-ties. For these simulations, due to the higher drive powers at earlier times, hydro-motion was turned off earlier at around 0.75–1.0 ns depending on the level of wall expansion for each simulation. The hohlraum temperature was taken to be the internal radiation temperature after 4 ns. The results are summarised in table 5.2. It can be seen that the predicted drive powers from reference 94 are matched well, with the 5.75-6.72 mm hohlraums producing near 300 eV peak temperatures. The drive power for the 5.10 mm hohlraum was found by trialling a few drive powers in steps of 10 TW and 270 TW

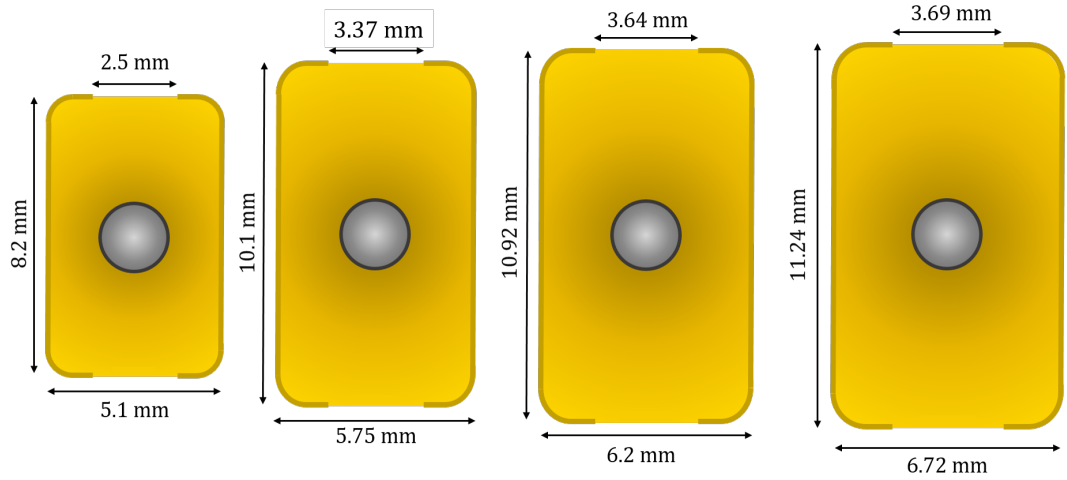


Figure 5.11: Schematic diagram of the series of hohlraum sizes used in the h2d simulations. Dimensions of the hohlraum and the laser entrance hole are shown, the capsule size remains the same in each hohlraum.

Drive Power	Total Energy	Hohlraum Diameter	Hohlraum Temperature
250 TW Peak	1.00 MJ	5.10 mm	298 eV
380 TW Peak	1.52 MJ	5.75 mm	298 eV
420 TW Peak	1.68 MJ	6.20 mm	290 eV
480 TW Peak	1.92 MJ	6.72 mm	293 eV

Table 5.2: A table summarising the peak hohlraum temperatures produced in the different hohlraum dimensions that are outlined in figure 5.11. In each case the peak of the laser drive power was chosen in order to achieve a hohlraum temperature close to 300 eV.

using the power that was closest to achieve a peak of 300 eV. According to the $T_R^{3.3} \propto \frac{P}{A} \tau^{0.5}$ scaling law, the required power should scale linearly with respect to the inner surface area of the hohlraum. The required drive power has been plotted against the inner surface area in figure 5.12. A linear relation between area and power has also been plotted, it can be seen that area and power do follow an approximately linear relationship.

5.4.4 Time-Dependent Laser to X-ray Conversion

The laser to X-ray scaling relations used previously have neglected any considerations of time with the assumption that the albedo of the hohlraum wall remains constant. Whilst most of the flux incident into the hohlraum wall is re-emitted from the conversion layer, some of it is deposited in the wall as thermal energy. Over time, the wall will get hotter and, by the Stefan-Boltzmann law, will emit more radiation. The result is that, as time goes on, the wall albedo will increase and therefore, so will the scaling of laser drive power

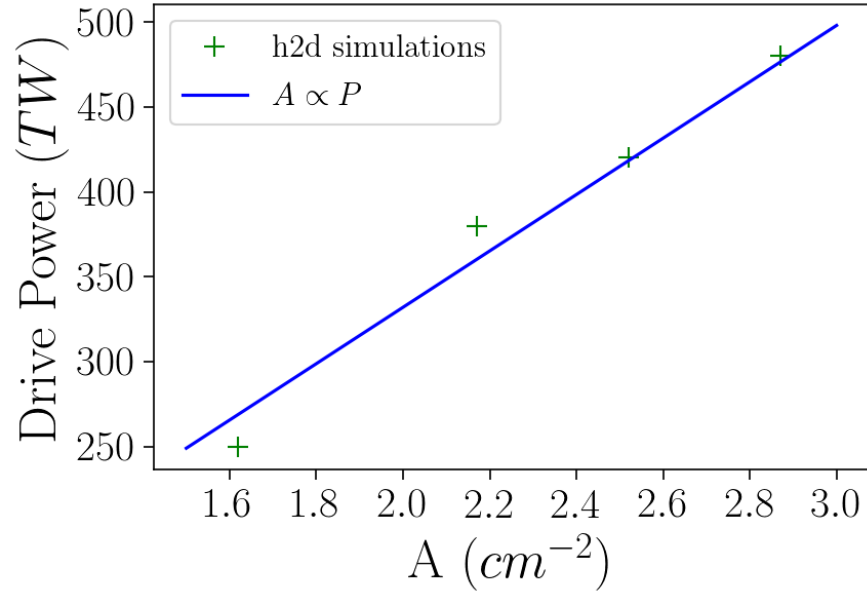


Figure 5.12: Results of the h2d simulations for varying hohlraum sizes. Shows the laser drive power required to generate a hohlraum temperature of 300 eV plotted against the total inner surface area of the hohlraum wall.

with hohlraum temperature. This scaling is considerably weaker than the scaling with the drive source intensity but must still be accounted for accurate modelling. One can model an increasing albedo with the addition of a temporal component in the scaling. Here, the power law proposed in reference 47 is considered. The physics of this scaling laws is outlined in section 2.6.2. The Basko scaling gives the re-emitted flux, S_r as

$$S_r = 14.1[E_a(t, \mathbf{r})]^{0.510}[S_a(t, \mathbf{r})]^{0.748}, \quad (5.4)$$

where E_a is the total energy absorbed by the hohlraum, related to the absorbed flux, S_a by

$$\frac{\partial E_a(t, \mathbf{r})}{\partial t} = S_a(t, \mathbf{r}). \quad (5.5)$$

This scaling relation has been compared with the results of the h2d simulations. The deposited laser power is extracted from the laser deposition model in h2d. Summing this over all the zones in the gold region gives the total laser power deposited in the hohlraum. Then, assuming the incoming radiation is deposited across the entire hohlraum surface, taking the inner surface area of the 5.11 mm by 8.2 mm to be 1.62 cm² one can find S_a the absorbed

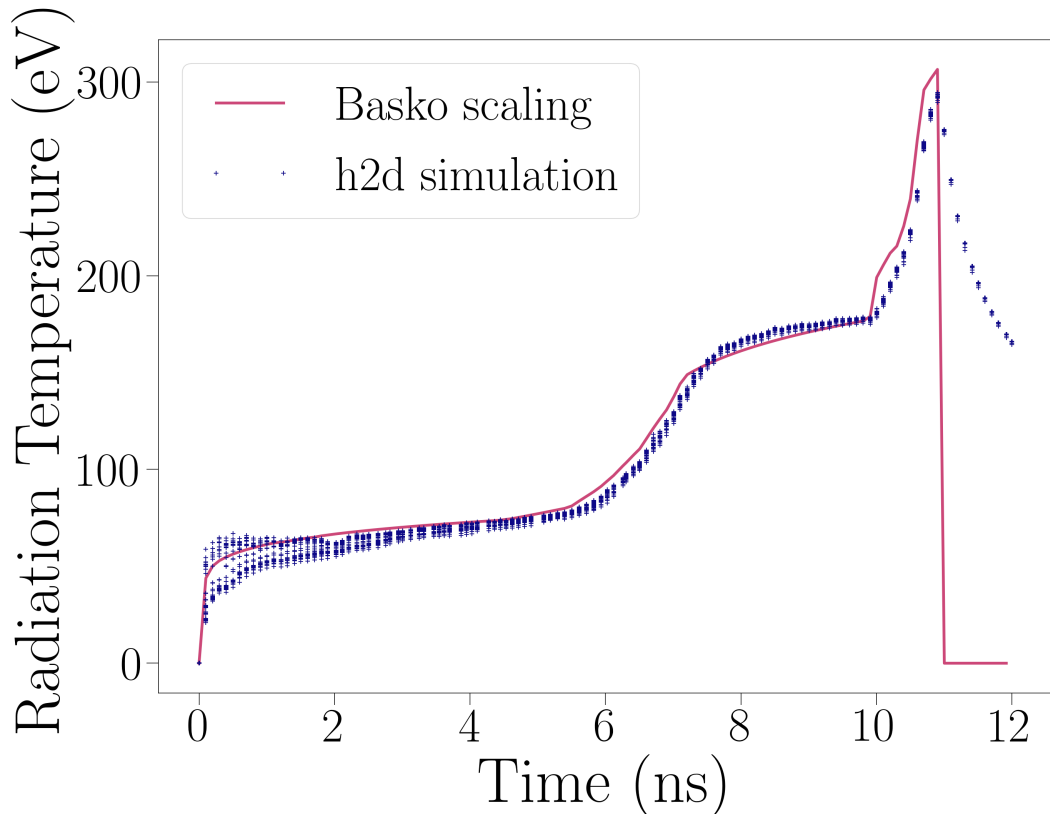


Figure 5.13: A graph comparing the X-ray profile produced in 2D simulations to the profile predicted by Basko's time-dependent scaling law. The hohlraum temperature from the 400 TW peak pulse 5.75 mm hohlraum is shown as blue crosses. Basko's⁴⁷ time-dependent scaling law (equation 5.5) is shown as a solid line.

laser flux. The total absorbed energy is then found by integrating the deposited laser energy over time, or in other words, $E_a = \int S_a dt$. The prediction from this relation is plotted in figure 5.13. It can be seen that there is a good match to the simulated data.

5.4.5 Suprathermal Electrons

At 400 TW, the laser intensity required to launch the ignition shock in shock ignition will be over the threshold for parametric instabilities. Parametric instabilities were discussed in detail in section 2.2.3. These effects are of great interest in direct-drive shock-ignition research as they will create a population of suprathermal electrons in the ablated plasma that may propagate into the fuel. Whether these suprathermal electrons will pass the shock front, causing fuel pre-heat is still an open question and the subject of much interest. In the case of an indirect-drive shock-ignition scheme, the electrons will be created in the plasma

that fills the hohlraum, along the path of the laser. The direction of the produced electrons is still not known, so it is not possible to definitively say whether or not or how they will affect the capsule implosion. However, they will degrade the conversion to X-rays by taking energy out of the laser. For this reason, it is important to briefly consider their effects here. In CHS ignition experiments on the NIF, it is the initial stages of compression that are most susceptible to hot electron preheat¹¹⁹. In shock ignition, the laser power will be lower than CHS ignition at earlier times. It is therefore only the igniter peak part of the pulse that may cause significant preheat. The spot size of the 192 NIF beams at best focus (at the laser entrance hole) are around 0.004 cm^2 ⁸⁵. This would give the 400 TW peak power pulse a maximum intensity of $8 \times 10^{14}\text{ W cm}^{-2}$. This is above the threshold for parametric instabilities^{120,121}. In a plastic ablator direct-drive shock-ignition target, the igniter shock is launched at a time where the areal fuel density is approaching $\sim 10\text{ mg cm}^{-2}$ ¹²². This should be dense enough to stop electrons of energies up to 100 keV¹²³. Measurements have been made on the NIF using a 400 TW peak pulse for two different capsule ablaters. Pre-heat levels were calculated for electron energies of $>100\text{ keV}$ ¹²⁴ for plastic and $>170\text{ keV}$ ¹¹⁹ for beryllium. In general, the amount of preheat is within acceptable limits but a recent study has shown, in some cases, beaming can lead to a higher energy deposition in the capsule shell¹²⁵. These results suggest that the 400 TW pulse used here would produce acceptable levels of hot electron preheat. However, if poor laser to X-ray conversion meant that higher powers were required, the intensities at the LEH could go above $1 \times 10^{15}\text{ W cm}^{-2}$, which is in the region of significant collisionless absorption.

Chapter 6

Controlling X-ray Flux Inside Hohlraums Using Burn-through Barriers

In this chapter, a new technique for controlling X-ray flux inside hohlraums using burn-through barriers is proposed. To begin with, some motivation for this technique is outlined. Next, the physics of X-ray burn-through is investigated using the 1D radiation hydrodynamics code HYADES. The burn-through properties for different materials are compared. Following that, more sophisticated, multi-layer barriers are used to delay X-ray burn-through without reducing the transmission of X-rays through the barrier. Finally, the application of spatially varying burn-through barrier sources to hohlraum interiors is investigated using the view-factor code F3D.

6.1 Introduction

Hohlraums are high-Z casings used in indirect drive ICF to create a bath of soft X-rays that drive capsule implosions. An in-depth discussion of indirect drive was given in section 2.6. The spatial and temporal properties of the X-ray field inside the hohlraum must be precisely controlled to achieve adequate compression of the fuel. Jumps in the intensity of the X-rays must occur at specific times in order to launch a series of shocks into the capsule that

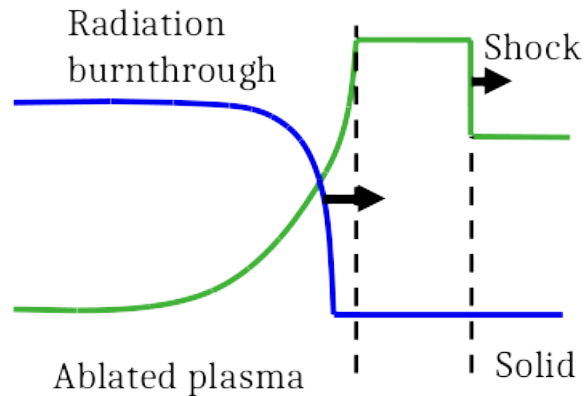


Figure 6.1: A schematic diagram of a subsonic burn-through wave. The radiation front is succeeded by a shock front travelling into the solid material. The blue line shows the radiation front which drops to zero as the density (green line) of the material increases.

drive the compression¹⁰⁹. The implosions also require a high degree of spatial uniformity in order to maintain spherical symmetry^{9,15,16}. Traditionally, the spatial characteristics of the X-rays are managed through modification of the driver properties or target geometry. For example, in laser indirect drive ICF, the pointing of the beams is chosen so that the resulting absorption sites will lead to optimum spherical irradiation of the capsule. The discussion of indirect drive experiments is limited here to ICF, however attention is drawn to several HEDP studies that require precise control of X-ray flux profiles^{78,126–131}.

The term burn-through refers to the propagation of a radiation wave completely through a material up to the rear surface. For applications such as those considered here, the material should be sufficiently thin such that a significant fraction of the drive power is transmitted through. The material through which the radiation wave is burning is referred to as a burn-through barrier. In the case of subsonic propagation, the radiation wave will set-up a shock front. A schematic of a subsonic burn-through wave is shown in figure 6.1. The subsonic burn-through wave will propagate through the barrier until it reaches the rear surface. At which point the shock front will break out, triggering disassembly of the barrier and a sudden burst of X-ray radiation.

Previous work has been conducted to examine the interaction of high-intensity lasers and thin high-Z foils. Such burn-through foils were developed for use in HEDP experiments as X-ray sources^{132–137}. These burn-through foils are quite different to the barriers that are being examined in this work. Here we consider burn-through barriers that are irradiated

directly by a soft X-ray source. Some work has already been carried out on X-ray driven burn-through but with a different focus. Previous studies used X-ray driven burn-through as a diagnostic tool for measuring ablator pre-heat¹³⁸ and hohlraum wall re-emission¹³⁹. This work studies X-ray driven burn-through in a different context. It is proposed that burn-through barriers may be used to modulate the X-ray flow inside hohlraums. The work in this chapter shows how burn-through barriers can significantly alter the spatial and temporal properties of X-rays burning through into an adjacent hohlraum chamber.

This application of burn-through barriers would be useful at facilities which can generate high intensity X-ray sources to study HED conditions but are limited in their ability to control the X-ray characteristics. For example, hohlraums employed on Z-pinch facilities are capable of generating large X-ray fluxes^{140–142} but limited in their control of the source. Shaping the pulse in time requires complex nested z-pinch array targets^{142,143} and spatial shaping is limited to power balancing of the drive sources and modification of the hohlraum geometry¹⁴². Even at extremely sophisticated facilities such as the NIF, there are still outstanding issues in terms of producing a uniform X-ray drive source^{144–146}. The hotspots created at the laser absorption sites cause X-ray drive asymmetries¹⁴⁷ and can also be a source of pre-heat due to M-band emission in the gold material¹⁴⁸. Burn-through barriers may be able to spatially modulate the X-rays, as well as providing some shielding of hard X-rays as they could be placed between the laser absorption sites and the payload. Additionally, there is an issue of time-lag in the conversion of laser to X-ray energy in hohlraums; this was discussed in detail in chapter 5 with regards to producing shock-ignition-like X-ray drive profiles. Again burn-through barriers may be useful in this context through the temporal shaping they could provide. A study is discussed later in this chapter on how a burn-through barrier could be used in the application of shock ignition.

6.2 1D HYADES Burn-through Barrier Simulations

The first section in this chapter describes a study carried out in HYADES that examined burn-through barriers made up of a single material. The burn-throughs of low, middle and high atomic number materials over a range of thicknesses are compared. For each material,

the dynamics of the burn-through wave is investigated. A number of burn-through metrics are also defined. Finally, the effects of time-varying X-ray sources are examined.

6.2.1 Simulation Set-up

The simulations were carried out in 1D planar geometry using HYADES. A description of all of the physics models used in HYADES was given in chapter 3. The simulations use a flux-limited Spitzer-Härm model to handle thermal transport. An average-atom LTE ionisation model was employed. Radiation transport was handled with a multi-group diffusion model with 100 groups with upper bounds ranging from 5.0×10^{-4} keV up to 30 keV. The flux out of the rear surface was extracted from the group boundary emission value in HYADES. This is given as the total flux summed from the boundary emission in each spectral group. The technique for this is outlined in appendix B (section 8.2). All the 1D simulations described in this chapter used these models unless it is explicitly stated otherwise.

The mesh structure of the targets varied from simulation to simulation. In the case of the single material barriers, a constant mesh feather value of 1.1 was used throughout the whole mesh. The number of mesh lines was chosen in order to maintain sufficient spatial resolution throughout the simulation. The barriers made up from multiple materials (section 6.3) used a different technique for mesh feathering. The front surface material is feathered as before using a ratio of 1.1 throughout the mesh. The mesh for the second material then used constant spacing. The number of mesh lines was then chosen such that the mass in each region was roughly equal. This satisfies a condition for stability in HYADES which requires adjacent mesh regions to have no more than a factor of 2 difference in the mass values. The mesh in the shock-ignition burn-through barrier was structured differently to the rest and is described in more detail in that section.

6.2.2 Comparison of High-Z Mid-Z and Low-Z Burn-through

To begin, a comparison is made between the radiation burn-throughs of low-Z, mid-Z and high-Z barriers. The burn-through of a constant 314 eV X-ray source through low-Z beryllium at 1.845 g cm^{-3} (SESAME #2020), mid-Z copper at 8.93 g cm^{-3} (SESAME #3330) and high-Z gold at 19.3 g cm^{-3} (SESAME #2700) are compared. The thicknesses of the targets were

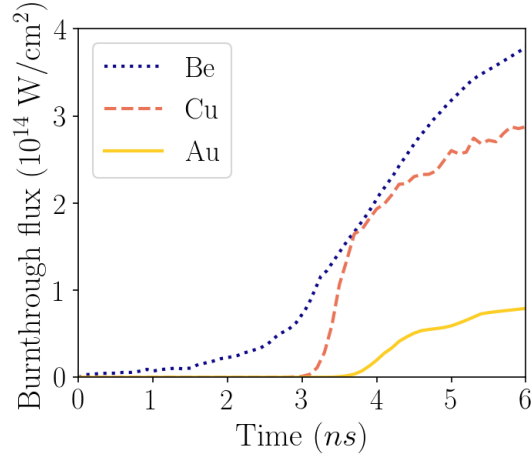


Figure 6.2: A plot is shown of the rear-surface flux against time for three different burn-through barrier targets. Each of these barriers were simulated in HYADES using a 314 eV ($1 \times 10^{15} \text{ W cm}^{-2}$) Planckian X-ray source. The materials were 15 μm gold (solid line), 30 μm copper (dashed line) and 800 μm beryllium (dotted line).

chosen through trial and error such that the burn-through wave would reach the rear surface at 3 ns. The emitted flux from the the rear surface over time is shown for the three materials in figure 6.2. It can be seen that all three exhibit a sigmoid-like shape in the rear-surface flux profile. However, the rise for beryllium is much more gradual and there is a significant level of emission from the rear surface right from the start of the simulation. The explanation for this becomes apparent upon examination the radiation temperature and density profiles through the barriers.

First, the burn-through wave in the gold barrier will be examined. Figure 6.3 shows a rear-surface flux profile upon which three key points in time have been highlighted. At each of those times, snapshots of the mass density and radiation temperature profile through the barrier have been plotted. These snapshots build up a picture of the dynamics of the burn-through. In the early stages of the burn-through, a shock-front is set-up ahead of the radiation front. The radiation temperature falls to zero where the density peaks as the plasma is sufficiently opaque to fully absorb the radiation wave. This is an example of the subsonic ablative heat wave which was introduced in section 2.5.1 and has already been discussed several times in this thesis. At ~ 3 ns the shock front reaches the rear surface of the barrier and the barrier begins to rapidly disassemble. The density drops and the radiation temperature at the rear surface of the barrier rises sharply. From then on the gold plasma

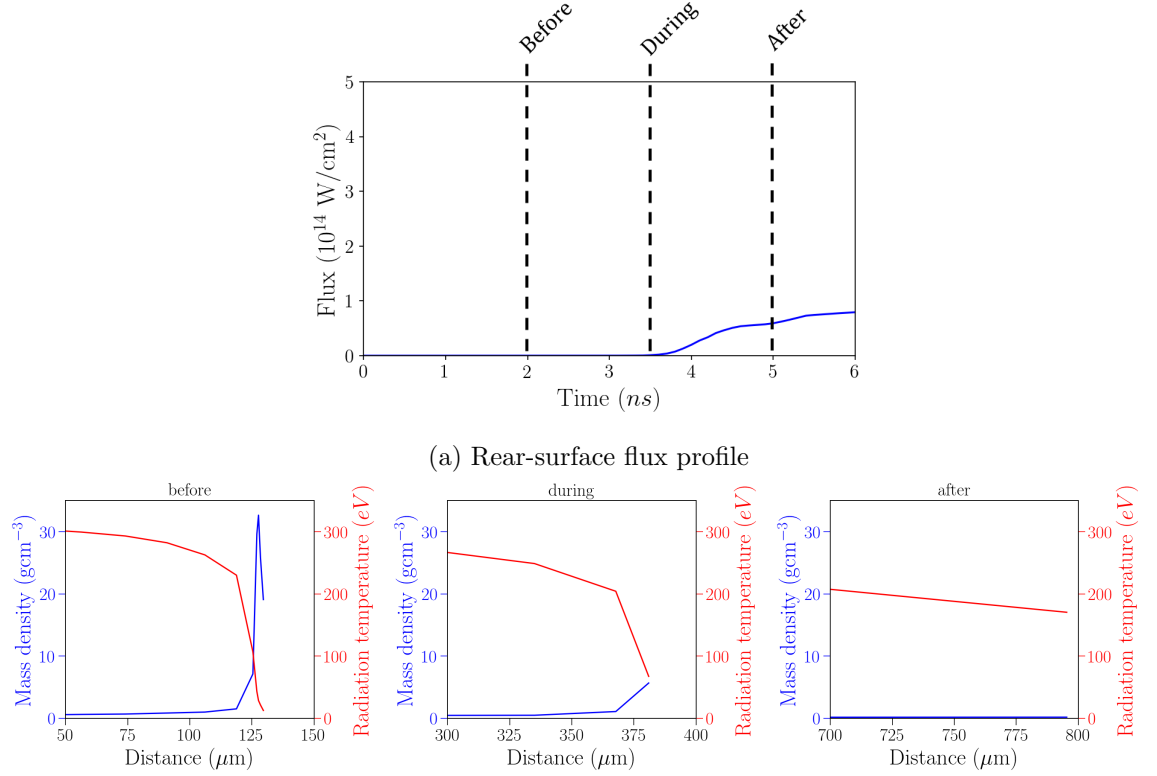


Figure 6.3: A figure that shows the simulation results of the burn-through of a 314 eV Planckian X-ray drive source through 15 μm of gold. The rear-surface flux against time is shown in the top figure. Three points in time are highlighted before, during and after the burn-through. The density (blue line) and radiation temperature (red line) profiles at those points in time are then shown in the three plots below.

continues to expand, becoming more transparent, which results in a slow rise in flux until the end of the simulation.

Copper is examined next. The simulations of a 314 eV source irradiating a 30 μm copper barrier are displayed in figure 6.4. The dynamics of the burn-through are similar to that of the gold barrier. An ablative heat wave is set-up and propagates up to the rear surface where it breaks out. However, copper requires a thicker barrier in order to achieve the same 3 ns delay and a larger amount of flux burns through the barrier. This is to be expected as the speed of the radiation wave in the target and the total burn-through flux is related to its opacity. The analytical solution for a Marshak wave driven by constant flux from section 2.5.1 gave the penetration distance as

$$x_p = \left(\frac{8\sigma T_0^4}{3k_a^{(R)} \rho \epsilon_0} t \right)^{\frac{1}{2}}. \quad (6.1)$$

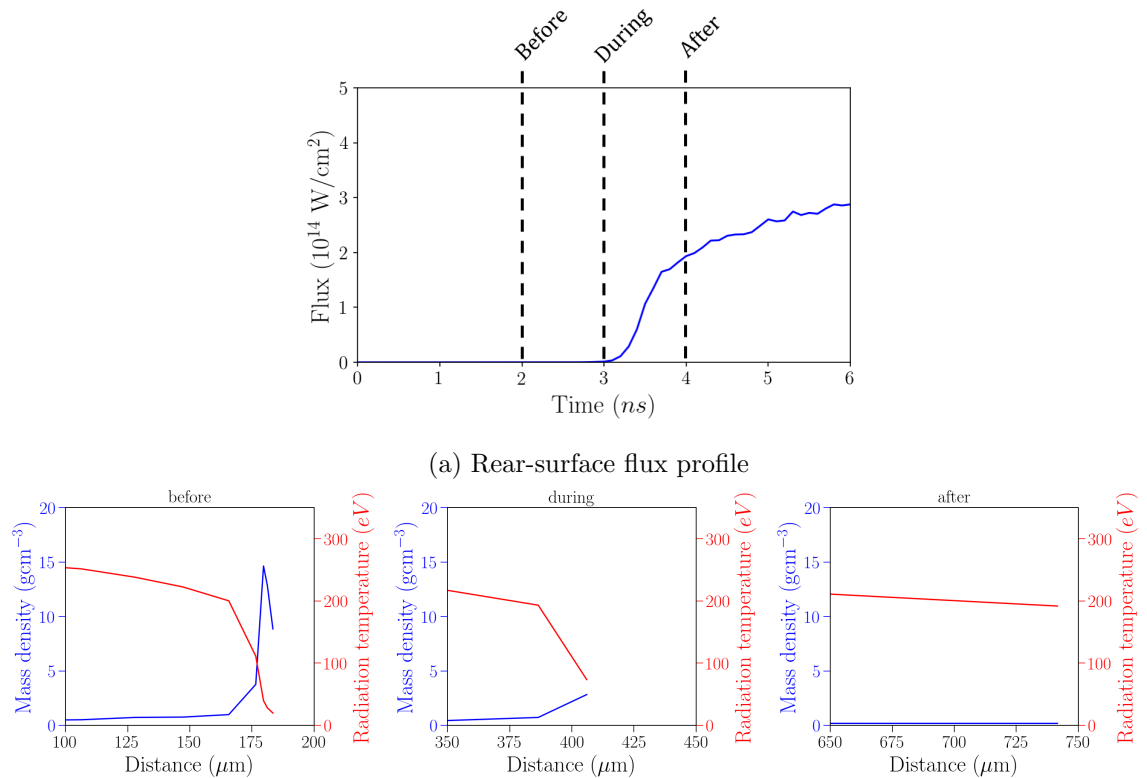


Figure 6.4: A figure that shows the simulation results of the burn-through of a 314 eV Planckian drive source through 30 μm of copper. The rear-surface flux against time is shown in the top figure. Three points in time are highlighted before, during and after the burn-through. The density (blue line) and radiation temperature (red line) profiles at those points in time are then shown in the three plots below.

As copper has a lower opacity, for a given time, equation 6.1 predicts the penetration distance will be less. Similarly, in lower opacity targets, more energy is coupled into kinetic motion resulting in a faster shock front. Therefore, a lower opacity material will require a thicker target to delay the start of the burn-through rise.

Finally, the results of the burn-through in a 800 μm thick beryllium barrier simulation can be seen in figure 6.5. The burn-through profile for the beryllium target is quite different. From the first step in the simulation, the X-ray flux through the beryllium is already significant. Looking at the density profile in the beryllium it can be seen that, whilst there is a perturbation in the density profile, no significant shock-front is built up. This is because the temperature of 314 eV is above the critical temperature for transonic behaviour. This perturbation does not become opaque enough to hold back the radiation wave and the X-ray drive is able to penetrate deep into the material. For this reason, a large amount of flux

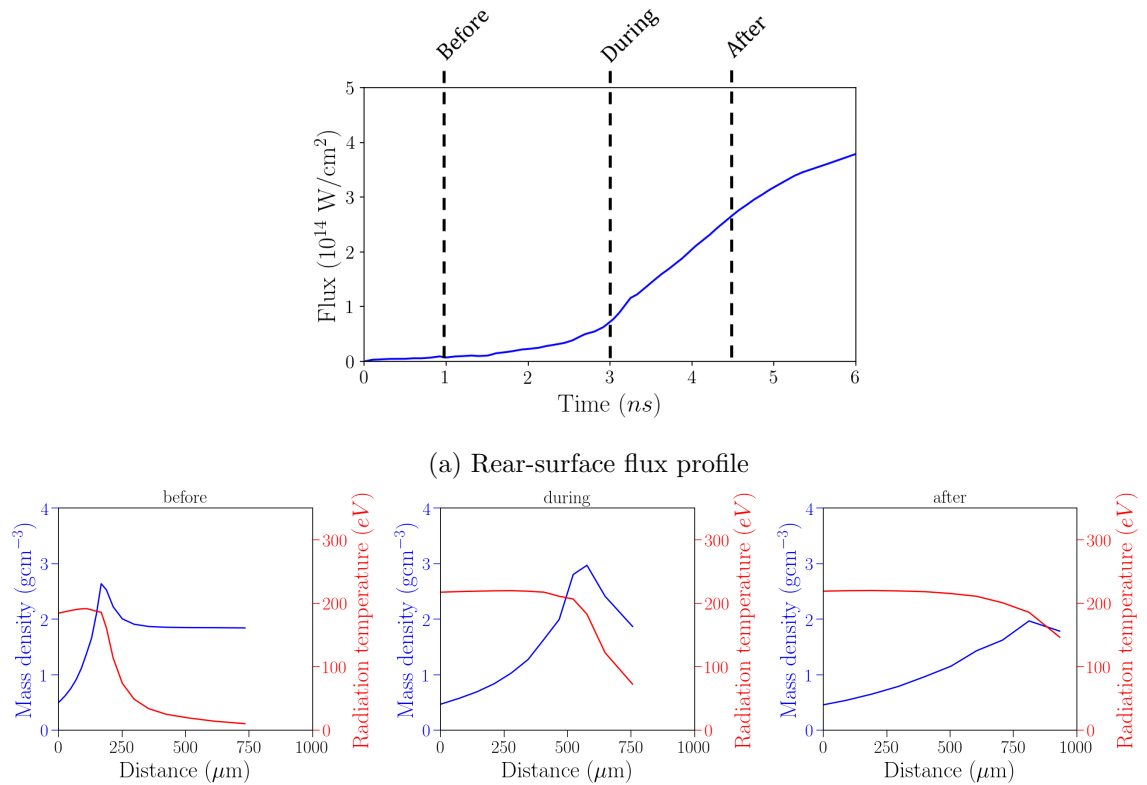


Figure 6.5: A figure that shows the simulation results of the burn-through of a 314 eV Planckian drive source through 800 μm of beryllium. The rear-surface flux against time is shown in the top figure. The burn-through rise shape is not as clear as it was for copper (fig 6.4) and gold (fig 6.3) but before during and after points have been approximately defined. The density (blue line) and radiation temperature (red line) profiles at those points in time are then shown in the three plots below.

penetrates entirely through the barrier at early times. The rate of flux then continues to go up as the barrier expands. Eventually the density perturbation reaches the rear surface and the barrier begins to slowly disassemble.

The spectral structure of the rear surface flux has been plotted in figure 6.6. It can be seen that at early times (1 ns), only the high-energy tail of the source is being transmitted through the target. As the target expands more of the high energy tail is able to transmit through (3 ns). Then, at 4.5 ns after the radiation front has the reached surface and the target has disassembled, a significant portion of the entire spectrum is transmitted through the target. The double peak structure is a result of the k-edge, which in beryllium occurs at 112 eV¹³⁶. This section has shown how X-ray the propagation of burn-through waves changes with increasing atomic number. In the next stage of work, it is examined how varying the thickness of these barriers alters the burn-through characteristics.

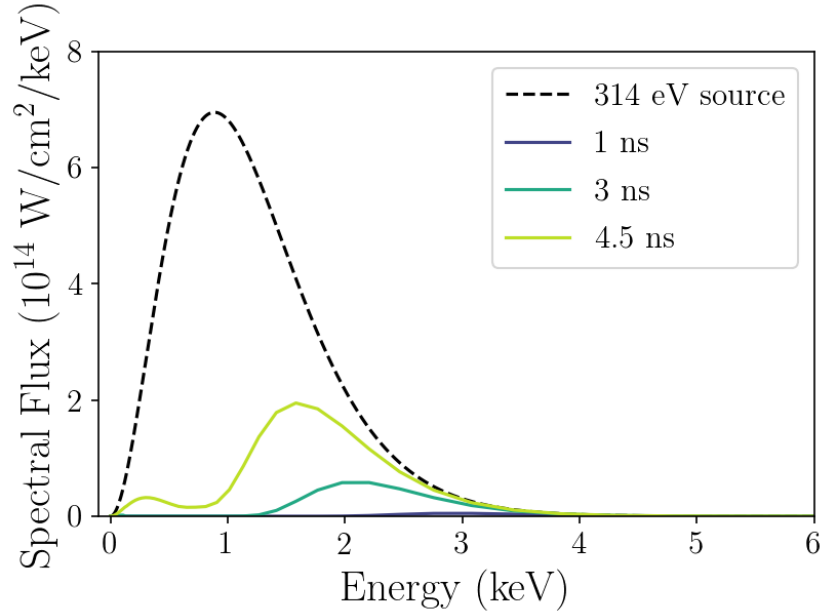


Figure 6.6: Plot of the spectral structure of the burn-through radiation transmitting through 800 μm of beryllium at different stages of the burn-through. The black dotted line shows the 314 eV source. The times are the same as the 'before', 'during' and 'after' points from figure 6.5.

6.2.3 Varying Thickness

A series of simulations were run for a number of materials using the same simulation set-up described in section 6.2.1. Three burn-through metrics are defined: the burn-through start time, the maximum rise rate and the total burn-through flux. Figure 6.7 shows how the metrics are defined using the burn-through flux profile of the 30 μm copper target as an example. The first two metrics were defined from the numerical time derivative of the rear-surface flux profile. The time derivative was calculated using a central differences technique. The maximum rise rate is simply the peak value of the derivative. The burn-through start time is defined as the first point in time where the derivative becomes higher than 10% of the maximum rise rate. Finally, the total burn-through flux is defined as the value of the rear-surface flux at 15 ns.

The simulations used four materials with different thickness ranges. The materials chosen were beryllium, aluminium, copper and gold. For each material the thickness range was chosen such that the start of the burn-through rise would occur between 1 ns and 10 ns. The results are summarised in the plots in figure 6.8.

In general, the four materials exhibit similar trends. Increasing the thickness of a barrier

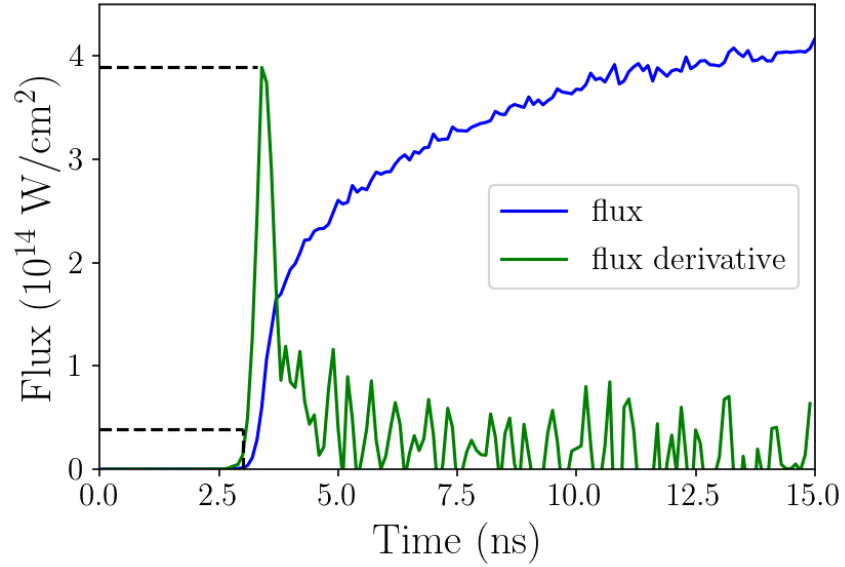


Figure 6.7: A plot showing how the burn-through metrics are defined. Plotted in blue is the rear-surface flux for a 15 μm copper burn-through barrier. The time derivative (green line) was done numerically using central differences and has been normalised to fit on the graph. Displayed are the points of maximum rise, the burn-through rise start time and the burn-through flux at 15 ns.

delays the start of the burn-through whilst decreasing the total flux through the target and the steepness of the burn-through rise.

6.2.4 Rising Flux Profile

In the previous section, the burn-through barriers were driven with a constant flux source which is not particularly realistic. It will take the drive source some amount of time to rise before it reaches a stable value. Such a rise will affect the dynamics of the burn-through. The effect of simple linearly rising sources is investigated here for beryllium and copper barriers. A range of sources with different power profiles were used. The sources begin at a flux of 0 and rise to 314 eV over 1 ns, 2 ns, 5 ns and 10 ns. The simulations used a slightly different radiation group structure than was describe in section 6.2.1. The groups used 100 upper bounds spaced from 5.0×10^{-4} keV to 5 keV.

The results for the 30 μm copper barrier are shown in figure 6.9. As one might expect, for the profiles with a slower rise, the burn-through occurs at a later time. The total flux through the target and the steepness of the burn-through rise stay roughly the same. A less intense X-ray drive in the early stages results in a weaker, more slowly propagating shock front in

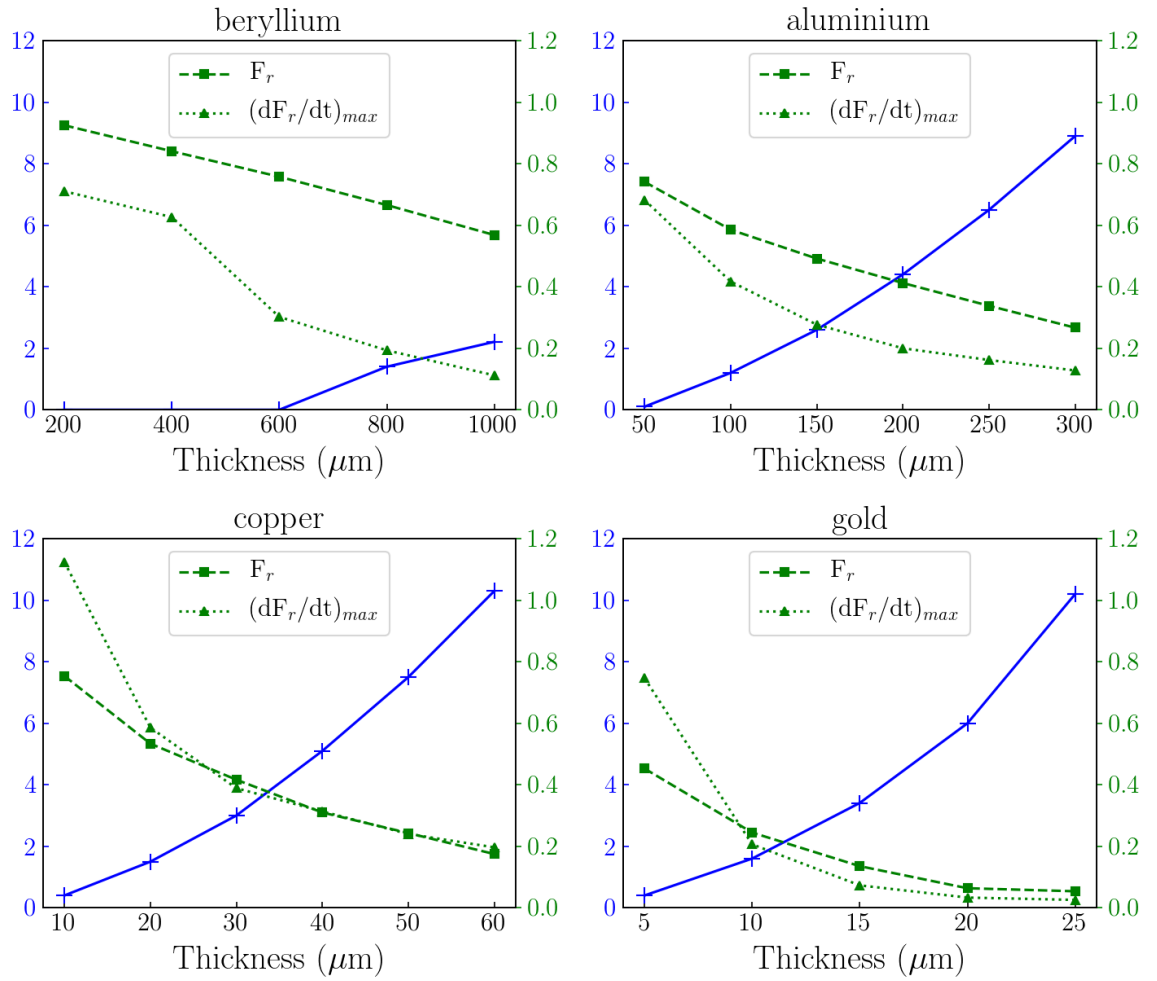


Figure 6.8: Plots to show how the burn-through metrics vary with thickness for beryllium, aluminium, copper and gold when driven with a 314 eV Planckian X-ray source. The blue axes represent the start rise time in nanoseconds. The green axes give the flux in units of 10^{15}W cm^{-2} and the maximum rate of change of flux in units of $10^{15} \text{W cm}^{-2} \text{ns}^{-1}$. The lines do not represent a fit to data they are only there to guide the eye.

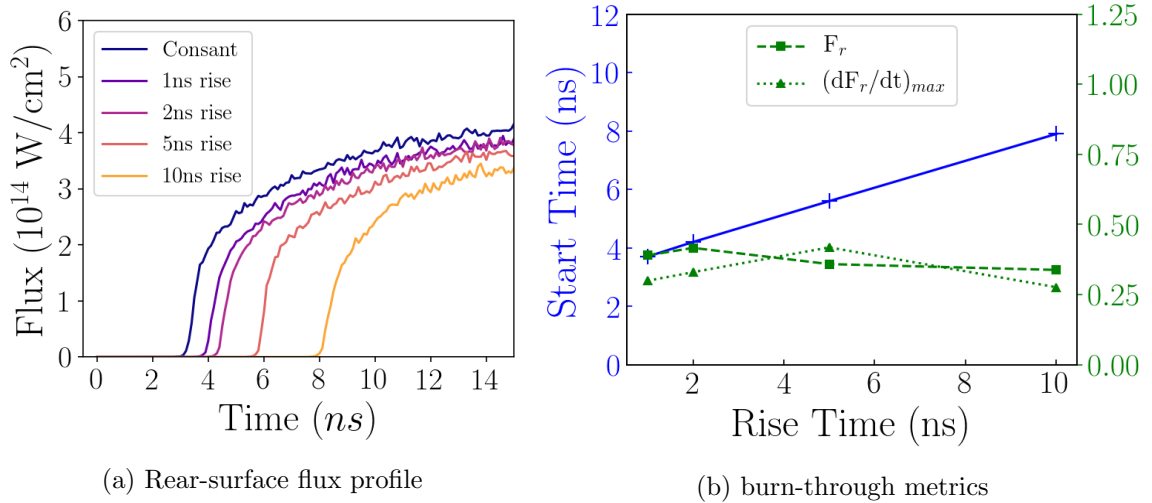


Figure 6.9: Plots showing the (a) rear-surface flux profiles and (b) burn-through metrics for a number of drive sources using a range of rise times up to 314 eV irradiating 30 μm of copper.

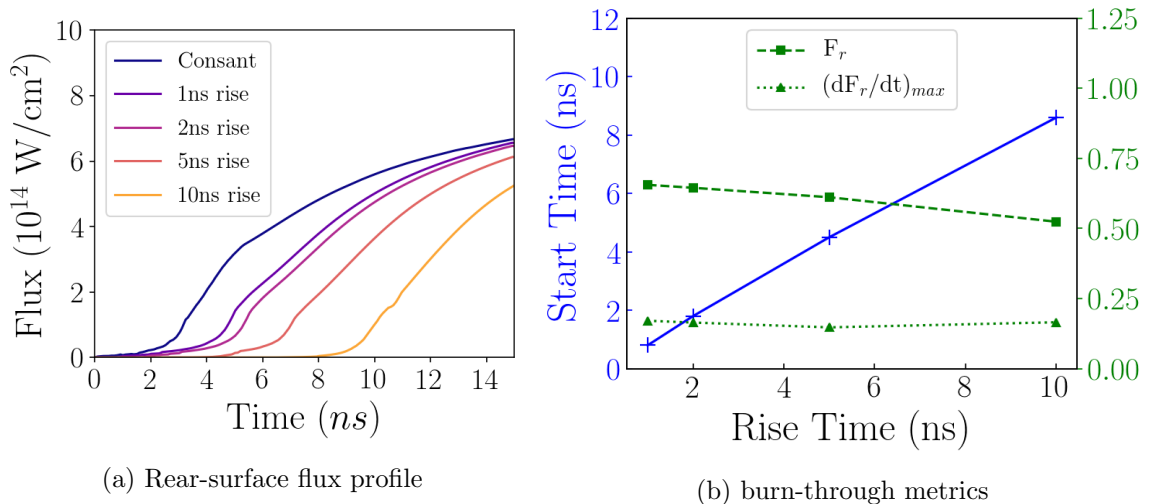


Figure 6.10: Plots showing the (a) rear-surface flux profiles and (b) burn-through metrics for a number of drive sources using a range of rise times up to 314 eV irradiating 800 μm of beryllium.

the target.

Beryllium exhibits a more interesting range of results. The rear-surface flux profiles for a 800 μm beryllium barrier are shown in figure 6.10. The results from the constant source show that immediately a significant amount of flux is emitted from the rear surface of the barrier. As explained earlier this is due to transonic behaviour of the radiation heat wave. However, for the rising sources, it can be seen that as the rise time is increased the immediate flux is significantly reduced. A sharp rise is seen at early times for the 1 ns and 2 ns source but more weakly in the 5 ns rise. Contrastingly, the 10 ns rise source has a sigmoid-like shape,

similar to that of the subsonic behaviour of the higher-Z materials. This is explained by the fact that, for a long duration, the drive temperatures in the 10 ns rise-time profile are under the $T_{R,critical}$ temperature for transonic behaviour for beryllium. The lower flux in the early stages results in a longer period of subsonic behaviour before the radiation front overtakes the shock front.

6.3 Complex Barrier Design

In the previous section, the barriers being simulated consisted of only one material. In the following section, the effect of layering the barrier with different materials is investigated. It is examined how a burn-through wave interacts when crossing the interface between two materials. The findings from that study are then used to aid the design of a barrier that could be applied to shock ignition. Additionally, a discussion is given on a few different ways in which burn-through barriers can be used in hohlraums.

6.3.1 Burn-through from Mid-Z to High-Z Material

The first set of simulations examined the transition of a burn-through wave from a mid-Z material to a high-Z material. The simulations used a 25 μm copper surface in front of 5 μm of gold. These thicknesses were chosen in order to produce a similar burn-through rise time and total burn-through flux to the 30 μm copper target from section 6.2.2. The rear-surface flux profile of the copper-gold target is shown in figure 6.11. Compared to the 30 μm copper only barrier, the rise is more gradual and doesn't appear to flatten off in the same way. This can be explained by looking at dynamics the shock front as it passes into the gold material. Figure 6.12 shows some snapshots of the density, pressure and radiation temperature profiles in the target taken at key points in time. As the initial shock front reaches the gold material it has a similar density (figure 6.12a). This results in a significant reflected shock in addition to the the transmission of the shock through the interface (figure 6.12b). The transmitted shock then reaches the rear surface of the barrier, the target begins to disassemble and a rarefaction wave propagates back into the target (figure 6.12c). The reflected shock maintains a region of high density which prevents the radiation front from reaching the rear surface.

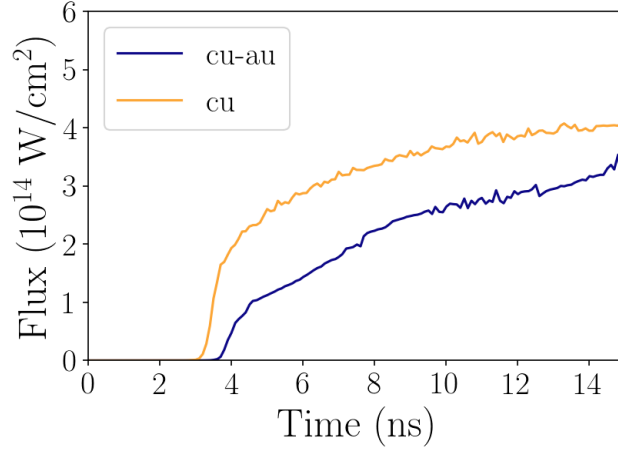


Figure 6.11: The rear-surface flux profile for a 25 μm copper, 5 μm gold burn-through barrier driven by a 314 eV source. The rear-surface flux profile from a previous simulation of 30 μm copper is shown for comparison.

Some time later the reflected wave dissipates and the continued drive onto the front of the target sets up a new, much weaker shock travelling forwards into the remaining gold plasma (figure 6.12d). This shock then breaks out of the plasma at 4 ns which triggers the rise of the rear-surface flux. The fact that this shock is weaker explains why the overall rise of the rear-surface flux is much slower than for a copper only target.

6.3.2 Burn-through from Mid-Z to Low-Z Material

The mid-Z to low-Z simulations used a 10 μm copper surface on the front of 130 μm of beryllium (SESAME #2020). Again, these thicknesses were chosen so that the burn-through would bare resemblance to the 30 μm copper target for comparison. The rear-surface flux profile is shown in figure 6.13. It can be seen that the burn-through start time and rate of rise are fairly similar but there is a larger amount of flux transmitted through the barrier. As with the copper-gold barrier simulations, this can be understood by examining the dynamics of the shock front across the material interface.

When the initial shock (figure 6.14a) reaches the material interface, the density of beryllium is much lower and so the shock is entirely transmitted (figure 6.14b) with no reflected shock. The transmitted shock in the beryllium has a lower peak density and continues to travel towards the rear surface of the barrier (figure 6.14c). At ~ 3 ns the shock breaks out triggering the target disassembly which causes the rapid rise in burn-through flux. This explains the

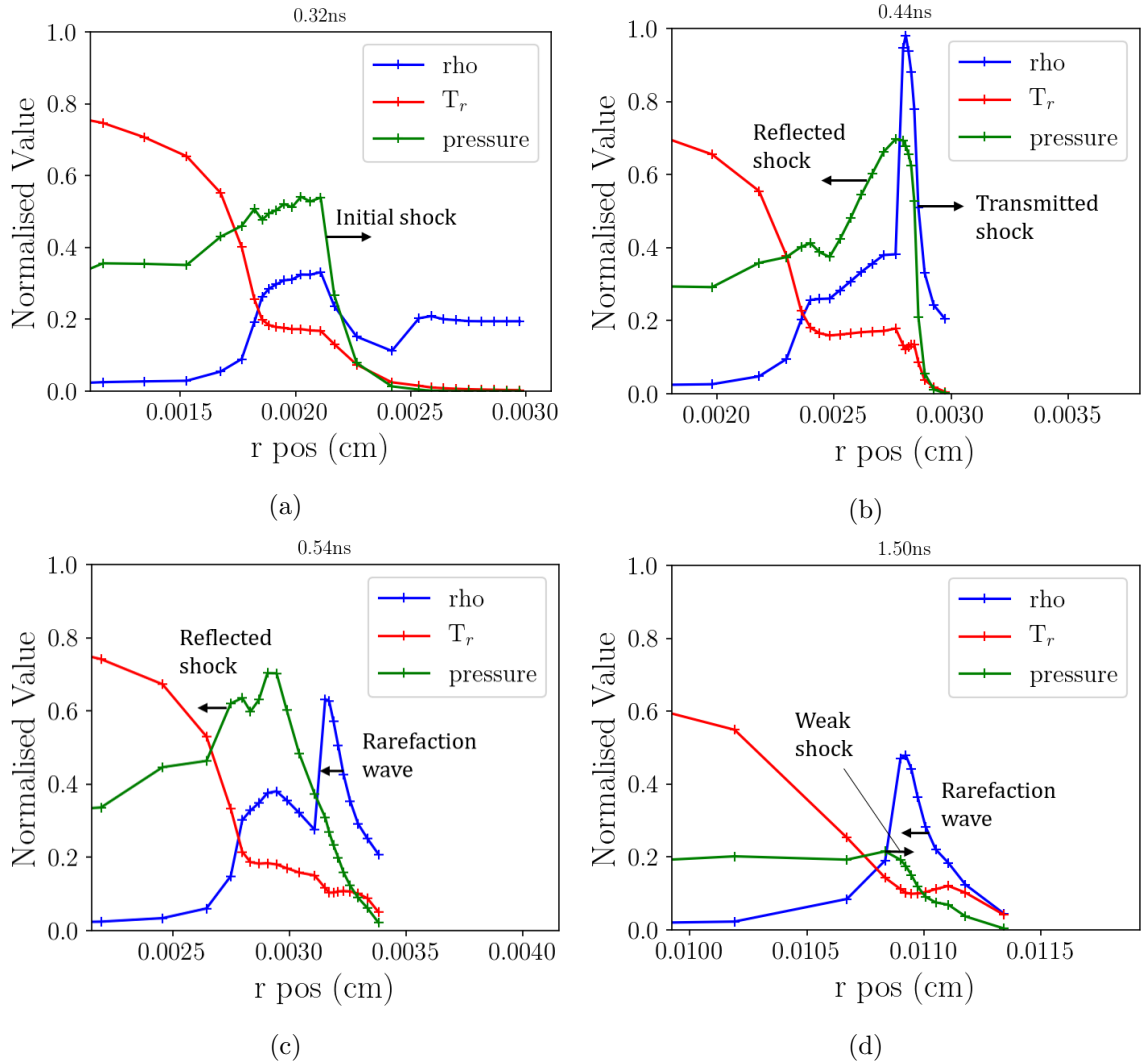


Figure 6.12: Snapshots of the density (blue), radiation temperature (red) and pressure (green) profiles in the copper-gold burn-through barrier. The time-step at which they were taken is shown at the top of the figure. They show how the shock built-up in the copper collides with the gold interface. (a) The initial shock approaching the gold interface. (b) The transmitted and reflected shocks produced at the interface. (c) The transmitted shock reaches the rear surface beginning a rarefaction wave as the reflected shock travels back into the barrier. (d) Final stage where a new weaker shock is set-up by the continued X-ray drive.

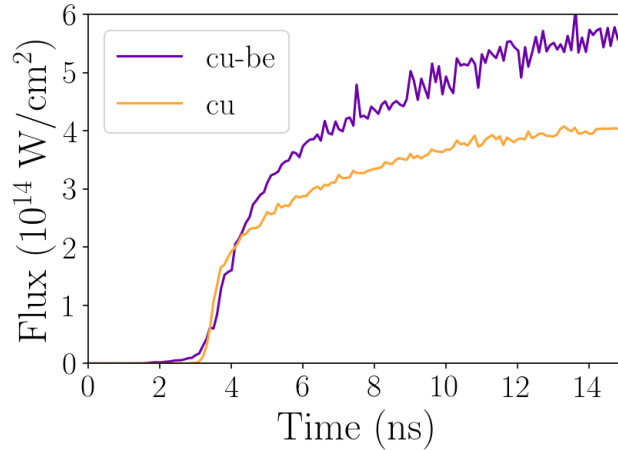


Figure 6.13: The rear-surface flux profile for a 20 μm copper, 130 μm beryllium burn-through barrier driven by a 314 eV source. The rear-surface flux profile from a previous simulation of 30 μm copper is shown for comparison.

similar shape of the burn-through flux profile to the single material simulations. However, the opacity of beryllium being lower than copper means that the total burn-through flux is higher than it would be for a pure copper target with a similar burn-through delay. It would not be possible to create the subsonic burn-through wave in a beryllium barrier because the 314 eV drive temperature is above the critical temperature for transonic behaviour. However, the copper on the front surface allows for subsonic ablation to occur. The resulting radiatively driven shock wave is then transmitted into the beryllium and continues to propagate subsonically up until the rear surface.

6.3.3 Delaying Burn-through

The mid-Z to low-Z barrier from the previous section is well suited to delay the onset of the burn-through without greatly reducing the total burn-through flux. The mid-Z material ablates subsonically allowing for a shock to build-up. The rear low-Z material then acts as a medium for this shock to propagate through. One can then delay the occurrence of the burn-through by increasing the thickness of the low-Z material. Then, due to the lower opacity of the low-Z material, the total burn-through flux doesn't significantly decrease. This is examined further through the comparison of a series of burn-throughs of copper-plastic barriers with those of pure copper barriers.

The simulations were run with the standard set-up, using the 314 eV source. The plastic

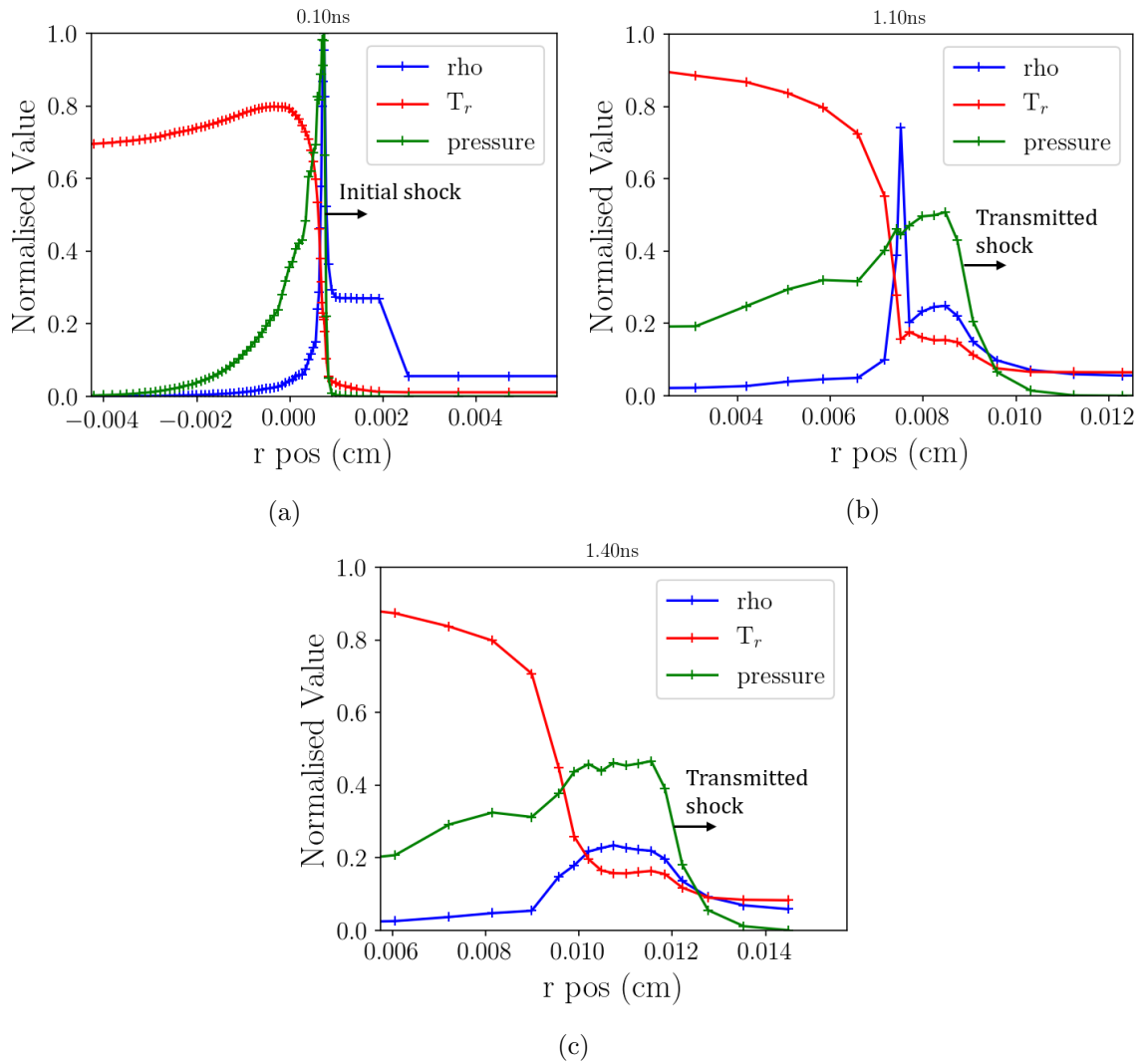


Figure 6.14: Snapshots of the density (blue), radiation temperature (red) and pressure (green) profiles in the copper-beryllium burn-through barrier. The time-step at which they were taken is shown at the top of the figure. (a) Initial shock approaching the copper-beryllium interface. (b) Shock transmitting into the beryllium. (c) Final shock travelling to the rear surface.

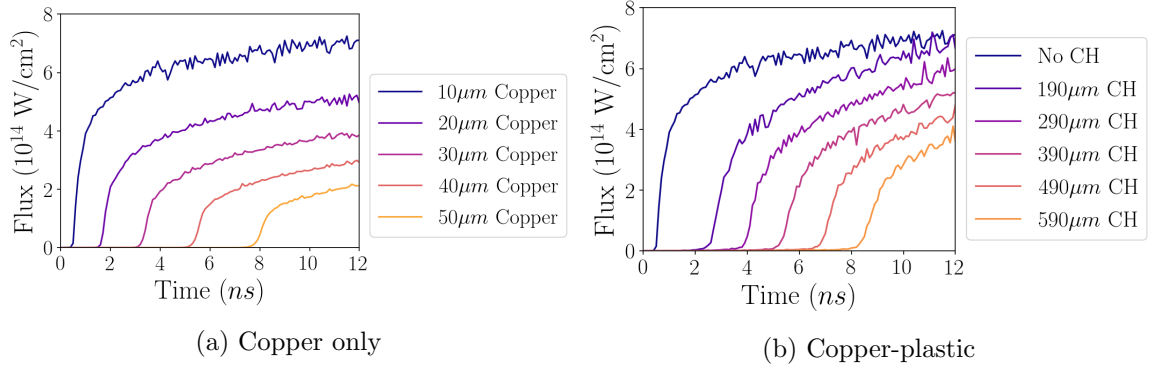


Figure 6.15: Graphs showing the rear-surface flux profiles of copper only and copper-plastic burn-through barriers. The drive source was a uniform Planckian X-ray drive at 314 eV. The profiles for a number of thicknesses of copper is shown on the left. The copper plastic barriers all had 10 μ m of copper on the front then different amounts of plastic (shown in the legend).

material used was polystyrene ($Z=3.5$, $A=6.51$) (SESAME #7592) at a solid density of 1.044 g cm $^{-3}$. Six barriers were simulated, each with 10 μ m of copper on the front surface and a different thickness of plastic 0 - 590 μ m. The results are compared to the varying thickness copper targets from section 6.2.3 in figure 6.15. In both barriers, the increasing thickness is delaying the onset of the burn-through rise. However, the fall off in total burn-through flux is significantly less for the copper-plastic barriers. The copper-plastic barriers demonstrate an effective way of delaying burn-through without greatly reducing the total flux through the barrier.

6.3.4 Burn-through Barrier Hohlraums

The previous sections gave an outline on how choices in burn-through barrier design can modify a constant X-ray source. The next stage in development is to think how one might use such barriers as drive sources in hohlraums. The most simple idea would be to mount a burn-through barrier source on the outer surface of the hohlraum. An external chamber could be heated to generate an X-ray radiation field. This would be separated from the internal hohlraum chamber (containing the payload) via a burn-through barrier. The burn-through barrier could then be designed to allow for the burn-through of radiation at a desired time. A schematic diagram of this idea is shown in figure 6.16. Hohlraums designed with multiple chambers have been proposed in previous studies^{85,140,149}. Here we propose that burn-through barriers can be placed in-between the internal chamber and external drive

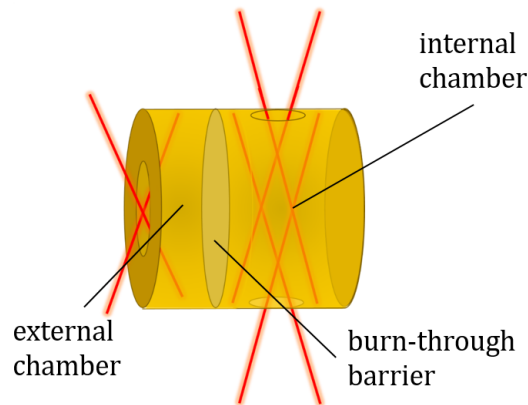


Figure 6.16: Schematic diagram of a hohlraum with an external burn-through chamber mounted on the outside. A burn-through barrier is placed between the external chamber and the main hohlraum to control the flow of X-rays into the hohlraum. The red lines represent laser drivers.

chambers in order to regulate the flow of X-rays onto the payload.

A more complex set-up may see a number of burn-through barrier sources mounted on the outer surface of a hohlraum. Each barrier could be designed to burn-through at different times creating a series of jumps in radiation intensity in the hohlraum interior. One could perhaps include some low-Z barriers that burn-through supersonically allowing for periods of more gradual rise. Such a hohlraum may be useful in a scenario in which there was no ability to change the temporal profile of a heating source. For example a laser system with limited pulse shaping capability. The available beams could be divided amongst a number of external burn-through barrier chambers. The X-ray profile in each external chamber would be the same but a complex temporally shaped X-ray field would be achieved in the interior through the use of a number of burn-through barriers with different burn-through properties. There is also the option to use more complex barrier designs. For instance one could use a single barrier that was pixelated into a number of different burn-through regions. Each region could be designed to burn-through at a different time. This way a constant drive source incident on the front surface would create a number of jumps in the total rear-surface flux. Alternatively one could design a similar barrier in which the different regions were designed to burn-through at the same time but with a varying amount of total burn-through flux. In that case, a spatially uniform source on the front surface could be modified to create a spatially shaped source at the rear surface. Such a barrier may be useful in controlling

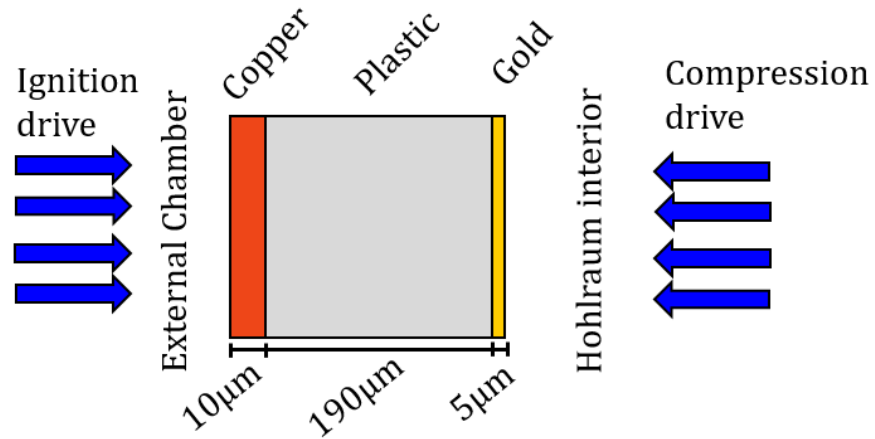
the spatial flux properties in a hohlraum interior. This idea is considered later on using 3D view-factor simulations.

This section is finished with a discussion on the validity of using a constant X-ray source in hohlraum burn-through barrier simulations.

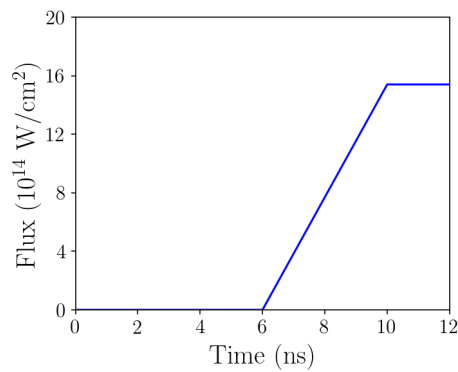
6.3.5 Shock Ignition Barrier

In this section, a burn-through barrier is designed that can be used to create a shock-ignition-like drive profile inside a hohlraum. In chapter 5 the drive requirements for an indirect-drive shock-ignition profile were investigated. It was shown that high laser drive powers may be required in order to increase the hohlraum temperature at a sufficient rate in order to launch the ignition shock. An alternative approach would be to use a burn-through barrier source to achieve a similar effect. Rather than using a fast rising, high power pulse, a more moderate laser driver could be used to gradually heat an external chamber to the desired temperature. The rapid rise in X-ray drive required to launch the ignition shock would occur when the radiation wave burns through into the internal chamber. In such a barrier, two radiation waves would be present. One from the drive building up in the external chamber and one from the drive in the internal hohlraum chamber. 1D HYADES simulations were carried out to investigate the dynamics of colliding burn-through waves.

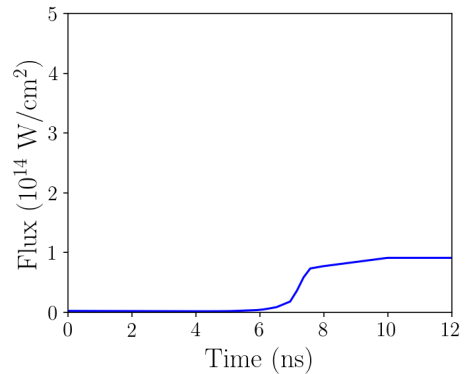
The X-ray profile used in the 1D shock-ignition-like pressure simulations from chapter 5, section 5.2.3 was used as a target. The aim is to design a barrier that on one side reflects the radiation from the internal chamber and on the other side allows a burn-through wave to build up that will eventually reach the inner chamber and quickly raise the drive temperature. Figure 6.17 shows the final design of the barrier and the X-ray sources used. The LHS represents the side which the external burn-through source will be on and the RHS will have the hohlraum interior. The RHS will be irradiated with a source that represents the compression portion of the shock ignition pulse. For this the X-ray flux profile from the 1D simulations in chapter 5, section 5.2.3 can be used. On the LHS will be an X-ray source chosen so that the burn-through into the internal chamber will occur at the right time, supplying the ignition part of the pulse. The burn-through source used rises linearly from 0 at 6 ns up to $1.54 \times 10^{15} \text{ W cm}^{-2}$ (350 eV) at 10 ns. Note that this source is just used



(a) Schematic of the shock ignition barrier design.



(b) Ignition drive



(c) Compression drive

Figure 6.17: Set-up of the shock-ignition burn-through barrier simulation. (a) A schematic diagram of the barrier design. The concept behind the barrier is that the X-rays from the source on the LHS will burn-through the barrier at 10 ns rapidly increasing the flux escaping on the RHS. The drive profiles used in the simulations are shown in the bottom plots. (b) Ignition profile that rises from 0 at 6 ns to $1.54 \times 10^{15} \text{ W cm}^{-2}$ at 10 ns. (c) The compression portion of the drive pulse used in chapter 5, see figure 5.3.

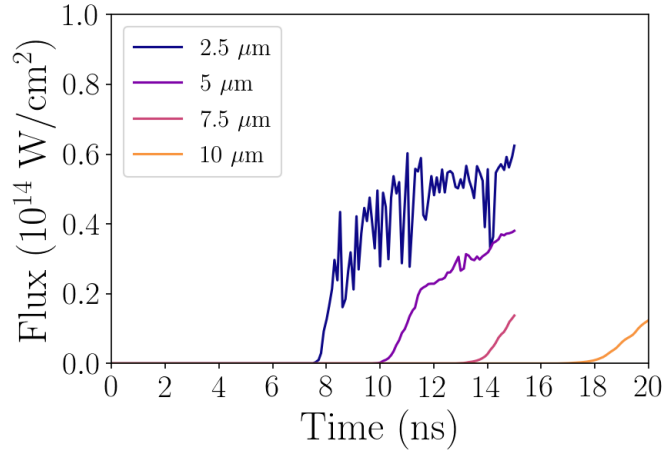


Figure 6.18: The rear flux profiles of gold barriers of different thicknesses. The drive source used in the simulations was the shock ignition compression pulse from figure 6.17c. The simulations were run for 15 ns with the exception of the 10 μm thick barrier where the simulation length was increased to 20 ns so the burn-through rise could be observed.

as an example of a slowly rising X-ray source that could be created in an external chamber. One can crudely estimate the drive power that might be required to create such a source using scaling laws that were laid out in chapter 5. The radiation temperature in a hohlraum scales as $T_R^{3.3} \propto \frac{P}{A} t^{1/2}$, where P is the drive power, A is the surface area of the hohlraum and t is time. Simulations in chapter 5 showed that a 400 TW pulse generated 290 eV in 1 ns in a 1.62 cm² area hohlraum (section 5.3.1). Let's assume an external chamber would have half the surface area. Then, using the scaling law, achieving 350 eV in 4 ns would require a considerably lower drive power of 190 TW. This is only a rough estimate but it demonstrates the possible benefits of using an external burn-through source.

The aim now is to design the barrier so that the burn-through of the external source occurs at around 10 ns suddenly increasing the internal temperature of the hohlraum. In the barrier, there will be two burn-through waves present. The burn-through wave from the compression pulse burning into the gold from the hohlraum interior and the wave from the ignition pulse burning through the copper-plastic barrier. The barrier should be designed so that the two radiation waves will burn-through at 10 ns. A number of simulations were run for gold targets with thicknesses 2.5 μm , 5 μm , 7.5 μm and 10 μm . The temperature of the drive source used is shown in figure 6.17c. The rear resulting rear-surface flux profiles are shown in figure 6.18. The 5 μm gold delays the burn-through for the desired 10 ns.

A similar set of simulations were carried out for the external source burning through the

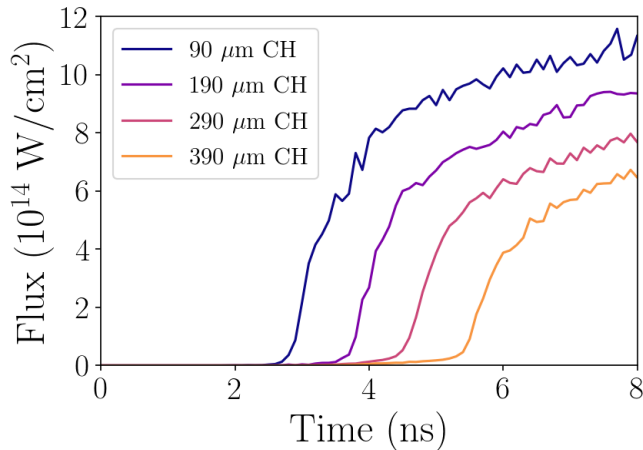


Figure 6.19: A plot of the rear-surface flux profile for copper-plastic barriers of different thickness that were irradiated with the ignition pulse from figure 6.17b. In all the barriers, the thickness of copper was 10 μm , the thickness of the plastic is then shown in the legend.

plastic-copper barrier. A barrier design is required that will burn through 4 ns after the rise begins. Three copper-plastic barriers were simulated with 10 μm of copper and then 90 μm , 190 μm and 290 μm of plastic. The rear-surface flux profiles are shown in figure 6.19 The 190 μm thickness plastic barrier delays the burn-through to close to 4 ns as needed.

The copper-plastic and gold barriers can now be combined into one simulation to model a shock ignition-like burn-through source. A simulation was run in HYADES using a barrier made up of 10 μm of copper, 190 μm of plastic and 5 μm of gold. The mesh was structured in order to maintain spatial resolution and keep similar masses in adjacent mesh regions. The copper region consisted of 71 mesh lines with a feather ratio of 1.1. With a surface area of 1 cm^2 this resulted in a mass value of 0.8 mg in the last region. The plastic region then had 29 mesh lines equally spaced giving a mass value of 0.7 mg in each region. Then finally gold used 64 mesh lines with a feather ratio of 0.9 making the mass in the first region 1.0 mg. The sources used are shown in figure 6.17. The flux into the hohlraum was then taken to be the boundary flux at the RHS.

Figure 6.20 shows the RHS boundary flux from the simulation as a dashed blue line. It can be seen that the rise in the ignition spike occurs before 10 ns and is not as fast as it needs to be. This slow rise can be attributed to the collision of the two counter-propagating burn-through waves in the barrier. After the shock fronts collide they create a region of high density and pressure that results in a slower disassembly of the barrier. This is similar to the

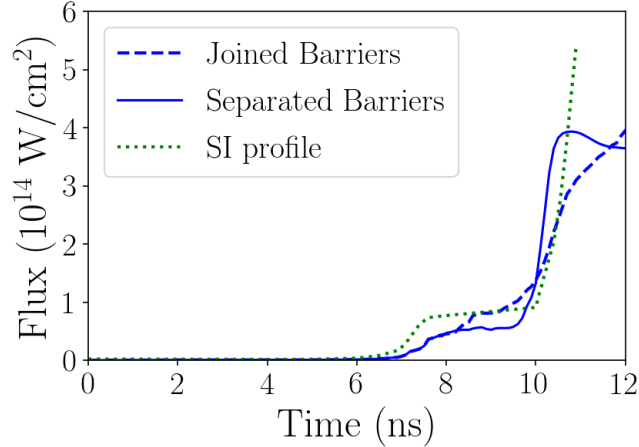


Figure 6.20: Results of the RHS flux from the 1D shock-ignition burn-through barrier simulations that was described and shown in figure 6.19. The shock ignition X-ray drive profile from chapter 5, section 5.2.3 is shown for reference as a green dotted line.

situation described in the mid-Z to high-Z target in section 6.3.2. This can be avoided by separating the barriers with a low-density gas region so they are not in direct contact with each other. In the simulation, this was modelled by placing a 1 mm region of helium gas at 0.1 mg cm^{-3} between the copper-plastic and gold barriers. When the barriers are separated the shock fronts can't collide and the two barrier disassemble independently. In figure 6.20 the rear-surface flux profiles of the joined and separated barriers are compared to the original shock-ignition-like drive profile that was used in the 1D simulations in chapter 5. It is clear that the flux separated barrier is much closer to the shape of the desired shock ignition profile. However, the flux is consistently less than the shock ignition-like profile. This is to be expected as only one surface of the hohlraum is being modelled. In reality the radiation escaping the RHS of the simulation would be contained in a hohlraum. We would therefore expect the hohlraum temperature to be slightly higher. The ignition spike rise time in the separated barrier is sufficiently rapid.

It is worth discussing the choices made behind the sources used in the shock ignition barrier simulation. The sources used are not based on experimental or numerical results but represent the values of flux and rise times that are easily achievable inside hohlraums. The point of using these sources was to show how one might use burn-through barriers to modify X-ray sources as desired. Shock ignition was being used as an example but is just one of the possible applications of burn-through barriers. In the next section it is examined how

burn-through barriers can spatially shape X-ray sources.

6.4 Spatially Shaped Burn-through Sources

Up until now, burn-through barriers have only been used to control the temporal properties of the X-ray drive. In section 6.3.4 the idea of a pixelated burn-through barrier with a number of different burn-through regions was suggested as a way of spatially modulating a uniform X-ray source. That concept is looked at in more detail in this section. First, a discussion is given on how such a barrier can be designed using a number of 1D HYADES simulations. Then, the F3D view-factor code is used to study the effect of a spatially shaped pulse inside hohlruams.

6.4.1 Spatially Shaped Barrier Design

A spatially shaping barrier can be designed using the idea of pixelated burn-through barrier made up of a number of layered barrier regions. The spatial shaping is achieved by using a varying ratio of copper:plastic thickness across the barrier. The parts of the barrier with a higher amount of copper will have a lower total burn-through flux due to the higher opacity of copper. The thickness of the plastic can then be chosen in order to synchronise the times of the burn-through across the barrier. A schematic diagram of such a barrier can be seen in figure 6.21. The compositions of the different regions were designed using 1D HYADES simulations. Each barrier was modelled independently.

Five barriers were simulated with different copper:plastic ratios. The simulations used the same HYADES set-up as in the copper-plastic simulations in section 6.3.3 and the usual 314 eV X-ray source. Each barrier began with a different thickness of copper ranging from 10 μm to 50 μm . Multiple simulations were then run with varying thicknesses of plastic. The plastic thickness was increased/decreased until a burn-through delay of 7 ns was achieved. The final thicknesses in each of the five barrier designs were 10 μm :500 μm , 20 μm :320 μm , 30 μm :205 μm , 40 μm :115 μm ., and 50 μm :35 μm . The rear-surface flux profiles from all the simulations of those barriers are shown in figure 6.22.

The different barriers all begin the burn-through rise at the same time but end with different

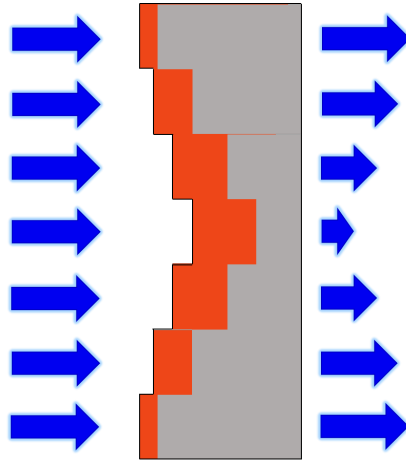


Figure 6.21: A schematic diagram of how a pixelated barrier could be used to create a spatially shaped X-ray source. Each region has a different ratio of copper to plastic and therefore has a different level of burn-through flux. If the plastic thickness is tailored so that the burn-throughs occur simultaneously across the barrier the result is one burst of spatially shaped X-rays.

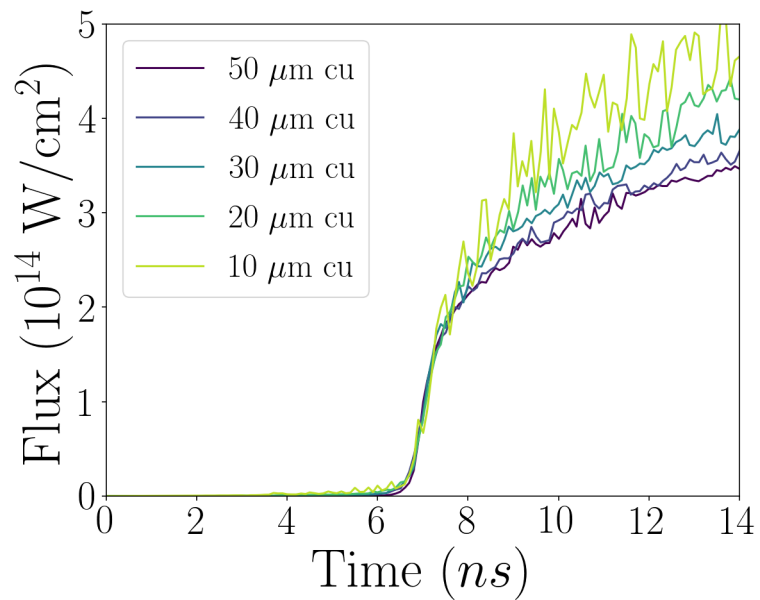


Figure 6.22: The rear-surface flux profiles from a number of different copper-plastic barriers driven with a 314 eV X-ray source. The thickness of the copper in each barrier is shown in the legend, the thickness of the plastic was chosen so that the burn-through would occur at 7 ns.

total burn-through fluxes. It would be possible to create a burn-through barrier combining these barrier designs. The result would be a single burst of spatially shaped X-ray flux out of the rear surface. This sort of barrier could be used to control the spatial and temporal properties of an X-ray source simultaneously. However, such a barrier would introduce additional concerns. The adjacent regions of different density and potential for shear flows give rise to instability growth within the barrier. In particular, the Richtmyer-Meshkov instability¹⁵⁰ can seed growth for the Rayleigh-Taylor instability¹⁵¹ at interfaces of discontinuous density. These instabilities would cause mixing of the copper and plastic regions. Such fluid effects have been shown to be important in laser driven burn-through experiments^{133,152}. As h2d is not well suited to modelling these effects they are not considered any further.

Now that a barrier has been designed, the effects of a spatially shaped source on hohlraum radiation fields can be examined. The following sections describe 3D view-factor simulations investigating the effect of spatially varying barriers on hohlraum radiation fields.

6.4.2 Simulation Set-up

The code F3D was used for the simulations investigating the 3D X-ray field created in a hohlraum by a spatially shaped burn-through source. F3D was described in detail in section 3.2. The hohlraum was represented in 3D as a cylindrical surface. To represent the burn-through source, an emitting surface with an albedo of 0 (meaning it reflects none of the radiation incident on it) was placed at each end of the hohlraum. Realistically the albedo of the burn-through barrier surface would be non-zero but the radiation reflected back into the hohlraum interior would be significantly less than the radiation burning through from the other side of the barrier. Therefore, the reflected radiation would have a minimal effect on the symmetry of the X-ray field in the hohlraum. For this reason, the albedo of the barrier is neglected. The remaining inner surface of the cylinder was given an albedo of 0.9, which is a reasonable approximation for a high-temperature gold hohlraum¹⁵³. A spherical surface with albedo of 0 was used to represent a capsule payload in the centre of the hohlraum. Again, an albedo of 0 is not accurate as there would be some amount of radiation reflected from the capsule surface. However, the albedo of the outer capsule surface is much less than the albedo of the hohlraum walls (ICF outer surface ablaters are specifically chosen for their

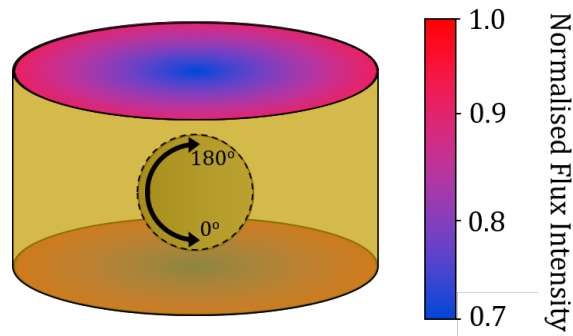


Figure 6.23: A schematic diagram of the 3D view-factor simulations. As an example the 30% linearly varying source described in section 6.4.3 is shown. The hohlraum (10 mm radius, 15 mm length) has a burn-through barrier source placed at either end. The sources vary from 70% to 100% along the radius of the disc. A spherical capsule (radius 2.5 mm) surface is shown in the centre. The angles shown are used later to describe the spatial flux profile across the capsule.

low albedos as this leads to more efficient ablation). So it is assumed that the capsule absorbs all incident radiation and the albedo is set to 0. The next section describes the results for a number of different spatially shaped burn-through barrier sources.

6.4.3 Spatially Varying Drive Barriers

The initial simulations used a hohlraum with dimensions of 10 mm radius and 15 mm length. The spherical payload surface had a radius of 2.5 mm and was placed in the centre of the hohlraum. A schematic diagram of one of the simulations is shown in figure 6.23. A number of different burn-through sources were trialled at both ends of the hohlraum. The first was a spatially uniform 250 eV source. Then, four sources that varied linearly along the radius of the source. The total variations were 10%, 20%, 30% and 40% from minimum to maximum with the peak flux being emitted at the outer radius of the source. Two non-linearly varying sources used a quadratic and fifth order power ($F(r) = F_0 r^5$) variation with radius and had a 40% variation from minimum to maximum. All the varying sources were normalised in order to make sure the total flux emitted would be the same as for the 250 eV uniform source. The resulting drive profiles on the capsule are shown in figure 6.24 as a function of angle. To begin with it can be seen that, for the uniform drive source, there is a significant 11% variation over the capsule surface. The 90° point represents the capsule equator which is the part of the capsule surface that is furthest from the burn-through source. This is the origin of the asymmetry as the drive will be strongest from the burn-through part of the hohlraum.

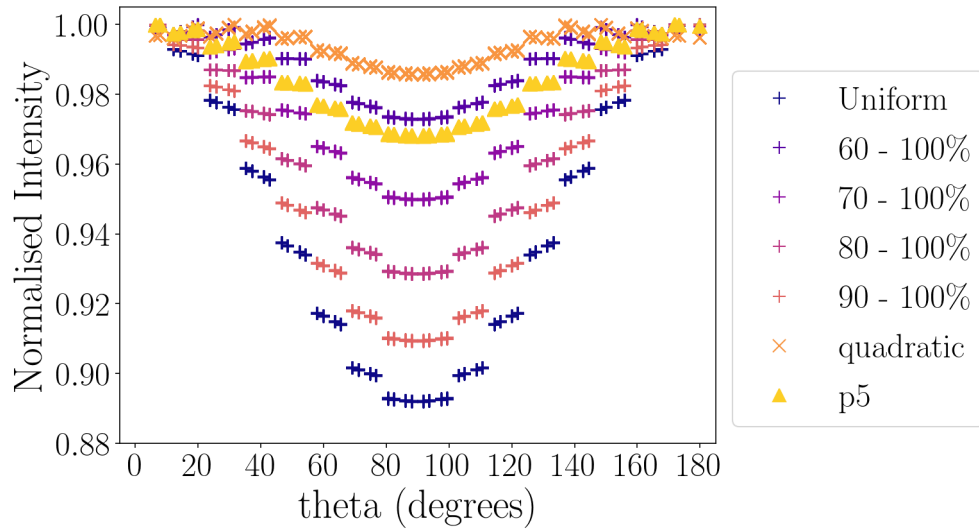


Figure 6.24: The angular flux profile across a capsule produced in 3D view-factor simulations for a number of spatially varying hohlraum burn-through sources. A schematic diagram of the simulation was given along with the definition of the angles on the x-axis in figure 6.23.

This asymmetry can be counteracted by shifting more flux to the outer radius of the source surface. The equator of the capsule will see more of the source flux and the radiation profile will be evened out. In this way, the sources with 40% variation in flux along the surface act to flatten the X-ray flux profile across the capsule. The quadratically varying source flattens the profile even further to the point where the difference in flux across the whole capsule is less than 1.5%.

The effect of this radiation profile flattening is highly dependent on the geometry of the hohlraum. If the hohlraum were longer and narrower the capsule poles would see little of the burn-through source surface. So the effect of pushing more flux to the outer radius is reduced. The simulation was run again with such a hohlraum that had a radius of 2.55 mm and length of 8.2 mm. Shown in figure 6.25 are the angular drive profiles on the capsule for a uniform source and linearly and quadratically varying sources with a 40% variation. It is clear that the effect of profile flattening is greatly reduced.

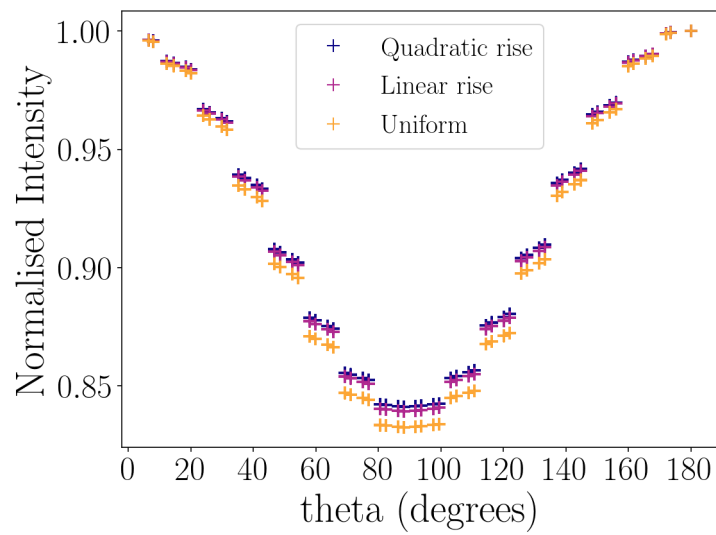


Figure 6.25: Angular flux drive profiles in 3D view-factor simulations in a narrower hohlraum geometry. Shown are the flux profiles produced by a uniform source and sources that varied by 40% linearly and quadratically.

Chapter 7

Conclusions

7.1 Conclusions

7.1.1 Soft X-ray Ablation Pressure Scaling

In chapter 4, the ablation pressure scaling of materials driven by soft X-rays was investigated. The interaction of soft X-rays is important in a number of areas in the field of HEDP. In the literature, ablation pressure studies have tended to focus on low- Z materials relevant to ICF. Work on materials of a higher atomic number ($Z > 6$) have been more concerned with equation of state, opacity and radiation transport. The aim of the work in chapter 4 was to fill the gap in the literature by surveying the properties of soft X-ray driven ablation in materials with atomic numbers up to $Z = 22$.

More than six hundred HYADES simulations were run, investigating the ablation pressure in seven materials over the temperature range 100 eV to 400 eV. The temperature value at which the material began ablating transonically $T_{R,critical}$, was found for each material. In general, $T_{R,critical}$ increased with atomic number. Power laws for the scaling of ablation pressure with temperature and time were also found. As expected from the theory, the temperature scalings weakened for materials of high atomic number. The results from this study were in agreement with the literature that, in the range of 100 eV - 300 eV beryllium is the highest performing ablator.

In this study it was found that an atomic shell effect was reducing the ablation pressure in titanium. To the authors knowledge, such an effect has not been described before in the

literature. It was proposed that this is caused by a significant increase in the ionisation energy once an atomic shell has been fully stripped of electrons. The presence of the atomic shell effect was confirmed when it disappeared in simulations that used a Thomas-Fermi ionisation model.

7.1.2 Producing Shock-Ignition-Like Pressures Using Indirect Drive

The work in chapter 5 was concerned with the laser drive parameters that would be required to achieve shock-ignition-like pressures using indirect drive. Present studies in the field of shock ignition have only considered a direct drive approach. This study began the development of an indirect drive approach with the motivation of fielding ignition-scale experiments without having to modify current facilities.

Starting from a working direct drive shock ignition study, steady-state ablation scaling laws were used to make a prediction for an X-ray drive profile that could achieve shock-ignition-like pressures in a beryllium ablator. 1D radiation hydrodynamics simulations confirmed that the X-ray drive pressures matched the pressures from the laser drive profile. From there, 2D simulations were carried out, which found the laser drive parameters that could produce the required X-ray drive inside a hohlraum. It was shown that a ~ 250 Mbar igniter shock could be produced by indirect drive with a laser drive pulse that peaked at 400 TW. This is within the range of what is currently achievable at the NIF.

The study finished with a number of comparisons to similar indirect drive studies and experiments. The ablation pressures observed in this work matched experimental observations of ablation rates in the range of X-ray drive temperatures between 160 eV - 240 eV. A comparison was made to an experimental study that saw similarly fast rises in hohlraum temperature in vacuum hohlraums. However, there are a couple of concerns that higher laser drive powers than the predicted 400 TW may be required. The first concern is that high levels of laser plasma interactions such as SRS and SBS in gas-filled hohlraums may negatively impact the conversion of laser to X-ray energy. In addition, these effects create suprathermal electrons which can go on to cause pre-heat in the capsule. The case is regularly made in direct drive shock ignition that, if these electrons are not too energetic and the shell sufficiently dense, they could enhance shock pressures; a similar case could perhaps be made for indirect

drive shock ignition. The second concern is that significant shell acceleration in the capsule compression could cause the pressure scaling to drop. The effect of both laser plasma interactions and reduced ablation pressure under shell acceleration could push the required laser drive power beyond the capabilities of the NIF. Adequate assessment of these would require knowledge of the capsule and X-ray pulse design of a indirect-drive shock-ignition target.

7.1.3 Hohlräum Burn-through Barriers

Chapter 6 presented a new technique for controlling X-ray flux inside hohlraums using burn-through barriers. This is considerably different to the current approach where the hohlraum X-rays are predominantly controlled via the external driver. Hohlräum burn-through barriers offer a number of potential benefits. In particular it is suggested for Z-pinch driven hohlraums, which are capable of producing intense X-ray sources but are limited in their ability to control the spatial and temporal aspects of the X-rays.

A number of 1D radiation hydrodynamics simulations were used to investigate the burn-through of a uniform 314 eV source through a barrier and into an adjacent hohlraum chamber. It was shown how the spatial and temporal properties of a source can be controlled through choice of material and barrier thickness. A multi-layered, copper-plastic barrier was used to delay X-ray burn-through. The plastic thickness could be increased, delaying the burn-through without significantly reducing the total X-ray flux through the barrier.

Several suggestions were made on how to employ burn-through sources in hohlraums. External chambers could be mounted onto a hohlraum each separated from the internal chamber by a burn-through barrier. A number of different barrier designs could then be used to create a series of jumps in the X-ray intensity in the internal chamber. Alternatively, a more sophisticated, pixelated barrier design could be used in which there are multiple different burn-through regions. Each region would burn-through at a different time, again resulting in a series of jumps in X-ray intensity. It was also shown how a pixelated barrier could be used to create a spatially shaped source. A number of 1D simulations showed that, by changing the copper:plastic ratio, one could synchronise burn-throughs with a different X-ray intensity spread across the barrier. Then the effects of using such a spatially shaped barrier in a hohlraum were investigated. 3D view-factor simulations were run examining how differ-

ent burn-through sources mapped onto spherical payloads inside hohlraums. It was found that, by varying the intensity of the X-rays along the radius of the burn-through source, the symmetry of the irradiation of the payload could be controlled. This was however, highly dependent on the hohlraum geometry.

7.2 Further Work

This final section suggests a number of avenues for further work on the topics investigated in this thesis.

Perhaps the most interesting discovery from the work in chapter 4 was the drop in ablation pressure scaling due to an atomic shell effect in mid-Z plasmas. To the author's knowledge this effect has never been observed before in the literature. The work in this thesis consolidated the evidence and confirmed the presence of a shell effect but did not seek to provide a complete picture behind the physical reason for the pressure fall off. This would require the development of a new theoretical ablation pressure scaling model and would be a good basis for further study.

The work in chapter 5 demonstrated that hohlraum temperature rise times may actually be sufficient in NIF-scale hohlraums to undertake shock ignition experiments. However, the study's use of a beryllium ablator will change the dynamics of the implosion. The next logical step in this work would be to design a new shock ignition capsule with a beryllium ablator and corresponding X-ray drive profile. This would also aid in understanding what the conditions in the hohlraum are likely to be and thus, the level of parametric instabilities one should expect. Recent studies in ICF target design have used data-driven techniques, which is an emerging area of interest in the field of HEDP [154–156](#). A data-driven indirect-drive shock-ignition study could yield useful insights both from a data science and ICF perspective.

The burn-through barrier study in chapter 6 has a few areas of further research worth pursuing. In the present study, the simulations were limited to 1D but there are a number of 2D fluid instability effects that would need to be investigated. Additionally, it would be interesting to begin designing specific applications of hohlraum burn-through barriers (e.g. a

capsule implosion driven by a Z-pinch source in a burn-through barrier hohlraum). Finally, it would be valuable to begin hohlraum burn-through barrier experiments to confirm the observations made in the simulations. Such a study has been accepted for time on the Orion laser at AWE and is in the planning stage at the time of submission of this thesis.

Chapter 8

Appendices

8.1 Appendix A: Derivation of Diffusion Equation

This appendix outlines the derivation of the diffusion equation from the radiative transfer equation. The derivation largely follows the treatment from reference 30. Let's start by stating the radiative transfer equation from section 2.4.1

$$\frac{1}{c} \frac{\partial I_\nu}{\partial t} + \mathbf{n} \cdot \nabla I_\nu = j_\nu - k_a I_\nu + \sigma_{\text{scatter}}, \quad (8.1)$$

The first step is to approximate the angular dependence on the specific intensity $I_\nu(\mathbf{r}, \mathbf{n}, t)$, with a spherical harmonic expansion. The expansion is a linear combination of the Laplace spherical harmonics given by

$$f(\theta, \varphi) = \sum_{l=0}^{\infty} \sum_{m=-l}^l f_l^m Y_l^m(\theta, \varphi), \quad (8.2)$$

where Y_l^m are the corresponding spherical harmonics and f_l^m are the expansion coefficients given by the integral over all solid angle

$$f_l^m = \int_{\Omega} f(\theta, \varphi) Y_l^{m*}(\theta, \varphi) d\Omega, \quad (8.3)$$

the Y_l^{m*} denotes the complex conjugate and Ω is the solid angle. We now need to apply this expansion to the specific intensity. It is assumed that the radiation field is nearly isotropic,

so we can limit to the $l = 0$ and $l = 1$ terms. Using the standard spherical harmonics and equation 8.3 $l = 0$ terms are

$$Y_0^0(\theta, \varphi) = \frac{1}{2} \sqrt{\frac{1}{\pi}}, \quad (8.4)$$

$$f_0^0 = \int_{\Omega} I_{\nu}(\mathbf{r}, \mathbf{n}, t) \frac{1}{2} \sqrt{\frac{1}{\pi}} d\Omega. \quad (8.5)$$

Similarly, the $l = 1$ terms are

$$Y_1^{-1}(\theta, \varphi) = \frac{1}{2} \sqrt{\frac{3}{2\pi}} \cdot e^{-i\varphi} \cdot \sin(\theta) \quad (8.6)$$

$$f_1^{-1} = \int_{\Omega} I_{\nu}(\mathbf{r}, \mathbf{n}, t) \frac{1}{2} \sqrt{\frac{3}{2\pi}} \cdot e^{i\varphi} \cdot \sin(\theta) d\Omega \quad (8.7)$$

$$Y_1^0(\theta, \varphi) = \frac{1}{2} \sqrt{\frac{3}{\pi}} \cdot \cos(\theta) \quad (8.8)$$

$$f_1^0 = \int_{\Omega} I_{\nu}(\mathbf{r}, \mathbf{n}, t) \frac{1}{2} \sqrt{\frac{3}{\pi}} \cdot \cos(\theta) d\Omega \quad (8.9)$$

$$Y_1^1(\theta, \varphi) = -\frac{1}{2} \sqrt{\frac{3}{2\pi}} \cdot e^{i\varphi} \cdot \sin(\theta) \quad (8.10)$$

$$f_1^1 = -\int_{\Omega} I_{\nu}(\mathbf{r}, \mathbf{n}, t) \frac{1}{2} \sqrt{\frac{3}{2\pi}} \cdot e^{-i\varphi} \cdot \sin(\theta) d\Omega. \quad (8.11)$$

Using equations 8.4-8.11 we can now express the expansion in a more simple form

$$I_{\nu}(\mathbf{r}, \mathbf{n}, t) = \frac{1}{4\pi} I_{\nu}^{(0)}(\mathbf{r}, t) + \frac{3}{4\pi} \mathbf{n} \cdot \mathbf{I}_{\nu}^{(1)}(\mathbf{r}, t). \quad (8.12)$$

where the expansion coefficients are given by

$$I_{\nu}^{(0)}(\mathbf{r}, t) = \int_{\Omega} I_{\nu}(\mathbf{n}, \mathbf{r}, t) d\Omega. \quad (8.13)$$

$$\mathbf{I}_{\nu}^{(1)}(\mathbf{r}, t) = \int_{\Omega} \mathbf{n} I_{\nu}(\mathbf{n}, \mathbf{r}, t) d\Omega. \quad (8.14)$$

We can now integrate equation 8.1 over all directions and substitute in 8.13 and 8.14; for simplicity it will be assumed that the scattering term is described by the product of the

specific intensity and some scattering coefficient, $\sigma_{\text{scatter}} = -k_s I_\nu(\mathbf{n})$, which will give

$$\frac{1}{c} \frac{\partial I_\nu^{(0)}(\mathbf{r}, t)}{\partial t} + \nabla \cdot \mathbf{I}_\nu^{(1)}(\mathbf{r}, t) = 4\pi j_\nu - k_a I_\nu^{(0)}(\mathbf{r}, t) - k_s I_\nu^{(0)}(\mathbf{r}, t). \quad (8.15)$$

In a similar way multiplying 8.1 by \mathbf{n} and integrating over all directions gives

$$\frac{1}{c} \frac{\partial \mathbf{I}_\nu^{(1)}(\mathbf{r}, t)}{\partial t} + \frac{1}{3} \nabla I_\nu^{(0)}(\mathbf{r}, t) = -(k_a + k_s) \mathbf{I}_\nu^{(1)}(\mathbf{r}, t) \quad (8.16)$$

At this point we now impose the assumption of diffusive behaviour. For diffusive behaviour to be valid, equation 8.16 must satisfy Fick's law which states that diffusive flux must be proportional to the concentration gradient, or in this case $\mathbf{I}_\nu^{(1)}(\mathbf{r}, t) = -D(\nu) \nabla I_\nu^{(0)}(\mathbf{r}, t)$ where $D(\nu)$ is some diffusion coefficient. For this to be true, the time derivative term in 8.16 must be zero. That now gives an equation that relates $I_\nu^{(0)}(\mathbf{r}, t)$ and $\mathbf{I}_\nu^{(1)}(\mathbf{r}, t)$ which we can use to re-express the radiative transfer equation in terms of only $I_\nu^{(0)}(\mathbf{r}, t)$:

$$\frac{1}{c} \frac{\partial I_\nu^{(0)}(\mathbf{r}, t)}{\partial t} - \nabla \cdot D(\nu) \nabla I_\nu^{(0)}(\mathbf{r}, t) = 4\pi j_\nu - (k_a + k_s) I_\nu^{(0)}(\mathbf{r}, t). \quad (8.17)$$

where the diffusion coefficient is given by $D(\nu) = 1/3(k_a + k_s)$. Equation 8.17 is known as the diffusion equation.

8.2 Appendix B: Technique for Extracting Rear-Surface Flux from HYADES

This appendix describes the technique used to extract the total X-ray flux transmitted through a material in a 1D planar HYADES simulation. In the geometry being used in the burn-through barrier simulations, the burn-through wave is propagating from left to right. The total transmission of X-rays through the barrier will be given by the boundary emission at the RHS of the simulation. This was taken from the right hand boundary emission flux variable in HYADES called QRADGR. Note that an equivalent QRADGL variable exists for emission at the left hand boundary which would give a measure of the radiation reflected from the front surface. The QRADGR and QRADGL terms are outputs of the multi-group

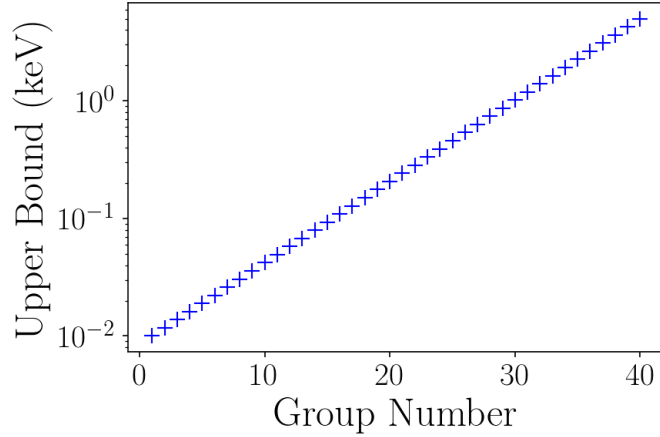


Figure 8.1: A plot of the photon spectral group structure used in the HYADES simulation of a 314 eV Planckian source transmitting through low density of hydrogen. The upper bounds of the groups are plotted against the group number

radiation transport package in HYADES. In multi-group radiation transport the photons are binned into a number of spectral groups, the structure of which is defined by the user. The QRADGR output gives the intensity of X-ray emission of each spectral group per unit spectral energy and thus has units of $\text{erg cm}^{-2} \text{s}^{-1} \text{keV}^{-1}$. The intensity of the boundary emission from a specific spectral group can be retrieved by multiplying the QRADGR term by the spectral width of the group. The total boundary emission F_{tot} , is then given by

$$F_{\text{tot}} = \sum_{i=1}^n \text{QRADGR}_i \times (E_{\text{ub},i} - E_{\text{lb},i}), \quad (8.18)$$

where i is the spectral group index and E_{ub} and E_{lb} represent the upper and lower energy boundaries of the spectral groups.

The validity of this technique was confirmed by applying it to a simple HYADES simulation. 300 μm of low density (0.1 mg cm^{-3} hydrogen gas was irradiated by Planckian X-ray source at a radiation temperature of 314 eV. For such a low opacity target, one should expect effectively 100% transmission of X-rays through the target. The simulation used 40 photon groups with upper boundaries equally spaced (in logarithmic space) between 0.01 keV and 5 keV. The photon group structure is shown in figure 8.1. The resulting group boundary emission from the HYADES simulation was found using equation 8.18 and is represented graphically in figure 8.2. The total area of the histogram is equivalent to the F_{tot} term in equation 8.18. Also plotted is the spectral intensity profile a perfect Planckian 314 eV source.

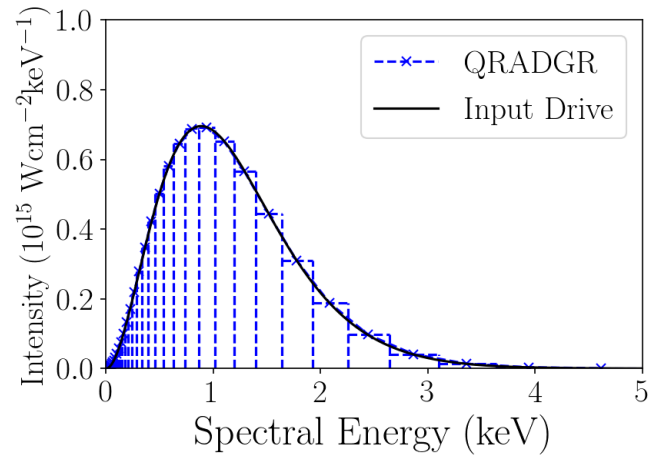


Figure 8.2: A histogram plot of the total boundary group emission represented by equation 8.18. Each rectangle represents one term in the sum, the total flux is then the combined area of the histogram. The solid black line represents the spectral intensity profile of the 314 eV input source.

As the hydrogen gas absorbs a negligible amount of X-rays, we should expect the QRADGR profile to closely match the profile of the ideal 314 eV source. The clear match in figure 8.2 confirms this technique for extracting X-ray flux is accurate.

List of References

- [1] World Energy Council. World Energy Scenarios 2016 - The Grand Transition, 2016.
- [2] Hans-Wilhelm Schiffer, Tom Kober, and Evangelos Panos. World Energy Council's Global Energy Scenarios to 2060. *Zeitschrift für Energiewirtschaft*, 42(2):91–102, 2018. ISSN 1866-2765. doi:10.1007/s12398-018-0225-3. URL <https://doi.org/10.1007/s12398-018-0225-3>.
- [3] International Energy Agency. World Energy Outlook 2019. <https://www.iea.org/reports/world-energy-outlook-2019/electricity>, 2019.
- [4] John D Lawson. Some criteria for a power producing thermonuclear reactor. *Proceedings of the physical society. Section B*, 70(1):6, 1957.
- [5] John Nuckolls, Lowell Wood, Albert Thiessen, and George Zimmerman. Laser compression of matter to super-high densities: Thermonuclear (ctr) applications. *Nature*, 239(5368):139–142, 1972.
- [6] Stefano Atzeni and Jürgen Meyer-ter Vehn. *The Physics of Inertial Fusion: BeamPlasma Interaction, Hydrodynamics, Hot Dense Matter*, volume 125. OUP Oxford, 2004.
- [7] Susanne Pfalzner. *An introduction to inertial confinement fusion*. CRC Press, 2006.
- [8] George H Miller, Edward I Moses, and Craig R Wuest. The national ignition facility. *Optical Engineering*, 43(12):2841–2854, 2004.
- [9] John Lindl, Otto Landen, John Edwards, and Ed Moses. Review of the national ignition campaign 2009-2012. *Physics of Plasmas*, 21(2), 2014. ISSN 1070664X. doi:10.1063/1.4865400.
- [10] S. Le Pape, L. F. Berzak Hopkins, L. Divol, A. Pak, E. L. Dewald, S. Bhandarkar, L. R. Benedetti, T. Bunn, J. Biener, J. Crippen, D. Casey, D. Edgell, D. N. Fittinghoff, M. Gatu-Johnson, C. Goyon, S. Haan, R. Hatarik, M. Havre, D. D-M. Ho, N. Izumi, J. Jaquez, S. F. Khan, G. A. Kyrala, T. Ma, A. J. Mackinnon, A. G. Macphee, B. J. Macgowan, N. B. Meezan, J. Milovich, M. Millot, P. Michel, S. R. Nagel, A. Nikroo, P. Patel, J. Ralph, J. S. Ross, N. G. Rice, D. Strozzi, M. Stadermann, P. Volegov, C. Yeamans, C. Weber, C. Wild, D. Callahan, and O. A. Hurricane. Fusion Energy Output Greater than the Kinetic Energy of an Imploding Shell at the National Ignition Facility. *Physical Review*

- Letters*, 120(24):245003, jun 2018. ISSN 10797114. doi:[10.1103/PhysRevLett.120.245003](https://doi.org/10.1103/PhysRevLett.120.245003). URL <https://link.aps.org/doi/10.1103/PhysRevLett.120.245003>.
- [11] RL McCrory, RE Bahr, R Betti, TR Boehly, TJB Collins, RS Craxton, JA Delettrez, WR Donaldson, R Epstein, J Frenje, et al. Omega icf experiments and preparation for direct drive ignition on nif. *Nuclear fusion*, 41(10):1413, 2001.
- [12] John D Lindl, Peter Amendt, Richard L Berger, S Gail Glendinning, Siegfried H Glenzer, Steven W Haan, Robert L Kauffman, Otto L Landen, and Laurence J Suter. The physics basis for ignition using indirect-drive targets on the national ignition facility. *Physics of plasmas*, 11(2):339–491, 2004.
- [13] JD Moody, DA Callahan, DE Hinkel, PA Amendt, KL Baker, D Bradley, PM Celliers, EL Dewald, L Divol, T Döppner, et al. Progress in hohlraum physics for the national ignition facility. *Physics of Plasmas*, 21(5):056317, 2014.
- [14] DE Hinkel, DA Callahan, AB Langdon, SH Langer, CH Still, and EA Williams. Analyses of laser-plasma interactions in national ignition facility ignition targets. *Physics of Plasmas*, 15(5):056314, 2008.
- [15] R. H.H. Scott, D. S. Clark, D. K. Bradley, D. A. Callahan, M. J. Edwards, S. W. Haan, O. S. Jones, B. K. Spears, M. M. Marinak, R. P.J. Town, P. A. Norreys, and L. J. Suter. Numerical modeling of the sensitivity of x-ray driven implosions to low-mode flux asymmetries. *Physical Review Letters*, 110(7):075001, feb 2013. ISSN 00319007. doi:[10.1103/PhysRevLett.110.075001](https://doi.org/10.1103/PhysRevLett.110.075001). URL <https://link.aps.org/doi/10.1103/PhysRevLett.110.075001>.
- [16] Brian K. Spears, M. J. Edwards, S. Hatchett, J. Kilkenny, J. Knauer, A. Kritcher, J. Lindl, D. Munro, P. Patel, H. F. Robey, and R. P.J. Town. Mode 1 drive asymmetry in inertial confinement fusion implosions on the National Ignition Facility. *Physics of Plasmas*, 21(4):042702, apr 2014. ISSN 10897674. doi:[10.1063/1.4870390](https://doi.org/10.1063/1.4870390). URL <http://aip.scitation.org/doi/10.1063/1.4870390>.
- [17] VA Smalyuk, DT Casey, DS Clark, MJ Edwards, SW Haan, A Hamza, DE Hoover, WW Hsing, O Hurricane, JD Kilkenny, et al. First measurements of hydrodynamic instability growth in indirectly driven implosions at ignition-relevant conditions on the national ignition facility. *Physical Review Letters*, 112(18):185003, 2014.
- [18] VA Smalyuk, SV Weber, DT Casey, DS Clark, JE Field, SW Haan, BA Hammel, AV Hamza, DE Hoover, OL Landen, et al. Hydrodynamic instability growth of three-dimensional, “native-roughness” modulations in x-ray driven, spherical implosions at the national ignition facility. *Physics of Plasmas*, 22(7):072704, 2015.
- [19] R. Tommasini, J. E. Field, B. A. Hammel, O. L. Landen, S. W. Haan, C. Aracne-Ruddle, L. R. Benedetti, D. K. Bradley, D. A. Callahan, E. L. Dewald, T. Doepfner, M. J. Edwards, O. A. Hurri-

- cane, N. Izumi, O. A. Jones, T. Ma, N. B. Meezan, S. R. Nagel, J. R. Rygg, K. S. Segraves, M. Stadermann, R. J. Strauser, and R. P. J. Town. Tent-induced perturbations on areal density of implosions at the National Ignition Facility). *Physics of Plasmas*, 22(5):056315, may 2015. ISSN 1070-664X. doi:10.1063/1.4921218. URL <http://scitation.aip.org/content/aip/journal/pop/22/5/10.1063/1.4921218>.
- [20] DS Clark, CR Weber, JL Milovich, AE Pak, DT Casey, BA Hammel, DD Ho, OS Jones, JM Koning, AL Kritcher, et al. Three-dimensional modeling and hydrodynamic scaling of national ignition facility implosions. *Physics of Plasmas*, 26(5):050601, 2019.
- [21] OA Hurricane, PT Springer, PK Patel, DA Callahan, K Baker, DT Casey, L Divol, T Döppner, DE Hinkel, M Hohenberger, et al. Approaching a burning plasma on the nif. *Physics of Plasmas*, 26(5):052704, 2019.
- [22] National Research Council et al. *An assessment of the prospects for inertial fusion energy*. National Academies Press, 2013.
- [23] L J Perkins, R Betti, K N Lafortune, and W H Williams. Shock ignition: A new approach to high gain inertial confinement fusion on the national ignition facility. *Physical Review Letters*, 103(4):1–4, 2009. ISSN 00319007. doi:10.1103/PhysRevLett.103.045004.
- [24] LJ Perkins, BG Logan, GB Zimmerman, and CJ Werner. Two-dimensional simulations of thermonuclear burn in ignition-scale inertial confinement fusion targets under compressed axial magnetic fields. *Physics of Plasmas*, 20(7):072708, 2013.
- [25] Peter Amendt, JD Colvin, RE Tipton, DE Hinkel, MJ Edwards, OL Landen, John D Ramshaw, LJ Suter, WS Varnum, and RG Watt. Indirect-drive noncryogenic double-shell ignition targets for the national ignition facility: Design and analysis. *Physics of Plasmas*, 9(5):2221–2233, 2002.
- [26] TJ Boyd, TJM Boyd, and JJ Sanderson. *The physics of plasmas*. Cambridge University Press, 2003.
- [27] Donald Gary Swanson. *Plasma kinetic theory*. Crc Press, 2008.
- [28] Irvine I Glass and Jean Pascal Sisljan. *Nonstationary flows and shock waves*. Clarendon press Oxford, 1994.
- [29] Lev D Landau and Evgenij M Lifshitz. Fluid mechanics 2nd ed. *Pergamon*, pages 61–252, 1987.
- [30] Jon Larsen. *Foundations of high-energy-density physics: physical processes of matter at extreme conditions*. Cambridge University Press, 2017.
- [31] Hans Schamel. Lagrangian fluid description with simple applications in compressible plasma and gas dynamics. *Physics reports*, 392(5):279–319, 2004.

- [32] Paul Gibbon. *Short pulse laser interactions with matter*. World Scientific Publishing Company Singapore, 2004.
- [33] R Paul Drake. High-energy-density physics. *Phys. Today*, 63(6):28, 2010.
- [34] Lyman Spitzer and Richard Härm. Transport phenomena in a completely ionized gas. *Physical Review*, 89(5):977–981, mar 1953. ISSN 0031899X. doi:10.1103/PhysRev.89.977. URL <https://link.aps.org/doi/10.1103/PhysRev.89.977>.
- [35] Y. T. Lee and R. M. More. An electron conductivity model for dense plasmas. *Physics of Fluids*, 27(5):1273–1286, 1984. ISSN 10706631. doi:10.1063/1.864744. URL <https://aip.scitation.org/doi/10.1063/1.864744>.
- [36] H Brysk, P M Campbell, and P Hammerling. Thermal conduction in laser fusion. *Plasma Physics*, 17(6):473–484, jun 1975. ISSN 00321028. doi:10.1088/0032-1028/17/6/007. URL <https://iopscience.iop.org/article/10.1088/0032-1028/17/6/007>.
- [37] John I Castor. *Radiation hydrodynamics*. 2004.
- [38] Jeff Colvin and Jon Larsen. *Extreme physics: properties and behavior of matter at extreme conditions*. Cambridge University Press, 2013.
- [39] R. E. Marshak. Effect of radiation on shock wave behavior. *Physics of Fluids*, 1(1):24–29, 1958. ISSN 10706631. doi:10.1063/1.1724332.
- [40] R. Pakula and R. Sigel. Self-similar expansion of dense matter due to heat transfer by nonlinear conduction. *Physics of Fluids*, 28(1):232–244, jan 1985. ISSN 0031-9171. doi:10.1063/1.865184. URL <https://aip.scitation.org/doi/10.1063/1.865184>.
- [41] James H. Hammer and Mordecai D. Rosen. A consistent approach to solving the radiation diffusion equation. In *Physics of Plasmas*, volume 10, pages 1829–1845, may 2003. doi:10.1063/1.1564599. URL <http://aip.scitation.org/doi/10.1063/1.1564599>.
- [42] Mordecai D Rosen and James H Hammer. Analytic expressions for optimal inertial-confinement-fusion hohlraum wall density and wall loss. *Physical Review E*, 72(5):056403, 2005.
- [43] OA Hurricane and JH Hammer. Bent marshak waves. *Physics of plasmas*, 13(11):113303, 2006.
- [44] Grigory Isaakovich Barenblatt, Grigorii Isaakovič Barenblatt, and Barenblatt Grigory Isaakovich. *Scaling, self-similarity, and intermediate asymptotics: dimensional analysis and intermediate asymptotics*, volume 14. Cambridge University Press, 1996.

- [45] SP Hatchett. Ablation gas dynamics of low-Z materials illuminated by soft x rays. *Presented at the Inertial Fusion Lecture Series, . . .*, Lawrence L(UCRL-JC-108348), 1991. URL <http://adsabs.harvard.edu/abs/1991ifls.reptQ...H>.
- [46] M. Murakami and J. Meyer-Ter-vehn. Indirectly driven targets for inertial confinement fusion. *Nuclear Fusion*, 31(7):1315–1331, 1991. ISSN 17414326. doi:10.1088/0029-5515/31/7/007.
- [47] Mikhail Basko. An improved version of the view factor method for simulating inertial confinement fusion hohlraums. *Physics of Plasmas*, 3(11):4148–4155, 1996. ISSN 1070664X. doi:10.1063/1.871565.
- [48] Ricardo Betti, PY Chang, BK Spears, KS Anderson, J Edwards, M Fatenejad, JD Lindl, RL McCrory, R Nora, and D Shvarts. Thermonuclear ignition in inertial confinement fusion and comparison with magnetic confinement. *Physics of Plasmas*, 17(5):058102, 2010.
- [49] PY Chang, R Betti, BK Spears, KS Anderson, J Edwards, M Fatenejad, JD Lindl, RL McCrory, R Nora, and D Shvarts. Generalized measurable ignition criterion for inertial confinement fusion. *Physical review letters*, 104(13):135002, 2010.
- [50] Brian K Spears, S Glenzer, MJ Edwards, S Brandon, D Clark, R Town, C Cerjan, R Dylla-Spears, E Mapoles, D Munro, et al. Performance metrics for inertial confinement fusion implosions: Aspects of the technical framework for measuring progress in the national ignition campaign. *Physics of Plasmas*, 19(5):056316, 2012.
- [51] R. Betti and C. Zhou. High-density and high- ρ R fuel assembly for fast-ignition inertial confinement fusion. *Physics of Plasmas*, 12(11):1–4, nov 2005. ISSN 1070664X. doi:10.1063/1.2127932. URL <http://aip.scitation.org/doi/10.1063/1.2127932>.
- [52] M. C. Herrmann, M Tabak, and J. D. Lindl. A generalized scaling law for the ignition energy of inertial confinement fusion capsules. *Nuclear Fusion*, 41(1):99–111, jan 2001. ISSN 00295515. doi:10.1088/0029-5515/41/1/308. URL <https://iopscience.iop.org/article/10.1088/0029-5515/41/1/308>.
- [53] R Betti, K Anderson, T R Boehly, T. J.B. Collins, R S Craxton, J A Delettrez, D H Edgell, R Epstein, V Yu Glebov, V N Goncharov, D R Harding, R L Keck, J H Kelly, J P Knauer, S J Loucks, J A Marozas, F J Marshall, A V Maximov, D N Maywar, R L McCrory, P W McKenty, D D Meyerhofer, J Myatt, P B Radha, S P Regan, C Ren, T C Sangster, W Seka, S Skupsky, A A Solodov, V A Smalyuk, J M Soures, C Stoeck, W Theobald, B Yaakobi, C Zhou, J D Zuegel, J A Frenje, C K Li, R D Petrasso, and F H Seguin. Progress in hydrodynamics theory and experiments for direct-drive and fast ignition inertial confinement fusion. *Plasma Physics and Controlled Fusion*, 48(12 B):B153–B163, dec 2006. ISSN 07413335. doi:10.1088/0741-3335/48/12B/S15. URL <https://iopscience.iop.org/article/10.1088/0741-3335/48/12B/S15>.

- [54] S. W. Haan, J. D. Lindl, D. A. Callahan, D. S. Clark, J. D. Salmonson, B. A. Hammel, L. J. Atherton, R. C. Cook, M. J. Edwards, S. Glenzer, A. V. Hamza, S. P. Hatchett, M. C. Herrmann, D. E. Hinkel, D. D. Ho, H. Huang, O. S. Jones, J. Kline, G. Kyrala, O. L. Landen, B. J. MacGowan, M. M. Marinak, D. D. Meyerhofer, J. L. Milovich, K. A. Moreno, E. I. Moses, D. H. Munro, A. Nikroo, R. E. Olson, K. Peterson, S. M. Pollaine, J. E. Ralph, H. F. Robey, B. K. Spears, P. T. Springer, L. J. Suter, C. A. Thomas, R. P. Town, R. Vesey, S. V. Weber, H. L. Wilkens, and D. C. Wilson. Point design targets, specifications, and requirements for the 2010 ignition campaign on the National Ignition Facility. *Physics of Plasmas*, 18(5):051001, may 2011. ISSN 1070664X. doi:[10.1063/1.3592169](https://doi.org/10.1063/1.3592169). URL <http://aip.scitation.org/doi/10.1063/1.3592169>.
- [55] VA Shcherbakov. Ignition of a laser-fusion target by a focusing shock wave. *Soviet Journal of Plasma Physics*, 9(2):240–241, 1983.
- [56] C. Zhou and R. Betti. *Bulletin of the American Physical Society*, 50(140), 2005.
- [57] R. Betti, W. Theobald, C. D. Zhou, K. S. Anderson, P. W. McKenty, S. Skupsky, D. Shvarts, V. N. Goncharov, J. A. Delettrez, P. B. Radha, T. C. Sangster, C. Stoeckl, and D. D. Meyerhofer. Shock ignition of thermonuclear fuel with high areal densities. *Journal of Physics: Conference Series*, 112(Part 2):1–4, 2008. ISSN 17426596. doi:[10.1088/1742-6596/112/2/022024](https://doi.org/10.1088/1742-6596/112/2/022024).
- [58] S. Atzeni, X. Ribeyre, G. Schurtz, A. J. Schmitt, B. Canaud, R. Betti, and L. J. Perkins. Shock ignition of thermonuclear fuel: Principles and modelling. *Nuclear Fusion*, 54(5), 2014. ISSN 17414326. doi:[10.1088/0029-5515/54/5/054008](https://doi.org/10.1088/0029-5515/54/5/054008).
- [59] D. Batani, S. Baton, A. Casner, S. Depierreux, M. Hohenberger, O. Klimo, M. Koenig, C. Labaune, X. Ribeyre, C. Rousseaux, G. Schurtz, W. Theobald, and V. T. Tikhonchuk. Physics issues for shock ignition. *Nuclear Fusion*, 54(5), 2014. ISSN 17414326. doi:[10.1088/0029-5515/54/5/054009](https://doi.org/10.1088/0029-5515/54/5/054009).
- [60] R. Betti and O. A. Hurricane. Inertial-confinement fusion with lasers. *Nat Phys*, 12(5):435–448, may 2016. ISSN 1745-2473. URL <http://dx.doi.org/10.1038/nphys3736><http://10.0.4.14/nphys3736>.
- [61] V. T. Tikhonchuk, A. Colaitis, A. Vallet, E. Llor Aisa, G. Duchateau, Ph. Nicolai, and X. Ribeyre. Physics of laser-plasma interaction for shock ignition of fusion reactions. *Plasma Physics and Controlled Fusion*, 58(1), 2015. ISSN 13616587. doi:[10.1088/0741-3335/58/1/014018](https://doi.org/10.1088/0741-3335/58/1/014018).
- [62] X. Ribeyre, G. Schurtz, M. Lafon, S. Galera, and S. Weber. Shock ignition: An alternative scheme for HiPER. *Plasma Physics and Controlled Fusion*, 51(1), 2009. ISSN 07413335. doi:[10.1088/0741-3335/51/1/015013](https://doi.org/10.1088/0741-3335/51/1/015013).
- [63] X. Ribeyre, M. Lafon, G. Schurtz, M. Olazabal-Loumé, J. Breil, S. Galera, and S. Weber. Shock ignition: Modelling and target design robustness. *Plasma Physics and Controlled Fusion*, 51(12), 2009. ISSN 07413335. doi:[10.1088/0741-3335/51/12/124030](https://doi.org/10.1088/0741-3335/51/12/124030).

- [64] M. Lafon, X. Ribeyre, and G. Schurtz. Gain curves and hydrodynamic modeling for shock ignition. *Physics of Plasmas*, 17(5):052704, may 2010. ISSN 1070664X. doi:[10.1063/1.3407623](https://doi.org/10.1063/1.3407623). URL <http://aip.scitation.org/doi/10.1063/1.3407623>.
- [65] G Schurtz, X Ribeyre, and M Lafon. Target design for shock ignition. *Journal of Physics: Conference Series*, 244(PART 2):4–8, 2010. ISSN 17426596. doi:[10.1088/1742-6596/244/2/022013](https://doi.org/10.1088/1742-6596/244/2/022013).
- [66] M. Hohenberger, W. Theobald, S. X. Hu, K. S. Anderson, R. Betti, T. R. Boehly, A. Casner, D. E. Fratanduono, M. Lafon, D. D. Meyerhofer, R. Nora, X. Ribeyre, T. C. Sangster, G. Schurtz, W. Seka, C. Stoeckl, and B. Yaakobi. Shock-ignition relevant experiments with planar targets on OMEGA. *Physics of Plasmas*, 21(2):1–6, 2014. ISSN 1070664X. doi:[10.1063/1.4865373](https://doi.org/10.1063/1.4865373).
- [67] R. Nora, W. Theobald, R. Betti, F. J. Marshall, D. T. Michel, W. Seka, B. Yaakobi, M. Lafon, C. Stoeckl, J. Delettrez, A. A. Solodov, A. Casner, C. Reverdin, X. Ribeyre, A. Vallet, J. Peebles, F. N. Beg, and M. S. Wei. Gigabar spherical shock generation on the OMEGA laser. *Physical Review Letters*, 114(4):045001, jan 2015. ISSN 10797114. doi:[10.1103/PhysRevLett.114.045001](https://doi.org/10.1103/PhysRevLett.114.045001). URL <https://link.aps.org/doi/10.1103/PhysRevLett.114.045001>.
- [68] W. Theobald, R. Nora, W. Seka, M. Lafon, K. S. Anderson, M. Hohenberger, F. J. Marshall, D. T. Michel, A. A. Solodov, C. Stoeckl, D. H. Edgell, B. Yaakobi, A. Casner, C. Reverdin, X. Ribeyre, A. Shvydky, A. Vallet, J. Peebles, F. N. Beg, M. S. Wei, and R. Betti. Spherical strong-shock generation for shock-ignition inertial fusion. *Physics of Plasmas*, 22(5):056310, may 2015. ISSN 10897674. doi:[10.1063/1.4920956](https://doi.org/10.1063/1.4920956). URL <http://scitation.aip.org/content/aip/journal/pop/22/5/10.1063/1.4920956>.
- [69] O Klimo and V T Tikhonchuk. Laser-plasma interaction studies in the context of shock ignition: The regime dominated by parametric instabilities. *Plasma Physics and Controlled Fusion*, 55(9):095002, sep 2013. ISSN 07413335. doi:[10.1088/0741-3335/55/9/095002](https://doi.org/10.1088/0741-3335/55/9/095002). URL <https://iopscience.iop.org/article/10.1088/0741-3335/55/9/095002>.
- [70] G. Cristoforetti, A. Colaïtis, L. Antonelli, S. Atzeni, F. Baffigi, D. Batani, F. Barbato, G. Boutoux, R. Dudzak, P. Koester, E. Krousky, L. Labate, Ph. Nicolaï, O. Renner, M. Skoric, V. Tikhonchuk, and L. A. Gizzi. Experimental observation of parametric instabilities at laser intensities relevant for shock ignition. *EPL*, 117(3):35001, feb 2017. ISSN 12864854. doi:[10.1209/0295-5075/117/35001](https://doi.org/10.1209/0295-5075/117/35001). URL <https://iopscience.iop.org/article/10.1209/0295-5075/117/35001>.
- [71] A. Colaïtis, X. Ribeyre, E. Le Bel, G. Duchateau, Ph. Nicolaï, and V. Tikhonchuk. Influence of laser induced hot electrons on the threshold for shock ignition of fusion reactions. *Physics of Plasmas*, 23(7):072703, jul 2016. ISSN 10897674. doi:[10.1063/1.4958808](https://doi.org/10.1063/1.4958808). URL <http://aip.scitation.org/doi/10.1063/1.4958808>.

- [72] Ph. Nicolai, J. L. Feugeas, M. Touati, X. Ribeyre, S. Gus'Kov, and V. Tikhonchuk. Deleterious effects of nonthermal electrons in shock ignition concept. *Physical Review E - Statistical, Nonlinear, and Soft Matter Physics*, 89(3):033107, mar 2014. ISSN 15502376. doi:[10.1103/PhysRevE.89.033107](https://doi.org/10.1103/PhysRevE.89.033107). URL <https://link.aps.org/doi/10.1103/PhysRevE.89.033107>.
- [73] Cascade Applied Sciences Inc. <http://casinc.com>. Accessed: 09-2020.
- [74] Jon T Larsen and Stephen M Lane. HYADES—A plasma hydrodynamics code for dense plasma studies. *Journal of Quantitative Spectroscopy and Radiative Transfer*, 51(1):179–186, 1994. ISSN 0022-4073. doi:[https://doi.org/10.1016/0022-4073\(94\)90078-7](https://doi.org/10.1016/0022-4073(94)90078-7). URL <http://www.sciencedirect.com/science/article/pii/0022407394900787>.
- [75] John VonNeumann and Robert D Richtmyer. A method for the numerical calculation of hydrodynamic shocks. *Journal of applied physics*, 21(3):232–237, 1950.
- [76] BI Bennett, JD Johnson, GI Kerley, and GT Rood. Recent developments in the sesame equation-of-state library. Technical report, Los Alamos Scientific Lab., N. Mex.(USA), 1978.
- [77] Richard M More. Electronic energy-levels in dense plasmas. *Journal of Quantitative Spectroscopy and Radiative Transfer*, 27(3):345–357, 1982.
- [78] J E Bailey, T Nagayama, G P Loisel, G A Rochau, C Blancard, J Colgan, Ph. Cosse, G Faussurier, C J Fontes, F Gilleron, I Golovkin, S B Hansen, C A Iglesias, D P Kilcrease, J J MacFarlane, R C Mancini, S N Nahar, C Orban, J.-C. Pain, A K Pradhan, M Sherrill, and B G Wilson. A higher-than-predicted measurement of iron opacity at solar interior temperatures. *Nature*, 517(7532):56–59, 2015. ISSN 1476-4687. doi:[10.1038/nature14048](https://doi.org/10.1038/nature14048). URL <https://doi.org/10.1038/nature14048>.
- [79] T. M. Guymmer, A. S. Moore, J. Morton, J. L. Kline, S. Allan, N. Bazin, J. Benstead, C. Bentley, A. J. Comley, J. Cowan, K. Flippo, W. Garbett, C. Hamilton, N. E. Lanier, K. Mussack, K. Obrey, L. Reed, D. W. Schmidt, R. M. Stevenson, J. M. Taccetti, and J. Workman. Quantifying equation-of-state and opacity errors using integrated supersonic diffusive radiation flow experiments on the national ignition facility. *Physics of Plasmas*, 22(4):043303, 2015. doi:[10.1063/1.4919025](https://doi.org/10.1063/1.4919025). URL <https://doi.org/10.1063/1.4919025>.
- [80] HF Robey, Ye Zhou, AC Buckingham, P Keiter, BA Remington, and RP Drake. The time scale for the transition to turbulence in a high reynolds number, accelerated flow. *Physics of Plasmas*, 10(3):614–622, 2003.
- [81] A. Casner, D. Martinez, V. Smalyuk, L. Masse, J.O. Kane, B. Villette, J. Fariaut, G. Oudot, S. Liberatore, R.C. Mancini, B.A. Remington, and R.F. Heeter. Long duration x-ray drive hydrodynamics experiments relevant for laboratory astrophysics. *High Energy Density Physics*, 17:146 – 150, 2015.

- ISSN 1574-1818. doi:<https://doi.org/10.1016/j.hedp.2014.09.003>. URL <http://www.sciencedirect.com/science/article/pii/S1574181814000573>. 10th International Conference on High Energy Density Laboratory Astrophysics.
- [82] C Michaut, C Stehlé, S Leygnac, T Lanz, and L Boireau. Jump conditions in hypersonic shocks. *The European Physical Journal D-Atomic, Molecular, Optical and Plasma Physics*, 28(3):381–392, 2004.
- [83] LM Haffner, R-J Dettmar, JE Beckman, K Wood, JD Slavin, C Giammanco, GJ Madsen, A Zurita, and RJ Reynolds. The warm ionized medium in spiral galaxies. *Reviews of Modern Physics*, 81(3):969, 2009.
- [84] Bruce A Remington, R Paul Drake, and Dmitri D Ryutov. Experimental astrophysics with high power lasers and z pinches. *Reviews of Modern Physics*, 78(3):755, 2006.
- [85] John Lindl. Development of the indirect-drive approach to inertial confinement fusion and the target physics basis for ignition and gain. *Physics of Plasmas*, 2(11):3933, 1995. ISSN 1070664X. doi:10.1063/1.871025. URL <http://scitation.aip.org/content/aip/journal/pop/2/11/10.1063/1.871025>; <http://scitation.aip.org/content/aip/journal/pop/2/11/10.1063/1.871025;jsessionid=2gj3ri51mlcdh.x-aip-live-02>.
- [86] B Spears, D Hicks, C Velsko, M Stoyer, H Robey, D Munro, S Haan, O Landen, A Nikroo, and H Huang. Influence and measurement of mass ablation in ICF implosions. In *Journal of Physics: Conference Series*, volume 112, page 022003, may 2008. doi:10.1088/1742-6596/112/2/022003. URL <https://iopscience.iop.org/article/10.1088/1742-6596/112/2/022003>.
- [87] O. L. Landen, T. R. Boehly, D. K. Bradley, D. G. Braun, D. A. Callahan, P. M. Celliers, G. W. Collins, E. L. Dewald, L. Divol, S. H. Glenzer, A. Hamza, D. G. Hicks, N. Hoffman, N. Izumi, O. S. Jones, R. K. Kirkwood, G. A. Kyrala, P. Michel, J. Milovich, D. H. Munro, A. Nikroo, R. E. Olson, H. F. Robey, B. K. Spears, C. A. Thomas, S. V. Weber, D. C. Wilson, M. M. Marinak, L. J. Suter, B. A. Hammel, D. D. Meyerhofer, J. Atherton, J. Edwards, S. W. Haan, J. D. Lindl, B. J. MacGowan, and E. I. Moses. Capsule performance optimization in the National Ignition Campaign. In *Physics of Plasmas*, volume 17, page 056301, may 2010. doi:10.1063/1.3298882. URL <http://aip.scitation.org/doi/10.1063/1.3298882>.
- [88] D. S. Clark, A. L. Kritcher, S. A. Yi, A. B. Zylstra, S. W. Haan, and C. R. Weber. Capsule physics comparison of National Ignition Facility implosion designs using plastic, high density carbon, and beryllium ablaters. *Physics of Plasmas*, 25(3):032703, mar 2018. ISSN 10897674. doi:10.1063/1.5016874. URL <http://aip.scitation.org/doi/10.1063/1.5016874>.
- [89] Daniel S. Clark, Steven W. Haan, Bruce A. Hammel, Jay D. Salmonson, Debra A. Callahan, and Richard P.J. Town. Plastic ablator ignition capsule design for the National Ignition Facility. In *Physics*

- of *Plasmas*, volume 17, page 052703, may 2010. doi:[10.1063/1.3403293](https://doi.org/10.1063/1.3403293). URL <http://aip.scitation.org/doi/10.1063/1.3403293>.
- [90] A. J. Mackinnon, N. B. Meezan, J. S. Ross, S. Le Pape, L. Berzak Hopkins, L. Divol, D. Ho, J. Milovich, A. Pak, J. Ralph, T. Döppner, P. K. Patel, C. Thomas, R. Tommasini, S. Haan, A. G. Macphee, J. McNaney, J. Caggiano, R. Hatarik, R. Bionta, T. Ma, B. Spears, J. R. Rygg, L. R. Benedetti, R. P.J. Town, D. K. Bradley, E. L. Dewald, D. Fittinghoff, O. S. Jones, H. R. Robey, J. D. Moody, S. Khan, D. A. Callahan, A. Hamza, J. Biener, P. M. Celliers, D. G. Braun, D. J. Erskine, S. T. Prisbrey, R. J. Wallace, B. Koziowski, R. Dylla-Spears, J. Sater, G. Collins, E. Storm, W. Hsing, O. Landen, J. L. Atherton, J. D. Lindl, M. J. Edwards, J. A. Frenje, M. Gatu-Johnson, C. K. Li, R. Petrasso, H. Rinderknecht, M. Rosenberg, F. H. Séguin, A. Zylstra, J. P. Knauer, G. Grim, N. Guler, F. Merrill, R. Olson, G. A. Kyrala, J. D. Kilkenny, A. Nikroo, K. Moreno, D. E. Hoover, C. Wild, and E. Werner. High-density carbon ablator experiments on the National Ignition Facility. *Physics of Plasmas*, 21(5):056318, may 2014. ISSN 10897674. doi:[10.1063/1.4876611](https://doi.org/10.1063/1.4876611). URL <http://aip.scitation.org/doi/10.1063/1.4876611>.
- [91] L. Berzak Hopkins, S. Lepape, L. Divol, A. Pak, E. Dewald, D. D. Ho, N. Meezan, S. Bhandarkar, L. R. Benedetti, T. Bunn, J. Biener, J. Crippen, D. Casey, D. Clark, D. Edgell, D. Fittinghoff, M. Gatu-Johnson, C. Goyon, S. Haan, R. Hatarik, M. Havre, D. Hinkel, H. Huang, N. Izumi, J. Jaquez, O. Jones, S. Khan, A. Kritcher, C. Kong, G. Kyrala, O. Landen, T. Ma, A. Macphee, B. Macgowan, A. J. Mackinnon, M. Marinak, J. Milovich, M. Millot, P. Michel, A. Moore, S. R. Nagel, A. Nikroo, P. Patel, J. Ralph, H. Robey, J. S. Ross, N. G. Rice, S. Sepke, V. A. Smalyuk, P. Sterne, D. Strozzi, M. Stadermann, P. Volegov, C. Weber, C. Wild, C. Yeamans, D. Callahan, O. Hurricane, R. P.J. Town, and M. J. Edwards. Toward a burning plasma state using diamond ablator inertially confined fusion (ICF) implosions on the National Ignition Facility (NIF). *Plasma Physics and Controlled Fusion*, 61(1), 2019. ISSN 13616587. doi:[10.1088/1361-6587/aad97e](https://doi.org/10.1088/1361-6587/aad97e).
- [92] Douglas C. Wilson, Paul A. Bradley, Nelson M. Hoffman, Fritz J. Swenson, David P. Smitherman, Robert E. Chrien, Robert W. Margevicius, D. J. Thoma, Larry R. Foreman, James K. Hoffer, S. Robert Goldman, Stephen E. Caldwell, Thomas R. Dittrich, Steven W. Haan, Michael M. Marinak, Stephen M. Pollaine, and Jorge J. Sanchez. The development and advantages of beryllium capsules for the National Ignition Facility. *Physics of Plasmas*, 5(5 PART 1):1953–1959, may 1998. ISSN 1070664X. doi:[10.1063/1.872865](https://doi.org/10.1063/1.872865). URL <http://aip.scitation.org/doi/10.1063/1.872865>.
- [93] Andrei N. Simakov, Douglas C. Wilson, Sunghwan A. Yi, John L. Kline, Daniel S. Clark, Jose L. Milovich, Jay D. Salmonson, and Steven H. Batha. Optimized beryllium target design for indirectly driven inertial confinement fusion experiments on the national ignition facility. *Physics of Plasmas*, 21(2):022701, feb 2014. ISSN 1070664X. doi:[10.1063/1.4864331](https://doi.org/10.1063/1.4864331). URL <http://aip.scitation.org/doi/10.1063/1.4864331>.

- [94] S. Le Pape, L. F. Berzak Hopkins, L. Divol, N. Meezan, D. Turnbull, A. J. MacKinnon, D. Ho, J. S. Ross, S. Khan, A. Pak, E. Dewald, L. R. Benedetti, S. Nagel, J. Biener, D. A. Callahan, C. Yeamans, P. Michel, M. Schneider, B. Koziowski, T. Ma, A. G. MacPhee, S. Haan, N. Izumi, R. Hatarik, P. Sterne, P. Celliers, J. Ralph, R. Rygg, D. Strozzi, J. Kilkenny, M. Rosenberg, H. Rinderknecht, H. Sio, M. Gatu-Johnson, J. Frenje, R. Petrasso, A. Zylstra, R. Town, O. Hurricane, A. Nikroo, and M. J. Edwards. The near vacuum hohlraum campaign at the NIF: A new approach. *Physics of Plasmas*, 23(5):056311, may 2016. ISSN 10897674. doi:[10.1063/1.4950843](https://doi.org/10.1063/1.4950843). URL <http://aip.scitation.org/doi/10.1063/1.4950843>.
- [95] RM More, KH Warren, DA Young, and GB Zimmerman. A new quotidian equation of state (qeos) for hot dense matter. *The Physics of fluids*, 31(10):3059–3078, 1988.
- [96] Alexander Kramida, Yuri Ralchenko, Joseph Reader, et al. Nist atomic spectra database (ver. 5.3), 2015.
- [97] R. E. Olson, G. A. Rochau, O. L. Landen, and R. J. Leeper. X-ray ablation rates in inertial confinement fusion capsule materials. *Physics of Plasmas*, 18(3):032706, mar 2011. ISSN 1070664X. doi:[10.1063/1.3566009](https://doi.org/10.1063/1.3566009). URL <http://aip.scitation.org/doi/10.1063/1.3566009>.
- [98] J. L. Kline, S. A. Yi, A. N. Simakov, R. E. Olson, D. C. Wilson, G. A. Kyrala, T. S. Perry, S. H. Batha, A. B. Zylstra, E. L. Dewald, R. Tommasini, J. E. Ralph, D. J. Strozzi, A. G. MacPhee, D. A. Callahan, D. E. Hinkel, O. A. Hurricane, J. L. Milovich, J. R. Rygg, S. F. Khan, S. W. Haan, P. M. Celliers, D. S. Clark, B. A. Hammel, B. Koziowski, M. B. Schneider, M. M. Marinak, H. G. Rinderknecht, H. F. Robey, J. D. Salmonson, P. K. Patel, T. Ma, M. J. Edwards, M. Stadermann, S. Baxamusa, C. Alford, M. Wang, A. Nikroo, N. Rice, D. Hoover, K. P. Youngblood, H. Xu, H. Huang, and H. Sio. First beryllium capsule implosions on the National Ignition Facility. *Physics of Plasmas*, 23(5):056310, may 2016. ISSN 10897674. doi:[10.1063/1.4948277](https://doi.org/10.1063/1.4948277). URL <http://aip.scitation.org/doi/10.1063/1.4948277>.
- [99] Ankit Rohatgi. Webplotdigitizer, 2017.
- [100] A. G. Seaton and T. D. Arber. Laser-plasma instabilities in long scale-length plasmas relevant to shock-ignition. *Physics of Plasmas*, 27(8):082704, 2020. doi:[10.1063/5.0010920](https://doi.org/10.1063/5.0010920). URL <https://doi.org/10.1063/5.0010920>.
- [101] S Weber and C Riconda. Temperature dependence of parametric instabilities in the context of the shock-ignition approach to inertial confinement fusion. *High Power Laser Science and Engineering*, 3, 2015.
- [102] K S Anderson, R Betti, P. W. McKenty, T. J.B. Collins, M Hohenberger, W. Theobald, R. S. Craxton, J. A. Delettrez, M. Lafon, J. A. Marozas, R. Nora, S. Skupsky, and A. Shvydki. A polar-drive shock-

- ignition design for the National Ignition Facility. *Physics of Plasmas*, 20(5), 2013. ISSN 1070664X. doi:[10.1063/1.4804635](https://doi.org/10.1063/1.4804635).
- [103] B. Canaud, F. Garaude, C. Clique, N Lecler, A. Masson, R. Quach, and J. Van Der Vliet. High-gain direct-drive laser fusion with indirect drive beam layout of Laser Mégajoule. *Nuclear Fusion*, 47(12):1652–1655, dec 2007. ISSN 00295515. doi:[10.1088/0029-5515/47/12/002](https://doi.org/10.1088/0029-5515/47/12/002). URL <https://iopscience.iop.org/article/10.1088/0029-5515/47/12/002>.
- [104] B Canaud and M Temporal. High-gain shock ignition of direct-drive ICF targets for the Laser Mégajoule. *New Journal of Physics*, 12(4):043037, apr 2010. ISSN 13672630. doi:[10.1088/1367-2630/12/4/043037](https://doi.org/10.1088/1367-2630/12/4/043037). URL <https://iopscience.iop.org/article/10.1088/1367-2630/12/4/043037>.
- [105] William Trickey and John Pasley. Producing shock-ignition-like pressures by indirect drive. *Plasma Physics and Controlled Fusion*, 61(10), 2019. ISSN 13616587. doi:[10.1088/1361-6587/ab3007](https://doi.org/10.1088/1361-6587/ab3007).
- [106] Stefano Atzeni, Angelo Schiavi, and Claudio Bellei. Targets for direct-drive fast ignition at total laser energy of 200-400 kJ. *Physics of Plasmas*, 14(5), 2007. ISSN 1070664X. doi:[10.1063/1.2716682](https://doi.org/10.1063/1.2716682).
- [107] X Ribeyre, Ph Nicola, G Schurtz, M Olazabal-Loumé, J Breil, P H Maire, J L Feugeas, L Hallo, and V T Tikhonchuk. Compression phase study of the HiPER baseline target. *Plasma Physics and Controlled Fusion*, 50(2), 2008. ISSN 07413335. doi:[10.1088/0741-3335/50/2/025007](https://doi.org/10.1088/0741-3335/50/2/025007).
- [108] Pierre Henri Maire, Rémi Abgrall, Jérôme Breil, and Jean Ovardia. A cell-centered lagrangian scheme for two-dimensional compressible flow problems. *SIAM Journal on Scientific Computing*, 29(4):1781–1824, 2007. ISSN 10648275. doi:[10.1137/050633019](https://doi.org/10.1137/050633019). URL <https://doi.org/10.1137/050633019>.
- [109] V N Goncharov. Basic Principles of Direct-Drive Ignition Target Design. *LLE REview*, 106, 2006.
- [110] Ray E. Kidder. Theory of Homogeneous Isentropic Compression and Its Application To Laser Fusion. (1):449–464, 1974. doi:[10.1007/978-1-4684-8416-8_3](https://doi.org/10.1007/978-1-4684-8416-8_3).
- [111] B. Canaud and F. Garaude. Optimization of laser-target coupling efficiency for direct drive laser fusion. *Nuclear Fusion*, 45(12), 2005. ISSN 00295515. doi:[10.1088/0029-5515/45/12/L01](https://doi.org/10.1088/0029-5515/45/12/L01).
- [112] B. J. Le Garrec, C. Hernandez-Gomez, T. Winstone, and J. Collier. HiPER laser architecture principles. *Journal of Physics: Conference Series*, 244(PART 3), 2010. ISSN 17426596. doi:[10.1088/1742-6596/244/3/032020](https://doi.org/10.1088/1742-6596/244/3/032020).
- [113] M. Temporal, B. Canaud, and B. J. Le Garrec. Irradiation uniformity and zooming performances for a capsule directly driven by a 32x9 laser beams configuration. *Physics of Plasmas*, 17(2), 2010. ISSN 1070664X. doi:[10.1063/1.3309489](https://doi.org/10.1063/1.3309489).

- [114] S H Glenzer, B J MacGowan, P Michel, N B Meezan, L J Suter, S N Dixit, J L Kline, G A Kyrala, D K Bradley, D A Callahan, E L Dewald, L Divol, E Dzenitis, M J Edwards, A V Hamza, C A Haynam, D E Hinkel, D H Kalantar, J D Kilkenny, O L Landen, J D Lindl, S. Lepape, J D Moody, A Nikroo, T Parham, M B Schneider, R. P.J. Town, P Wegner, K Widmann, P Whitman, B. K.F. Young, B Van Wonterghem, L J Atherton, and E I Moses. Symmetric inertial confinement fusion implosions at ultra-high laser energies. *Science*, 327(5970):1228–1231, mar 2010. ISSN 00368075. doi:[10.1126/science.1185634](https://doi.org/10.1126/science.1185634). URL <http://www.ncbi.nlm.nih.gov/pubmed/20110465>.
- [115] R. E. Olson, L. J. Suter, J. L. Kline, D. A. Callahan, M. D. Rosen, S. N. Dixit, O. L. Landen, N. B. Meezan, J. D. Moody, C. A. Thomas, A. Warrick, K. Widmann, E. A. Williams, and S. H. Glenzer. X-ray conversion efficiency in vacuum hohlraum experiments at the National Ignition Facility. *Physics of Plasmas*, 19(5), 2012. ISSN 1070664X. doi:[10.1063/1.4704795](https://doi.org/10.1063/1.4704795).
- [116] Tieqiang Chang, Yongkun Ding, Dongxian Lai, Tianxuan Huan, Shaoping Zhu, Zhijian Zheng, Guangyu Wang, Yongmin Zheng, Xiantu He, Wenbing Pei, Qingsheng Duan, Weiyan Zhang, Tinggui Feng, Guangnan Chen, and Peijun Gu. Laser hohlraum coupling efficiency on the Shenguang II facility. *Physics of Plasmas*, 9(11):4744, 2002. ISSN 1070664X. doi:[10.1063/1.1516781](https://doi.org/10.1063/1.1516781).
- [117] T. R. Dittrich, O. A. Hurricane, D. A. Callahan, E. L. Dewald, T. Döppner, D. E. Hinkel, L. F. Berzak Hopkins, S. Le Pape, T. Ma, J. L. Milovich, J. C. Moreno, P. K. Patel, H. S. Park, B. A. Remington, J. D. Salmonson, and J. L. Kline. Design of a high-foot high-adiabat ICF capsule for the national ignition facility. *Physical Review Letters*, 112(5):1–5, 2014. ISSN 00319007. doi:[10.1103/PhysRevLett.112.055002](https://doi.org/10.1103/PhysRevLett.112.055002).
- [118] H S Park, O A Hurricane, D A Callahan, D T Casey, E L Dewald, T R Dittrich, T Döppner, D E Hinkel, L F Berzak Hopkins, S Le Pape, T Ma, P K Patel, B A Remington, H F Robey, J D Salmonson, and J L Kline. High-adiabat high-foot inertial confinement fusion implosion experiments on the national ignition facility. *Physical Review Letters*, 112(5):1–5, 2014. ISSN 00319007. doi:[10.1103/PhysRevLett.112.055001](https://doi.org/10.1103/PhysRevLett.112.055001).
- [119] E L Dewald, C Thomas, S Hunter, L Divol, N Meezan, S H Glenzer, L J Suter, E Bond, J L Kline, J Celeste, D Bradley, P Bell, R L Kauffman, J Kilkenny, and O L Landen. Hot electron measurements in ignition relevant Hohlraums on the National Ignition Facility. *Review of Scientific Instruments*, 81(10), 2010. ISSN 00346748. doi:[10.1063/1.3478683](https://doi.org/10.1063/1.3478683).
- [120] C. S. Liu, Marshall N. Rosenbluth, and Roscoe B. White. Raman and Brillouin scattering of electromagnetic waves in inhomogeneous plasmas. *Physics of Fluids*, 17(6):1211–1219, 1974. ISSN 10706631. doi:[10.1063/1.1694867](https://doi.org/10.1063/1.1694867).
- [121] A. Simon, R. W. Short, E. A. Williams, and T. Dewandre. On the inhomogeneous two-plasmon instability. *Physics of Fluids*, 26(10):3107–3118, 1983. ISSN 10706631. doi:[10.1063/1.864037](https://doi.org/10.1063/1.864037).

- [122] D. Batani, L. Antonelli, S. Atzeni, J. Badziak, F. Baffigi, T. Chodukowski, F. Consoli, G. Cristoforetti, R. De Angelis, R. Dudzak, G. Folpini, L. Giuffrida, L. A. Gizzi, Z. Kalinowska, P. Koester, E. Krousky, M. Krus, L. Labate, T. Levato, Y. Maheut, G. Malka, D. Margarone, A. Marocchino, J. Nejd, Ph Nicolai, T. O'Dell, T. Pisarczyk, O. Renner, Y. J. Rhee, X. Ribeyre, M. Richetta, M. Rosinski, M. Sawicka, A. Schiavi, J. Skala, M. Smid, Ch Spindloe, J. Ullschmied, A. Velyhan, and T. Vinci. Generation of high pressure shocks relevant to the shock-ignition intensity regime. *Physics of Plasmas*, 21(3), 2014. ISSN 10897674. doi:[10.1063/1.4869715](https://doi.org/10.1063/1.4869715).
- [123] A. A. Solodov and R. Betti. Stopping power and range of energetic electrons in dense plasmas of fast-ignition fusion targets. *Physics of Plasmas*, 15(4), 2008. ISSN 1070664X. doi:[10.1063/1.2903890](https://doi.org/10.1063/1.2903890).
- [124] T. Döppner, C. A. Thomas, L. Divol, E. L. Dewald, P. M. Celliers, D. K. Bradley, D. A. Callahan, S. N. Dixit, J. A. Harte, S. M. Glenn, S. W. Haan, N. Izumi, G. A. Kyrala, G. Lacaille, J. K. Kline, W. L. Kruer, T. Ma, A. J. MacKinnon, J. M. McNaney, N. B. Meezan, H. F. Robey, J. D. Salmonson, L. J. Suter, G. B. Zimmerman, M. J. Edwards, B. J. MacGowan, J. D. Kilkenny, J. D. Lindl, B. M. Van Wonterghem, L. J. Atherton, E. I. Moses, S. H. Glenzer, and O. L. Landen. Direct measurement of energetic electrons coupling to an imploding low-adiabat inertial confinement fusion capsule. *Physical Review Letters*, 108(13):135006, mar 2012. ISSN 00319007. doi:[10.1103/PhysRevLett.108.135006](https://doi.org/10.1103/PhysRevLett.108.135006). URL <https://link.aps.org/doi/10.1103/PhysRevLett.108.135006>.
- [125] E. L. Dewald, F. Hartemann, P. Michel, J. Milovich, M. Hohenberger, A. Pak, O. L. Landen, L. Divol, H. F. Robey, O. A. Hurricane, T. Döppner, F. Albert, B. Bachmann, N. B. Meezan, A. J. Mackinnon, D. Callahan, and M. J. Edwards. Generation and Beaming of Early Hot Electrons onto the Capsule in Laser-Driven Ignition Hohlräume. *Physical Review Letters*, 116(7):075003, feb 2016. ISSN 10797114. doi:[10.1103/PhysRevLett.116.075003](https://doi.org/10.1103/PhysRevLett.116.075003). URL <https://link.aps.org/doi/10.1103/PhysRevLett.116.075003>.
- [126] J. E. Bailey, G. A. Rochau, R. C. Mancini, C. A. Iglesias, J. J. MacFarlane, I. E. Golovkin, C. Blancard, Ph Cosse, and G. Faussurier. Experimental investigation of opacity models for stellar interior, inertial fusion, and high energy density plasmas. *Physics of Plasmas*, 16(5):058101, may 2009. ISSN 1070664X. doi:[10.1063/1.3089604](https://doi.org/10.1063/1.3089604). URL <http://aip.scitation.org/doi/10.1063/1.3089604>.
- [127] R. Cauble, D. W. Phillion, T. J. Hoover, N. C. Holmes, J. D. Kilkenny, and R. W. Lee. Demonstration of 0.75 Gbar planar shocks in x-ray driven colliding foils. *Physical Review Letters*, 70(14):2102–2105, apr 1993. ISSN 00319007. doi:[10.1103/PhysRevLett.70.2102](https://doi.org/10.1103/PhysRevLett.70.2102). URL <https://link.aps.org/doi/10.1103/PhysRevLett.70.2102>.
- [128] H. S. Park, R. E. Rudd, R. M. Cavallo, N. R. Barton, A. Arsenlis, J. L. Belof, K. J.M. Blobaum, B. S. El-Dasher, J. N. Florando, C. M. Huntington, B. R. Maddox, M. J. May, C. Plechaty, S. T.

- Prisbrey, B. A. Remington, R. J. Wallace, C. E. Wehrenberg, M. J. Wilson, A. J. Comley, E. Giraldez, A. Nikroo, M. Farrell, G. Randall, and G. T. Gray. Grain-size-independent plastic flow at ultrahigh pressures and strain rates. *Physical Review Letters*, 114(6):065502, feb 2015. ISSN 10797114. doi:10.1103/PhysRevLett.114.065502. URL <https://link.aps.org/doi/10.1103/PhysRevLett.114.065502>.
- [129] S. D. Rothman, A. M. Evans, C. J. Horsfield, P. Graham, and B. R. Thomas. Impedance match equation of state experiments using indirectly laser-driven multimegabar shocks. *Physics of Plasmas*, 9(5):1721, may 2002. ISSN 1070664X. doi:10.1063/1.1465419. URL <http://aip.scitation.org/doi/10.1063/1.1465419>.
- [130] R F Smith, J H Eggert, R Jeanloz, T S Duffy, D G Braun, J R Patterson, R E Rudd, J Biener, A E Lazicki, A V Hamza, J Wang, T Braun, L X Benedict, P M Celliers, and G W Collins. Ramp compression of diamond to five terapascals. *Nature*, 511(7509):330–333, 2014. ISSN 1476-4687. doi:10.1038/nature13526. URL <https://doi.org/10.1038/nature13526>.
- [131] Shuai Zhang, Burkhard Militzer, Michelle C. Gregor, Kyle Caspersen, Lin H. Yang, Jim Gaffney, Tadashi Ogitsu, Damian Swift, Amy Lazicki, D. Erskine, Richard A. London, P. M. Celliers, Joseph Nilsen, Philip A. Sterne, and Heather D. Whitley. Theoretical and experimental investigation of the equation of state of boron plasmas. *Physical Review E*, 98(2):023205, aug 2018. ISSN 24700053. doi:10.1103/PhysRevE.98.023205. URL <https://link.aps.org/doi/10.1103/PhysRevE.98.023205>.
- [132] John W. Murdoch, J. D. Kilkenny, D. R. Gray, and W. T. Toner. Time-resolved measurements of the laser burn-through of thin foils. *Physics of Fluids*, 24(11):2107–2114, 1981. ISSN 10706631. doi:10.1063/1.863306. URL <https://aip.scitation.org/doi/10.1063/1.863306>.
- [133] J. Delettrez, D. K. Bradley, P. A. Jaanimagi, and C. P. Verdon. Effect of barrier layers in burnthrough experiments with 351-nm laser illumination. *Physical Review A*, 41(10):5583–5593, may 1990. ISSN 1050-2947. doi:10.1103/PhysRevA.41.5583. URL <https://link.aps.org/doi/10.1103/PhysRevA.41.5583>.
- [134] J. Edwards, M. Dunne, D. Riley, R. Taylor, O. Willi, and S. J. Rose. Time-resolved measurement of x-ray heating in plastic foils irradiated by intense soft-x-ray pulses. *Physical Review Letters*, 67(27):3780–3783, dec 1991. ISSN 00319007. doi:10.1103/PhysRevLett.67.3780. URL <https://link.aps.org/doi/10.1103/PhysRevLett.67.3780>.
- [135] D. R. Kania, H. Kornblum, B. A. Hammel, J. Seely, C. Brown, U. Feldman, G. Glendinning, P. Young, E. Hsieh, M. Hennesian, L. Dasilva, B. J. MacGowan, D. S. Montgomery, C. A. Back, R. Doyas, J. Edwards, and R. W. Lee. Characterization of an x-ray-flux source for the production of high-energy-density plasmas. *Physical Review A*, 46(12):7853–7868, dec 1992. ISSN 10502947. doi:10.1103/PhysRevA.46.7853. URL <https://link.aps.org/doi/10.1103/PhysRevA.46.7853>.

- [136] W. Schwanda and K. Eidmann. Observation of radiative burnthrough in x-ray heated beryllium by time-resolved spectroscopy. *Physical Review Letters*, 69(24):3507–3510, dec 1992. ISSN 00319007. doi:10.1103/PhysRevLett.69.3507. URL <https://link.aps.org/doi/10.1103/PhysRevLett.69.3507>.
- [137] C. A. Back, L. Da Silva, H. Kornblum, D. Montgomery, B. MacGowan, G. Glendinning, J. Fenske, E. Hsieh, and R. W. Lee. X-ray flux from a burnthrough Au foil. *Journal of Quantitative Spectroscopy and Radiative Transfer*, 51(1-2):19–25, jan 1994. ISSN 00224073. doi:10.1016/0022-4073(94)90061-2. URL <https://www.sciencedirect.com/science/article/abs/pii/0022407394900612>.
- [138] R E Olson, R J Leeper, A Nobile, J A Oertel, G A Chandler, K Cochrane, S C Dropinski, S Evans, S W Haan, J L Kaae, J P Knauer, K Lash, L P Mix, A Nikroo, G A Rochau, G Rivera, C Russell, D Schroen, R J Sebring, D L Tanner, R E Turner, and R J Wallace. Shock propagation, preheat, and x-ray burnthrough in indirect-drive inertial confinement fusion ablator materials. *Physics of Plasmas*, 11(5 PART 2):2778–2789, 2004. ISSN 1070664X. doi:10.1063/1.1691032.
- [139] R. E. Olson, R. J. Leeper, S. C. Dropinski, L. P. Mix, G. A. Rochau, S. H. Glenzer, O. S. Jones, L. J. Suter, J. L. Kaae, C. H. Shearer, and J. N. Smith. Time and spatially resolved measurements of x-ray burnthrough and re-emission in Au and Au:Dy:Nd foils. *Review of Scientific Instruments*, 74(3 II): 2186–2190, mar 2003. ISSN 00346748. doi:10.1063/1.1537866. URL <http://aip.scitation.org/doi/10.1063/1.1537866>.
- [140] James H. Hammer, Max Tabak, Scott C. Wilks, John D. Lindl, David S. Bailey, Peter W. Rambo, Arthur Toor, George B. Zimmerman, and John L. Porter. High yield inertial confinement fusion target design for a z-pinch-driven hohlraum. *Physics of Plasmas*, 6(5 I):2129–2136, may 1999. ISSN 1070664X. doi:10.1063/1.873464. URL <http://aip.scitation.org/doi/10.1063/1.873464>.
- [141] M. E. Cuneo, R. A. Vesey, J. L. Porter, G. R. Bennett, D. L. Hanson, L. E. Ruggles, W. W. Simpson, G. C. Idzorek, W. A. Stygar, J. H. Hammer, J. J. Seamen, J. A. Torres, J. S. McGurn, and R. M. Green. Double [Formula presented]-Pinch Hohlraum Drive with Excellent Temperature Balance for Symmetric Inertial Confinement Fusion Capsule Implosions. *Physical Review Letters*, 88(21):4, may 2002. ISSN 10797114. doi:10.1103/PhysRevLett.88.215004. URL <https://link.aps.org/doi/10.1103/PhysRevLett.88.215004>.
- [142] M E Cuneo, R A Vesey, G R Bennett, D B Sinars, W A Stygar, E M Waisman, J L Porter, P K Rambo, I C Smith, S V Lebedev, J P Chittenden, D E Bliss, T J Nash, G A Chandler, B B Afeyan, E P Yu, R B Campbell, R G Adams, D L Hanson, T A Mehlhorn, and M K Matzen. Progress in symmetric ICF capsule implosions and wire-array z-pinch source physics for double-pinch-driven hohlraums. *Plasma Physics and Controlled Fusion*, 48(2):R1–R35, feb 2006. ISSN 07413335. doi:10.1088/0741-3335/48/2/R01. URL <http://stacks.iop.org/0741-3335/48/i=2/a=R01?key=crossref.7aa5258fef08de090d86118dbb831830>.

- [143] T. W.L. Sanford, R. E. Olson, R. L. Bowers, G. A. Chandler, M. S. Derzon, D. E. Hebron, R. J. Leeper, R. C. Mock, T. J. Nash, D. L. Peterson, L. E. Ruggles, W. W. Simpson, K. W. Struve, and R. A. Vesey. Z-pinch-generated x rays demonstrate potential for indirect-drive icf experiments. *Physical Review Letters*, 83(26):5511–5514, dec 1999. ISSN 10797114. doi:[10.1103/PhysRevLett.83.5511](https://doi.org/10.1103/PhysRevLett.83.5511). URL <https://link.aps.org/doi/10.1103/PhysRevLett.83.5511>.
- [144] A. Pak, L. Divol, A. L. Kritcher, T. Ma, J. E. Ralph, B. Bachmann, L. R. Benedetti, D. T. Casey, P. M. Celliers, E. L. Dewald, T. Döppner, J. E. Field, D. E. Fratanduono, L. F. Berzak Hopkins, N. Izumi, S. F. Khan, O. L. Landen, G. A. Kyrala, S. LePape, M. Millot, J. L. Milovich, A. S. Moore, S. R. Nagel, H. S. Park, J. R. Rygg, D. K. Bradley, D. A. Callahan, D. E. Hinkel, W. W. Hsing, O. A. Hurricane, N. B. Meezan, J. D. Moody, P. Patel, H. F. Robey, M. B. Schneider, R. P.J. Town, and M. J. Edwards. Examining the radiation drive asymmetries present in the high foot series of implosion experiments at the National Ignition Facility. *Physics of Plasmas*, 24(5):056306, may 2017. ISSN 10897674. doi:[10.1063/1.4979192](https://doi.org/10.1063/1.4979192). URL <http://aip.scitation.org/doi/10.1063/1.4979192>.
- [145] L. Masse, D. Clark, S. Maclaren, L. Berzak Hopkins, S. Haan, S. Khan, A. Kritcher, G. Kyrala, O. Landen, J. Lindl, T. Ma, P. Patel, J. Ralph, J. Salmonson, R. Tipton, and C. Weber. A simulation-based model for understanding the time dependent x-ray drive asymmetries and error bars in indirectly driven implosions on the National Ignition Facility. *Physics of Plasmas*, 26(6):062703, jun 2019. ISSN 10897674. doi:[10.1063/1.5092827](https://doi.org/10.1063/1.5092827). URL <http://aip.scitation.org/doi/10.1063/1.5092827>.
- [146] Hans G. Rinderknecht, D. T. Casey, R. Hatarik, R. M. Bionta, B. J. Macgowan, P. Patel, O. L. Landen, E. P. Hartouni, and O. A. Hurricane. Azimuthal Drive Asymmetry in Inertial Confinement Fusion Implosions on the National Ignition Facility. *Physical Review Letters*, 124(14):145002, apr 2020. ISSN 10797114. doi:[10.1103/PhysRevLett.124.145002](https://doi.org/10.1103/PhysRevLett.124.145002). URL <https://link.aps.org/doi/10.1103/PhysRevLett.124.145002>.
- [147] OL Landen, PA Amendt, LJ Suter, RE Turner, SG Glendinning, SW Haan, SM Pollaine, BA Hammel, M Tabak, MD Rosen, et al. A simple time-dependent analytic model of the p 2 asymmetry in cylindrical hohlraums. *Physics of Plasmas*, 6(5):2137–2143, 1999.
- [148] E. L. Dewald, R. Tommasini, N. B. Meezan, O. L. Landen, S. Khan, R. Rygg, J. Field, A. S. Moore, D. Sayre, A. J. MacKinnon, L. F. Berzak Hopkins, L. Divol, S. Le Pape, A. Pak, C. A. Thomas, M. Farrell, A. Nikroo, and O. Hurricane. First demonstration of improved capsule implosions by reducing radiation preheat in uranium vs gold hohlraums. *Physics of Plasmas*, 25(9):092702, sep 2018. ISSN 10897674. doi:[10.1063/1.5039385](https://doi.org/10.1063/1.5039385). URL <http://aip.scitation.org/doi/10.1063/1.5039385>.
- [149] Mordecai D. Rosen. The science applications of the high-energy density plasmas created on the Nova laser. *Physics of Plasmas*, 3(5):1803–1812, may 1996. ISSN 1070-664X. doi:[10.1063/1.871683](https://doi.org/10.1063/1.871683). URL <http://aip.scitation.org/doi/10.1063/1.871683>.

- [150] EE Meshkov. Instability in shock-accelerated boundary separating two gasses. *Izv. Akad. Nauk SSSR, Mekh. Zhidk. Gasa*, 5:151–158, 1969.
- [151] David H Sharp. Overview of rayleigh-taylor instability. Technical report, Los Alamos National Lab., NM (USA), 1983.
- [152] J. Delettrez, D. K. Bradley, and C. P. Verdon. The role of the Rayleigh-Taylor instability in laser-driven burnthrough experiments. *Physics of Plasmas*, 1(7):2342–2349, jul 1994. ISSN 1070664X. doi:[10.1063/1.870631](https://doi.org/10.1063/1.870631). URL <http://aip.scitation.org/doi/10.1063/1.870631>.
- [153] L. J. Suter, R. L. Kauffman, C. B. Darrow, A. A. Hauer, H. Kornblum, O. L. Landen, T. J. Orzechowski, D. W. Phillion, J. L. Porter, L. V. Powers, A. Richard, M. D. Rosen, A. R. Thiessen, and R. Wallace. Radiation drive in laser-heated hohlraums. *Physics of Plasmas*, 3(5):2057–2062, 1996. ISSN 10897674. doi:[10.1063/1.872002](https://doi.org/10.1063/1.872002).
- [154] P. W. Hatfield, S. J. Rose, and R. H.H. Scott. The blind implosion-maker: Automated inertial confinement fusion experiment design. *Physics of Plasmas*, 26(6), 2019. ISSN 10897674. doi:[10.1063/1.5091985](https://doi.org/10.1063/1.5091985).
- [155] Peter Hatfield, Steven Rose, Robbie Scott, Ibrahim Almosallam, Stephen Roberts, and Matt Jarvis. Using sparse gaussian processes for predicting robust inertial confinement fusion implosion yields. *IEEE Transactions on Plasma Science*, 48(1):14–21, 2019.
- [156] V. Gopalaswamy, R. Betti, J. P. Knauer, N. Luciani, D. Patel, K. M. Woo, A. Bose, I. V. Igumenshchev, E. M. Campbell, K. S. Anderson, K. A. Bauer, M. J. Bonino, D. Cao, A. R. Christopherson, G. W. Collins, T. J.B. Collins, J. R. Davies, J. A. Delettrez, D. H. Edgell, R. Epstein, C. J. Forrest, D. H. Froula, V. Y. Glebov, V. N. Goncharov, D. R. Harding, S. X. Hu, D. W. Jacobs-Perkins, R. T. Janezic, J. H. Kelly, O. M. Mannion, A. Maximov, F. J. Marshall, D. T. Michel, S. Miller, S. F.B. Morse, J. Palastro, J. Peebles, P. B. Radha, S. P. Regan, S. Sampat, T. C. Sangster, A. B. Sefkow, W. Seka, R. C. Shah, W. T. Shmyada, A. Shvydky, C. Stoeckl, A. A. Solodov, W. Theobald, J. D. Zuegel, M. Gatu Johnson, R. D. Petrasso, C. K. Li, and J. A. Frenje. Tripled yield in direct-drive laser fusion through statistical modelling. *Nature*, 565(7741):581–586, 2019. ISSN 14764687. doi:[10.1038/s41586-019-0877-0](https://doi.org/10.1038/s41586-019-0877-0).